
GRL-SNAM: GEOMETRIC REINFORCEMENT LEARNING WITH PATH DIFFERENTIAL HAMILTONIANS FOR SIMULTANEOUS NAVIGATION AND MAPPING IN UNKNOWN ENVIRONMENTS

Aditya Sai Ellendula¹, Yi Wang², Minh Nguyen³, Chandrajit Bajaj^{1,2}

¹ Department of Computer Science, University of Texas at Austin, Austin, TX 78712, USA

² Oden Institute, University of Texas at Austin, Austin, TX 78712, USA

³ Department of Mathematics, University of Texas at Austin, Austin, TX 78712, USA

{adityase, panzer.wy, minhpnguyen, bajaj}@utexas.edu

ABSTRACT

We present GRL-SNAM, a geometric reinforcement learning framework for Simultaneous Navigation and Mapping (SNAM) in unknown environments. A SNAM problem is challenging as it needs to design hierarchical or joint policies of multiple agents that control the movement of a real-life robot towards the goal in mapless environment, i.e. an environment where the map of the environment is not available *a priori*, and needs to be acquired through sensors. The sensors are invoked from the path learner, i.e. navigator, through active query responses to sensory agents, and along the motion path. GRL-SNAM differs from preemptive navigation algorithms and other reinforcement learning methods by relying exclusively on local sensory observations without constructing a global map. Our approach formulates path navigation and mapping as a dynamic shortest path search and discovery process using controlled Hamiltonian optimization: sensory inputs are translated into local energy landscapes that encode reachability, obstacle barriers, and deformation constraints, while policies for sensing, planning, and reconfiguration evolve stagewise via updating Hamiltonians. A reduced Hamiltonian serves as an adaptive score function, updating kinetic/potential terms, embedding barrier constraints, and continuously refining trajectories as new local information arrives. We evaluate GRL-SNAM on two different 2D navigation tasks. To show our geometric RL policies naturally decomposes and bring hierarchy, we build a hyperelastic robot that learns to squeeze through narrow gaps, detour around obstacles, and generalize to unseen environments; To show GRL-SNAM is generalizable to indoor scene layout, we build a point-nav system in an unseen indoor maze layouts. Comparing against *local reactive* baselines (PF, CBF, staged DWA, staged PPO) and *global* policy learning references (A*, PPO, SAC) under identical stagewise sensing constraints, GRL-SNAM maintains path quality while using the minimal map coverage. It preserves clearance, generalizes to unseen layouts, and demonstrates that Geometric RL learning via updating Hamiltonians enables high-quality navigation through *minimal exploration* via local energy refinement rather than extensive global mapping. The code is publicly available on Github.

1 INTRODUCTION

Reinforcement learning (RL) has achieved impressive results in high-dimensional control, yet its application to real-world continuous navigation remains fundamentally limited. Modern deep RL methods such as SAC (Haarnoja et al., 2018) and PPO (Schulman et al., 2017) typically require millions of interactions to learn a single robust policy, and their performance degrades sharply under even mild distribution shift. These challenges are amplified in simultaneous navigation and mapping (SNAM), where the agent must traverse unknown environments while building and updating spatial representations online. In this setting, long-horizon reasoning, multi-scale decision making, and the need for safe, sample-efficient adaptation often overwhelm existing methods.

Why many RL fails at SNAM. Three structural limitations are particularly acute in navigation: (i) *Sample efficiency*: continuous control demands rich exploration and fine-grained motor control; model-free RL compensates with massive data collection and unstable credit assignment. (ii) *Generalization*: black-box policies memorize training environments instead of discovering transferable navigation principles, leading to brittle behavior under new obstacle layouts or sensing conditions. (iii) *Temporal scale separation*: navigation couples fast obstacle avoidance, mid-range local planning, and slow global goal pursuit. Hierarchical RL (Sutton et al., 1998; Vezhnevets et al., 2017) introduces additional levels but still relies on monolithic value-based objectives and carefully engineered reward decompositions.

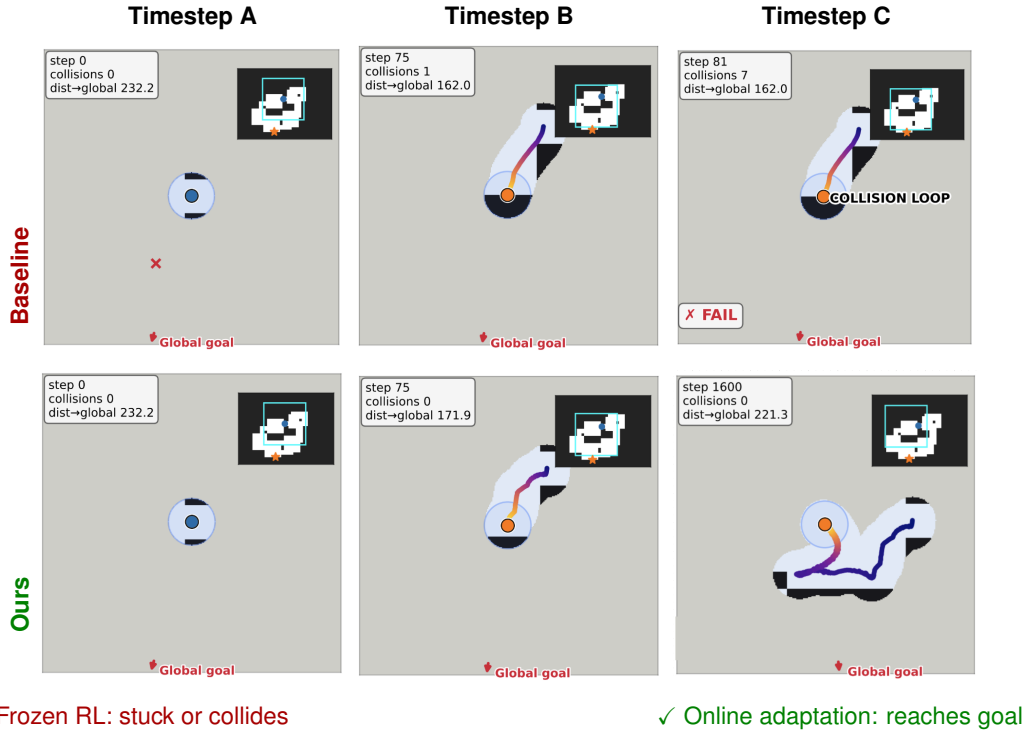


Figure 1: **Fixed policy vs. online adaptation in dungeon navigation.** We display global time step, collision count, and remaining goal distance on top-left of a navigation process under a mapless environment; the inset shows the local sensed view used for decision-making. Top: a fixed RL controller executes a fixed behavior and fails by colliding / entering a collision loop as the local obstacle geometry changes. Bottom: our method performs *online correction* by adjusting its motion field using only short-horizon feedback (clearance, distance-to-goal, and speed) to avoid obstacles and keep making progress, ultimately reaching the global goal.

These issues are magnified in SNAM. Recent systems such as Simultaneous Goal Localization and Mapping (SGoLAM) (Kim et al., 2021), Cognitive Mapping and Planning (CMP) (Gupta et al., 2019), and Continual Learning of Simultaneous Localization and Mapping (CL-SLAM) (Vödisch et al., 2023) tightly couple mapping and policy learning, often by constructing increasingly detailed metric maps that are then consumed by learned or differentiable planners. While effective, they implicitly optimize for *better maps*, not necessarily *minimal, task-focused exploration*. In contrast, our objective is to *reach the goal along high-quality, well-weighted paths while mapping as little of the unknown environment as possible*: as new local information is revealed, the navigator should differentially refine the path and its safety margins, rather than rebuilding global plans from scratch.

From unstructured policies to geometric structure. We view these limitations as symptoms of treating navigation as structureless optimization. Real robots are constrained by physics: conservation laws, kinematics, actuator limits, and contact constraints. Policies that ignore this structure are difficult to train, hard to interpret, and unstable over long rollouts. A geometric, physics-grounded formulation offers three advantages: (i) *Physical realizability*: dynamics remain compatible with

real actuators and constraints; (ii) *Stability*: symplectic structure preserves invariants (e.g., energy, momentum) and mitigates long-horizon drift; (iii) *Compositionality*: complex behavior emerges from composing interpretable energy terms (goal attraction, collision barriers, deformation costs) that can be reweighted and adapted without relearning from scratch.

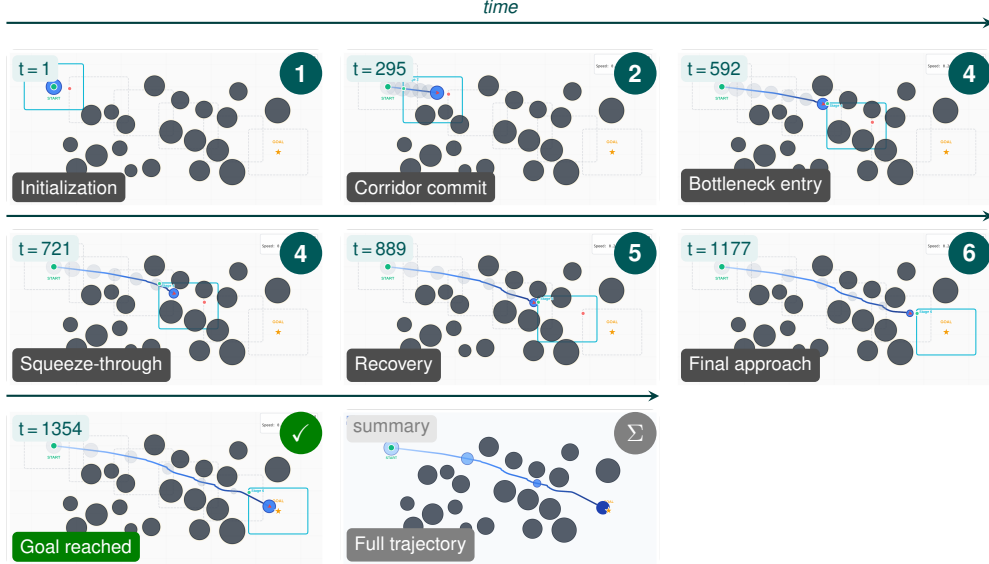


Figure 2: **GRL-SNAM rollout on a cluttered layout (representative episode).** Snapshots are ordered left-to-right within each row, with time increasing across rows. *Row 1*: initialization ($t=1$) and early *corridor commitment* ($t=295$), followed by *bottleneck entry* ($t=592$). *Row 2*: *squeeze-through* of the narrow passage ($t=721$), *recovery/re-centering* ($t=889$), and *final approach* to the goal ($t=1177$). *Row 3*: successful arrival ($t=1354$) and the full-trajectory overlay. Circular stage markers (1-6) denote the active hierarchical planning stage selected by the navigator at that snapshot.

GRL-SNAM: a geometric multi-policy, path-learner navigator process. We introduce **GRL-SNAM**, a *Geometric RL framework for Simultaneous Path Navigation and Mapping*, that realize SNAM policy learning via learning to formulate Hamiltonian dynamics. Our main contributions are:

1. **Geometric RL framework for SNAM via Hamiltonians (Section 3.1).** We cast navigation and mapping as formulating control optimization problem sequentially. The optimal control problems(OCPs) are mapped to the problem of learning the blue geometry and topology of Hamiltonian landscape through Hamiltonian dynamics. This yields our geometric RL model: it produces differentiable updates of the Hamiltonian. Differentiation in phase space corresponds to a policy update, while variation across environments induces a meta-level adaptation rule for the lowest amortized cost to move.
2. **Multi-scale geometric coordination via multi-policy energies (Section 3.2).** We introduce a three-submodular-policy architecture whose local policy govern sensing, frame-level motion, and shape control. GRL-SNAM composes each policy via constructing induced Hamiltonian flow maps and realize a discrete, feedforward Hamiltonian dynamics rather than a backward-forward Hamiltonian-Jacobi-Bellman optimization. This achieves temporal scale separation without hand-designed hierarchies as well.
3. **Physics-grounded offline-online adaptation (Section 3.3).** Building on our Geometric RL framework, we learn Hamiltonians via a hybrid offline-online learning scheme. During offline training, from trajectory and velocity observations, we identify the family of admissible control objectives consistent with each context and learn an embedding of the resulting landscape of local OCPs. While generalizing to unseen, online environments, our method performs online geometric alignment by adapting input-source terms naturally in Hamiltonian dynamics. This repeated-online adaptation strategy yields stable,

low-variance adaptation that preserves geometric, topological and functional (i.e. motion physics) structure.

4. **Empirical validation on deformable navigation (Section 5).** On a challenging hyperelastic ring robot that must squeeze through cluttered, narrow passages, GRL-SNAM achieves higher success rates, better safety margins, and superior sample efficiency compared to many standard deep RL baselines (SAC, TRPO, PPO), as well as task-specific navigation and mapping baselines such as potential-field (PF) planners, control barrier functions (CBF), and A^* -based methods.

Together, these claims support our rudiments: **when policy update respects geometric and Hamiltonian structure, complex navigation and mapping behaviors emerge naturally from energy reshaping rather than from brittle reward engineering or value iteration.** We demonstrate this principle on deformable robot navigation in unknown environments, a testbed that captures the core difficulties of real-world SNAM while showcasing the benefits of physics-informed policy design.

2 RELATED WORKS

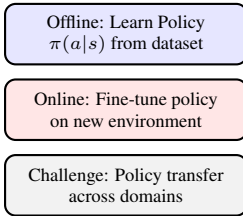
We focus on structure-preserving, deployable navigation with deformable bodies under strict local sensing. Our work intersects geometric and Hamiltonian learning, safety-critical control, deformable robot navigation, neural scene representations, and simultaneous navigation and mapping.

Geometric Reinforcement Learning in navigation. Most navigation RL methods treat the problem as control in flat Euclidean spaces using standard algorithms such as PPO and TD3 (Schulman et al., 2017; Fujimoto et al., 2018). Variants with richer reward shaping or auxiliary losses improve collision avoidance (Taheri et al., 2024), but still ignore the underlying geometric structure and typically require millions of interactions for robust performance (Dehghani Tezerjani et al., 2024). Geometric approaches explicitly exploit configuration-space structure: SE(2)/SE(3)-equivariant policies for manipulation (Hoang et al., 2025), Riemannian formulations that enforce constraints via tangent-space projections (Martínez-Rubio & Pokutta, 2023; Klein et al., 2023), and Hamiltonian / port-Hamiltonian neural networks that preserve symplectic structure and energy (Desai et al., 2021). However, these works are largely restricted to simple control or manipulation tasks, do not address deformable-body navigation, and are not designed for SNAM. In contrast, GRL-SNAM uses a Hamiltonian formulation for *navigation itself*: sensing, path planning, and deformation all evolve on a shared energy manifold with differential policy optimization rather than ad-hoc Euclidean policy updates.

We consider the geometric property in the RL policy iteration itself as well. Most mainstream deep RL algorithms are developed within the dynamic programming principle (DPP): they optimize either value functions or policy surrogates whose correctness is ultimately justified by Bellman consistency. This includes value-based and actor–critic families, even when the update is implemented via policy gradients (e.g., PPO, SAC, TRPO), because the critic and advantage estimates are derived from Bellman-style recursions rather than from Hamilton–Jacobi–Bellman (HJB) analysis or dual optimal control constructions. In contrast, our approach follows a growing line of work that explicitly departs from DPP and instead leverages continuous-time optimal control structure—HJB and/or duality-based Hamiltonian formulations—to define learning objectives and updates without relying on Bellman backups. Representative examples include model-free HJB-based learning (Settai et al., 2025), martingale formulations that reinterpret or relax DPP conditions (Jia & Zhou, 2023), and duality-driven Hamiltonian RL (Nguyen & Bajaj, 2025a), which we build upon and extend. The key distinction between GRL-SNAM and other RL navigation methods is two-folded: we do not reparameterize value-function gradients; we learn and adapt a reduced Hamiltonian whose energy decomposition directly induces the closed-loop dynamics. We refer readers Figure 3 for a comparison statement.

Safety-critical and reward-exploring navigation. When training to plan obstacle-avoidance paths, the design of reward affects the quality of output trajectories via policy learning. Earlier work focuses on handcrafted or intrinsic curiosity reward (Tai et al., 2017; 2018a). Control Barrier Functions (CBFs) have emerged as a principled way to enforce safety by projecting candidate actions into a safe set, including model-based CBF-RL combinations (Li et al., 2023), neural zeroing barrier

Standard RL



Our GRL-SNAM

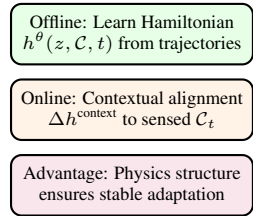


Figure 3: Comparison between standard RL offline/online adaptation and our physics-grounded approach. Standard methods learn arbitrary policies and struggle with transfer, while our approach learns physically meaningful Hamiltonians that naturally adapt to environmental variations.

functions (Feng et al., 2023), adaptive barrier mechanisms for dynamic environments (Mohammad & Bezzo, 2025), and social-navigation CBFs for human–robot interaction (Jang & Ghaffari, 2024). While these methods provide formal safety guarantees, safety is typically treated as an *external projection layer* on top of an otherwise standard controller, which often leads to conservative, sometimes myopic behavior and weak coupling between task optimality and safety. GRL-SNAM instead integrates safety *within* the Hamiltonian energy via barrier potentials: obstacles, free-space preferences, and goal attraction jointly shape the local energy landscape, so that safety and optimality are co-optimized under a symplectic, structure-preserving flow.

Deformable and soft robot navigation. Soft and deformable robots have motivated sophisticated modeling and control techniques, including hyperelastic material models with pressure-stiffening control (Roshanfar et al., 2023), passivity-based control via differential geometry of curves (Caesbrood et al., 2022), and spectral submanifold reduction for real-time hyperelastic control (Alora et al., 2025). Physics-informed learning further improves fidelity: PINN-Ray (Wang et al., 2024) and related models for non-conservative effects (Liu & Della Santina, 2024) achieve accurate displacement prediction but primarily target offline modeling rather than adaptive navigation. For navigation specifically, ring-like or morphable bodies such as aerial LCE-based gap navigators (Qi et al., 2024) and HAVEN (Mulvey & Nanayakkara, 2024) use pre-programmed deformation sequences or offline-optimized actuation patterns with deterministic execution. These systems cannot adapt deformation strategies online when geometry of environment changes, and they lack a unifying energy-based view that couples shape, motion, and sensing. GRL-SNAM fills this gap by treating the deformable robot as an energy-carrying body: deformation penalties, contact forces, and path costs are encoded in a Hamiltonian whose gradients drive both motion and shape control under changing local observations.

Neural scene representations for navigation. Neural implicit maps provide dense geometric information for navigation. NeRF-based SLAM methods such as NICE-SLAM (Zhu et al., 2022) and iMAP (Sucar et al., 2021) reconstruct detailed 3D scenes, while Neural Topological SLAM (Chaplot et al., 2020) and semantic extensions with large vision models (Zheng et al., 2025) combine learned mapping with classical planning. 3D Gaussian splatting approaches like GS-SLAM (Yan et al., 2024) and SplaTAM (Keetha et al., 2024) offer real-time, high-fidelity reconstruction suitable for robot navigation. These methods aim to build accurate maps; the control policy is typically a separate planning layer, and the system often assumes the luxury of extensive mapping before or during navigation. GRL-SNAM is complementary: any of these scene representations can be converted into signed-distance and occupancy-derived potentials for our barrier and goal terms, but our objective is to *minimize mapping effort*, using only local observations to progressively refine a Hamiltonian that encodes the task.

Simultaneous navigation and mapping (SNAM). Most SNAM methods prioritize constructing rich global maps and then planning on them. SGoLAM (Kim et al., 2021) couples goal localization with occupancy mapping, CMP (Gupta et al., 2019) integrates a differentiable planner into a learned map, and CL-SLAM (Vödisch et al., 2023) focuses on maintaining maps for long-term operation. These approaches do not explicitly reason about the cost of mapping itself and are not designed

for deformable bodies or binded with optimal control problems. Some works encourage to learn a context-aware reward (Liang et al., 2023) or an explicit terrain cost map (Sathyamoorthy et al., 2022) that can be used to compute dynamically feasible trajectories while simultaneously reading the partial map, yet they still rely on RL-driven policy network or model-based fixed rule (i.e. DWA, Fox et al. (2002)) to apply the learned reward/cost. GRL-SNAM instead targets *joint exploration*: the robot maintains only the local information needed to define a good energy landscape around its current belief, continually refining least-cost trajectories as new observations arrive rather than insisting on globally complete maps.

Hierarchical, multi-agent, and imitation-based navigation. Hierarchical RL decomposes complex navigation into sub-tasks with high-level coordinators, as in HRL4IN (Li et al., 2020a) and adaptive policy-family methods (Lee et al., 2023). Multi-agent frameworks such as RoboBallet (Lai et al., 2025) and MACRPO (Kargar & Kyrki, 2021) achieve impressive coordinated behavior using graph-based policies and improved information sharing. However, these methods typically rely on manually specified hierarchies or reward structures and seldom preserve underlying geometric or energy structure, making it difficult to guarantee stable coordination across time scales. Imitation learning and inverse RL further improve sample efficiency using expert trajectories: large-scale behavioral cloning (RT-1) (Brohan et al., 2023), safe imitation via GAIL-style methods (Tai et al., 2018b), DAgger-based continuous navigation (Shi et al., 2025), and confidence-aware imitation for sub-optimal demonstrations (Zhang et al., 2022). These approaches are powerful when high-quality demonstrations exist but struggle when expert coverage of the full deformation and contact behavior space is limited. GRL-SNAM shares with hierarchical and imitation methods the aim of efficient learning but differs in *how* structure is encoded: we do not hand-design a task graph; instead, sensing, path, and deformation policies are coupled through a shared Hamiltonian with differential updates, yielding principled multi-scale coordination and stability guarantees.

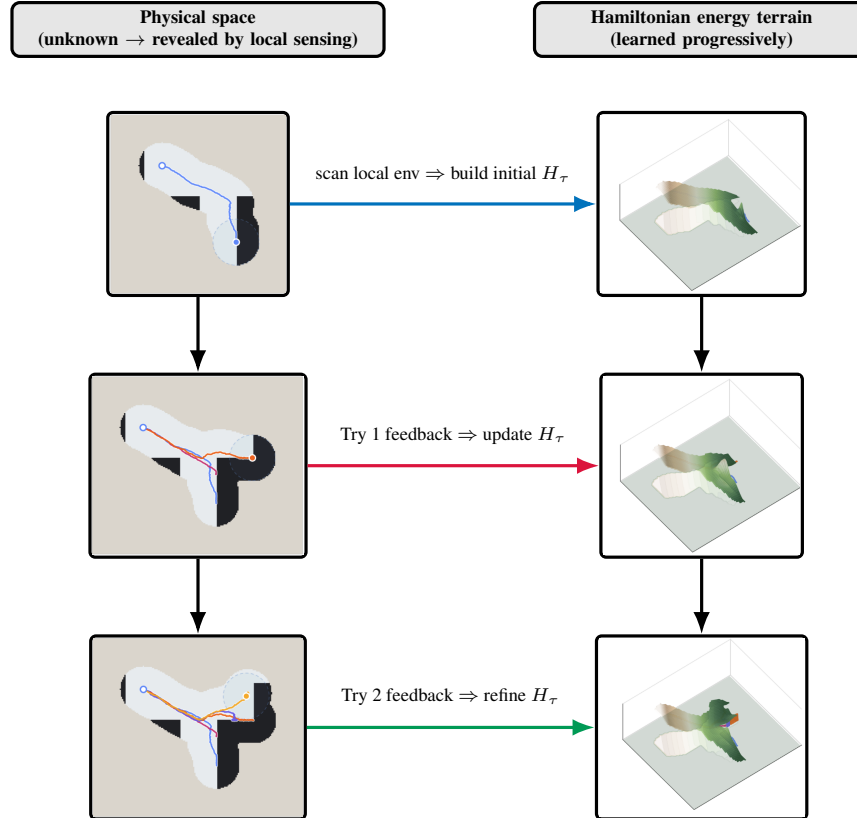
Foundation models for navigation reasoning. Recent work leverages large foundation models for high-level navigation reasoning, goal inference, and multi-agent coordination (Zhu et al., 2024; Wang et al., 2025). These systems excel at semantic understanding, language-grounded objectives, and flexible decision-making but generally outsource low-level control to conventional planners or RL policies, creating a gap between symbolic reasoning and physically consistent motion. GRL-SNAM is complementary: foundation models can supply high-level instructions or semantic goals that we encode as potential energy terms in our Hamiltonian, while our structure-preserving dynamics ensure that these goals translate into safe, physically plausible trajectories for a deformable body under local sensing.

Positioning of GRL-SNAM. Across these paradigms, existing methods typically provide *some* of: geometric structure, safety, sample efficiency, deformable-body support, or SNAM capabilities, but not all simultaneously. Our GRL-SNAM framework is, to our knowledge, the first to (i) formulate deformable-body SNAM as coupled Hamiltonian dynamics on a shared energy manifold under strict local sensing, (ii) integrate safety, deformation costs, and navigation objectives directly into the energy rather than in external projection layers, and (iii) coordinate sensing, planning, and deformation via a differential multi-policy architecture with symplectic updates. This combination yields high-quality, well-weighted paths with minimal mapping effort, while preserving geometric structure and enabling principled analysis of stability and convergence.

3 METHODOLOGY

Overview. We address how GRL-SNAM converts an online mapless navigation task into a stage-wise *energy landscape exploration and mapping* process under dynamical and geometric constraints. The SNAM task is to move a (deformable) robot in 2d space from $\mathbf{x}_0 \in \mathbb{R}^2$ to a goal $\mathbf{x}_g \in \mathbb{R}^2$ in an unknown workspace whose obstacles are encoded by an (unknown) occupancy field $I : \mathbb{R}^2 \rightarrow \{0, 1\}$. The robot is bound with state $\mathbf{q} = (\mathbf{y}, \mathbf{c}, \psi) \in \mathcal{Q}$ where $\mathbf{c} \in \mathbb{R}^2$ parameterize the robot pose in world coordinate, and $\mathbf{y} \in \mathbb{R}^{\text{sensor}}$, $\psi \in \mathbb{R}^{\text{robot}}$ collect sensory and deformation/object configuration variables. The configuration space \mathcal{Q} is assumed to be decomposable into three individual configuration space $\mathcal{Q} = \mathcal{Q}_y \times \mathcal{Q}_f \times \mathcal{Q}_o$, with $\mathbf{y} \in \mathcal{Q}_y$, $\mathbf{c} \in \mathcal{Q}_f$ and $\psi \in \mathcal{Q}_o$.

Progressive Hamiltonian Landscape Learning from Local Sensing along Hamiltonian geodesic pathways



Idea: In an unknown environment, the agent repeatedly senses a *local* neighborhood, attempts to reach the stage goal, and incrementally learns a Hamiltonian energy landscape whose valleys guide future attempts under partial observability.

Figure 4: **Conceptual overview: progressive energy-landscape shaping from local sensing.** *Left:* the physical workspace is initially unknown and is revealed only through local sensing around the agent, producing a partial view of nearby obstacles and a stage goal. *Right:* from this partial context, the agent builds an initial internal “energy terrain” and then repeatedly attempts a short plan toward the stage goal; each attempt produces simple feedback (e.g., collisions/clearance and progress), which is used to refine the terrain. Over successive refinements, the terrain becomes smoother and its low-energy valleys align with traversable corridors, guiding future attempts even under partial observability.

We assume the navigation system can query an independent sensor and the sensor would return an environment context \mathcal{E} sensed via current configuration \mathbf{q} ¹. The context \mathcal{E} at least include a local target goal $\mathbf{c}_{target}(\mathcal{E}) \in \mathbb{R}^2$, an obstacle cardinality $C(\mathcal{E}) \in \mathbb{N}$ and $C(\mathcal{E})$ non-collided constraints $\{d_i(\mathbf{q}; \mathcal{E}) \geq 0\}_{i=1}^{C(\mathcal{E})}$. Given current stage's context \mathcal{E} , GRL-SNAM learns to “construct” optimal control problems, whose solution offers an optimally controlled path, by learning to map each environment context \mathcal{E}_τ at stage $\tau = 0, 1, 2, \dots$, into a *reduced Hamiltonian* via a parametrized network η_ξ :

$$\eta_\xi : \mathcal{E}_\tau \longmapsto H(\cdot; \mathcal{E}_\tau) \in \mathcal{H}, \quad \mathcal{H} \cong C^\infty(T^* \mathcal{Q}, \mathbb{R}),$$

where $T^* \mathcal{Q}$ refers cotangent bundle of \mathcal{Q} . An element of $T^* \mathcal{Q}$ is a pair (\mathbf{q}, p) with $\mathbf{q} \in \mathcal{Q}$ and $p \in T_q^* \mathcal{Q}$, where p is a covector (a linear functional) acting on tangent vectors $\mathbf{v} \in T_q \mathcal{Q}$. The *policy* π , different from conventional RL definition, is denoted as the time- Δt flow map induced by Hamiltonian vector field:

$$\pi(\mathbf{q}|p) := \Phi_H^{\Delta t}(\mathbf{q}, p), \quad \text{where } \Phi_H^{\Delta t}(\cdot) : T^* \mathcal{Q} \rightarrow T^* \mathcal{Q}, \quad (\mathbf{q}_{t+\Delta t}, p_{t+\Delta t}) = \Phi_H^{\Delta t}(\mathbf{q}_t, p_t). \quad (1)$$

It then treats a SNAM problem as finding three policies operating at different effective timescales of each subsystem by decomposing H into three Hamiltonians $H_y : T^* \mathcal{Q}_y \rightarrow \mathbb{R}$, $H_f : T^* \mathcal{Q}_f \rightarrow \mathbb{R}$ and $H_o : T^* \mathcal{Q}_o \rightarrow \mathbb{R}$.

- i.) a *sensing policy* $\pi_y : T^* \mathcal{Q}_y \rightarrow T^* \mathcal{Q}_y$ that maintains how to update sensor configuration to acquire environment representation and active collision constraints from partial observations;
- ii.) a *frame policy* $\pi_f : T^* \mathcal{Q}_f \rightarrow T^* \mathcal{Q}_f$ that plans short-horizon motion in local frames toward intermediate “stage” goal \mathbf{c}_{target} ;
- iii.) a *shape policy* $\pi_o : T^* \mathcal{Q}_o \rightarrow T^* \mathcal{Q}_o$ that modulates the robot’s morphology (e.g., deformation or scale) to exploit narrow passages.

Rather than stacking these as a manually tuned hierarchy, we treat each policy as a flow map with its own energy terms under a shared latent codex of sensed environments. We denote g_ξ , which contains both η_ξ and policy specific parameter (discussed in Section 3.2), as the overall navigator function of GRL-SNAM. GRL-SNAM further separates learning g_ξ into complementary regimes: *offline*, we train reference Hamiltonians on trajectory data to capture fundamental couplings between sensing, planning, and deformation in local frames; *online*, we adapt open-loop control terms that reweight fixed energy components and add minimal non-conservative corrections injected into policies. Formally, offline learning yields a initial reference reduced Hamiltonian H per local scenario \mathcal{E} , and online adaptation performs geometric alignment by updating π_k , $k \in \{s, f, o\}$. This realizes a conservative adaptation principle: systems default to learned physics-based behavior while adding just enough correction to handle new obstacles or map updates, rather than catastrophically relearning policies. Algorithm 1 shows the overall pipeline. Algorithm 2 discuss how to obtain g_ξ offline. The full pseudo-code, including initialization, query protocols, energy assembly, integration details, and adaptation rules, is deferred to Algorithm 3 in Appendix B.

3.1 NAVIGATION AS HAMILTONIAN OPTIMIZATION

From a stagewise constrained optimal control problem to a reduced Hamiltonian system. At a fixed stage τ and local scenario \mathcal{E}_τ , we model motion planning for the deformable robot state $\mathbf{q} \in \mathcal{Q}$ as a *constrained optimal control problem*:

$$\min_{\mathbf{u}(\cdot) \in \mathcal{U}} \int_0^T L(\mathbf{q}(t), \mathbf{u}(t), t; \mathcal{E}_\tau) dt \quad \text{s.t.} \quad \begin{cases} \dot{\mathbf{q}}(t) = \mathbf{v}(\mathbf{q}(t), \mathbf{u}(t), t; \mathcal{E}_\tau), \\ d_i(\mathbf{q}(t); \mathcal{E}_\tau) \geq 0, \quad i = 1, 2, \dots, C(\mathcal{E}_\tau), \\ \mathbf{q}(0) = \mathbf{q}_0, \quad \mathbf{q}(T) = \mathbf{q}_{target}(\mathcal{E}_\tau). \end{cases} \quad (2)$$

Here \mathbf{q}_0 is inherited from the previous stage $\mathcal{E}_{\tau-1}$ (or initialized as $(\mathbf{x}_0, \mathbf{0}, \mathbf{0}, \mathbf{0})$ for $\tau = 1$), and $\mathbf{q}_{target}(\mathcal{E}_\tau)$ is a local goal specified by the stagewise planner. The inequality constraints $d_i(\mathbf{q}; \mathcal{E}_\tau) \geq 0$ encode collision avoidance with the locally sensed geometry; their number $C(\mathcal{E}_\tau)$ and active subset may vary across scenarios. Under standard regularity assumptions, a necessary condition for

¹How to design the best sensory pipeline is out of this paper’s discussion. We assume that sensor can always return the context of environment upon giving its current configuration \mathbf{q} .

Algorithm 1 Online GRL-SNAM pipeline

```

1: Input: goal  $\mathbf{x}_g$ , initial  $z_0 = (q_0, p_0)$  (typically  $p_0=0$ ), step  $\tau$ , horizons  $(T_y, T_f, T_o)$ , max steps  $N_{\max}$ 
2: Init:  $n \leftarrow 0$ , environment  $\mathcal{E}_0$ , environment counter  $\tau \leftarrow 0$  active set  $\mathcal{C}_0 \leftarrow \emptyset$ 
3: Init: meta state  $(\eta_0, \mu_0, u_{f,0})$  from network  $g_\xi$ ,
4: Assemble  $H$  by computing  $g_\xi(\mathcal{E}_0)$ 
5: while  $\neg \text{REACHEDGOAL}(\mathbf{c}_n, \mathbf{x}_g)$  and  $n < N_{\max}$  do
6:   if  $n \equiv 0 \pmod{T_y}$  then
7:     Assemble  $H_y$ , provide  $z_{y,0}$ .
8:     Query Sensor Process via  $\pi_y$  and get response  $\mathbf{R}_y$ 
9:   end if
10:  if  $n \equiv 0 \pmod{T_f}$  then
11:    Assemble  $H_f, u_f^{\xi,n}, \mu_f^{\xi,n}$ , provide  $z_{f,0}$ .
12:    Query Free Path Extractor via  $\pi_f$  and get response  $\mathbf{R}_f$ 
13:  end if
14:  if  $n \equiv 0 \pmod{T_o}$  then
15:    Assemble  $H_o$ , provide  $z_{o,0}$ .
16:    Query Shape Reconfig via  $\pi_o$  and get response  $\mathbf{R}_o$ 
17:  end if
18:  Collect QoIs  $y_n$  from responses  $\mathbf{R}_y, \mathbf{R}_f$  and  $\mathbf{R}_o$ .
19:  Compute correction term  $u_f^{\xi,n}$  via  $y_n$ .
20:  if  $n \equiv 0 \pmod{T_y}$  or reach stage goal then
21:    Update  $\mathcal{E}_{\tau+1}$  via response  $\mathbf{R}_y$ .
22:    Reassemble  $H$  by computing  $g_\xi(\mathcal{E}_{\tau+1})$ 
23:     $\tau \leftarrow \tau + 1$ 
24:  end if
25:   $n \leftarrow n + 1$ 
26: end while
27: Return: trajectory  $\{z_n\}_{n=0}^N$  and parameter history  $\{(\eta_n, \mu_f^{\xi,n}, u_f^{\xi,n})\}_{n=0}^N$ 

```

optimality in Equation (2) is given by the *state-constrained Pontryagin maximum principle(PMP)* (Ferreira & Vinter, 1994; Hartl et al., 1995; Pearson & Sridhar, 1966). We summarize the resulting reduction to a Hamiltonian system below (a formal statement and proof are provided in Theorem A.1).

Lemma 3.1. *Consider Equation (2) and assume: (i) control-affine dynamics $v(\mathbf{q}, \mathbf{u}, t; \mathcal{E}) = f(\mathbf{q}; \mathcal{E}) + A(\mathbf{q}; \mathcal{E}) \mathbf{u}$, (ii) separable running cost $L(\mathbf{q}, \mathbf{u}, t; \mathcal{E}) = \ell(\mathbf{q}; \mathcal{E}) + \varphi(\mathbf{u})$ with φ proper, closed, and strictly convex, and (iii) the regularity/qualification conditions required for the state-constrained maximum principle. Then there exist a costate $p : [0, T] \rightarrow \mathbb{R}^{\dim Q}$ of bounded variation and nonnegative Radon measures $\{\mu_i\}_{i=1}^{C(\mathcal{E}_\tau)}$ such that, defining the reduced Hamiltonian*

$$H_{PMP}(\mathbf{q}, p; \mathcal{E}) := \ell(\mathbf{q}; \mathcal{E}) + p^\top f(\mathbf{q}; \mathcal{E}) + \varphi^*(A(\mathbf{q}; \mathcal{E})^\top p), \quad (3)$$

the optimality conditions can be written (in measure form) as

$$\begin{aligned} \dot{\mathbf{q}}^*(t) &= \nabla_p H_{PMP}(\mathbf{q}^*(t), p(t); \mathcal{E}), \\ dp(t) &= -\nabla_q H_{PMP}(\mathbf{q}^*(t), p(t); \mathcal{E}) dt - \sum_{i=1}^{C(\mathcal{E})} \nabla d_i(\mathbf{q}^*(t); \mathcal{E}) \mu_i(dt). \end{aligned} \quad (4)$$

In particular, on interior intervals where all constraints are inactive, $\mu_i \equiv 0$ and Equation (4) reduces to the classical Hamiltonian system $\dot{\mathbf{q}}^* = \nabla_p H$, $\dot{p} = -\nabla_q H$.

Barrier relaxation and the learnable sub-modular Hamiltonian. For learning and differentiable rollout, we employ a smooth barrier relaxation of the state constraints (Nocedal & Wright, 2006). Let $b_i : \mathbb{R} \rightarrow \mathbb{R}$ be a C^2 barrier potential applied to the clearance $d_i(q; \mathcal{E})$, and let $\alpha_i(\mathcal{E}) \geq 0$

be environment-conditioned weights. Define the *barrier-shaped* running cost

$$L_\alpha(q, u; \mathcal{E}) := \ell(q; \mathcal{E}) + \varphi(u) + \sum_{i=1}^{C(\mathcal{E})} \alpha_i(\mathcal{E}) b_i(d_i(q; \mathcal{E})), \quad (5)$$

which yields an *unconstrained* OCP that approximates Equation (2) as the barriers stiffen. Applying the reduction in Theorem A.2 (quadratic φ and $f \equiv 0$) leads to the PMP Hamiltonian

$$H_{PMP}(q, p; \mathcal{E}) = \frac{1}{2} p^\top M^{-1} p - V(q; \mathcal{E}), \quad V(q; \mathcal{E}) := \ell(q; \mathcal{E}) + \sum_{i=1}^{C(\mathcal{E})} \alpha_i(\mathcal{E}) b_i(d_i(q; \mathcal{E})), \quad (6)$$

where $M \in \mathbb{S}_{++}^2$ is the (learned or fixed) mass/metric induced by the control penalty. We commented on Theorem 3.2 that under certain assumptions log-barrier relaxed OCPs can recover the constrained OCP. The statement of the proposition is inspired from Malisani (2023).

Proposition 3.2 (Barrier relaxation converges to the state-constrained OCP (log-barrier)). *Fix a scenario \mathcal{E} and consider the state-constrained OCP*

$$\begin{aligned} \min_{u(\cdot)} J(u) &:= \int_0^T L(q(t), u(t), t; \mathcal{E}) dt \\ \text{s.t. } \dot{q} &= f(q; \mathcal{E}) + A(q; \mathcal{E})u, \quad d_i(q(t); \mathcal{E}) \geq 0 \quad \forall t, \quad q(0) = q_0, \quad q(T) = q_T. \end{aligned} \quad (7)$$

Assume: (A1) (Slater) there exists a strictly feasible trajectory, i.e., some admissible (\bar{q}, \bar{u}) with $d_i(\bar{q}(t); \mathcal{E}) \geq \delta$ for all $t \in [0, T]$ and all i , for some $\delta > 0$; (A2) f, A, L, d_i are C^2 in q (and L is convex in u), and the constrained OCP admits a (locally) optimal solution (q^, u^*) satisfying a suitable constraint qualification and second-order sufficient conditions.*

For $t > 0$, define the log-barrier relaxed (unconstrained) OCP

$$\min_{u(\cdot)} J_t(u) := \int_0^T \left(L(q(t), u(t), t; \mathcal{E}) + \frac{1}{t} \sum_{i=1}^{C(\mathcal{E})} \alpha_i(\mathcal{E}) \phi(d_i(q(t); \mathcal{E})) \right) dt, \quad \phi(s) := -\log s,$$

subject only to the dynamics and boundary conditions (and implicitly $d_i(q(t); \mathcal{E}) > 0$ due to ϕ). Let (q^t, u^t) be a (locally) optimal solution of the barrier subproblem.

Then:

1. (Strict feasibility) For each t , $d_i(q^t(t); \mathcal{E}) > 0$ for all $t \in [0, T]$ and all i .
2. (Convergence of primal variables) Any sequence $t_k \rightarrow \infty$ has a subsequence (not relabeled) such that (q^{t_k}, u^{t_k}) converges (in a topology appropriate for the OCP, e.g. $q^{t_k} \rightarrow q^*$ strongly and $u^{t_k} \rightharpoonup u^*$ weakly) to a (locally) optimal solution (q^*, u^*) of the original state-constrained OCP.
3. (Recovery of multipliers) Define the barrier-induced (approximate) multipliers

$$\lambda_i^t(\tau) := \frac{\alpha_i(\mathcal{E})}{t} \frac{1}{d_i(q^t(\tau); \mathcal{E})} \geq 0.$$

Along the same subsequence, $\lambda_i^{t_k}$ converges (weakly*) to a nonnegative multiplier λ_i^* appearing in the state-constrained PMP/KKT system of the original OCP; moreover complementarity holds in the limit: $\lambda_i^*(\tau) d_i(q^*(\tau); \mathcal{E}) = 0$ for a.e. τ .

Proof. Defer to Theorem A.3. □

Our geometric reinforcement learning framework. GRL-SNAM learns a scenario-to-energy map $\mathcal{E} \mapsto H(\cdot; \mathcal{E})$. With a costate initialized, the resulting phase-space integrator $x_{t+1} = \Phi_\eta^{\Delta t}(x_t; \mathcal{E})$ with $x_t = (q_t, p_t)$ produces a feasible start-to-goal rollout using only forward passes. We view our proposed method as an Energy-Based Model (Hopfield, 1982; Ackley et al., 1985; LeCun et al., 2006) yet with augmented search space considering geometric structure of energy

landscape (Nguyen & Bajaj, 2025b; Ryan et al., 2025; McLennan et al., 2025). For deterministic dynamics $\dot{q} = f(q) + A(q)u$ and cost minimization, the value function satisfies the HJB equation

$$-\partial_t \mathcal{V}^*(t, q; \mathcal{E}) = \inf_{u \in U} \left\{ L(q, u; \mathcal{E}) + \nabla_q \mathcal{V}^*(t, q; \mathcal{E})^\top (f(q) + A(q)u) \right\}, \quad \mathcal{V}^*(T, q; \mathcal{E}) = \delta_{qT}(q).$$

When \mathcal{V}^* is smooth, the PMP costate admits the feedback representation $p(t) = \nabla_q \mathcal{V}^*(t, q(t); \mathcal{E})$ but one needs to solve the space-time PDE backward in time. Conventional RL methods approximate \mathcal{V}^* via Bellman recursion/backups, and explore its stochastic counterpart. Our design principle is that the optimal motion could be generated by a forward dynamics. To this end, we propose to learn a generalized Hamiltonian dynamical system whose reduced Hamiltonian is defined as:

$$H(q, p; \mathcal{E}) = \frac{1}{2} p^\top M^{-1} p + \mathcal{R}(q; \mathcal{E}), \quad \mathcal{R}(q; \mathcal{E}) := \ell(q; \mathcal{E}) + \sum_{i=1}^{C(\mathcal{E})} \alpha_i(\mathcal{E}) b_i(d_i(q; \mathcal{E})). \quad (8)$$

The sign of potential term is reversed as we are approximating the feedforward dynamics using $\nabla_q H$, and the flow reversibility is addressed in Theorem A.8. It lies in the least action principle energy space we want to search, and we address the search space immediately below.

Search space for the Hamiltonian. The Hamiltonian defined in Equation (8) is a function on the cotangent bundle T^*Q :

$$H \in \mathcal{H} := \left\{ H(q, p; \mathcal{E}) = \frac{1}{2} p^\top M^{-1} p + \mathcal{R}(q; \mathcal{E}) \mid M \in \mathbb{S}_{++}^2, \mathcal{R} \in \mathcal{R} \right\}.$$

We regard \mathcal{R} as a Hilbert space containing admissible potentials. For 2d navigation we *restrict* the potential space $\mathcal{R} \cong \mathbb{R}^{|\mathcal{E}|}$ by defining a parametrized map $\mathcal{E} \rightarrow \eta_\xi(\mathcal{E})$ producing nonnegative dual weights that shape the primal potential. This particular choice is compatible with soft barrier potential addition addressed in Equation (8). In general, each energy term may itself be parametrized:

$$\begin{aligned} H(q, p; \omega, \xi, \mathcal{E}) &= \frac{1}{2} p^\top M(\omega_M)^{-1} p + \mathcal{R}(q; \omega, \eta_\xi(\mathcal{E})), \\ \mathcal{R}(q; \omega, \eta_\xi(\mathcal{E})) &= E_{\text{sensor}}(q; \mathcal{E}, \omega_y) + \beta(\mathcal{E}) E_{\text{goal}}(q; \mathcal{E}, \omega_g) + \lambda(\mathcal{E}) E_{\text{obj}}(q; \omega_d) \\ &+ \sum_{i \in \mathcal{C}(\mathcal{E}, q)} \alpha_i(\mathcal{E}) b(d_i(q; \mathcal{E}); \omega_b), \end{aligned} \quad (9)$$

with $\eta_\xi(\mathcal{E}) = (\beta(\mathcal{E}), \lambda(\mathcal{E}), \{\alpha_i(\mathcal{E})\}) \in \mathbb{R}_+^{m(\mathcal{E})}$. Here $\omega = (\omega_y, \omega_M, \omega_g, \omega_d, \omega_b)$ are *intra-term* parameters (e.g. metric, goal shape, deformation model, barrier template), while η_ξ learns the *inter-term* tradeoffs by mapping the environment \mathcal{E} to dual weights. The cardinality $m(\mathcal{E}) = 2 + |\mathcal{C}(\mathcal{E}, q)|$ is environment/active-set dependent, so η_ξ is implemented with a permutation-invariant set encoder that outputs per-constraint scores $\alpha_i(\mathcal{E}, t) \geq 0$, together with scalars $\beta(\mathcal{E}), \lambda(\mathcal{E}) \geq 0$. The active set $\mathcal{C}(\mathcal{E}, q) := \{i \mid d_i(q, \mathcal{E}) \leq \hat{d}\}$ is discovered online by sensing. We explain role of each potential term in Figure 5.

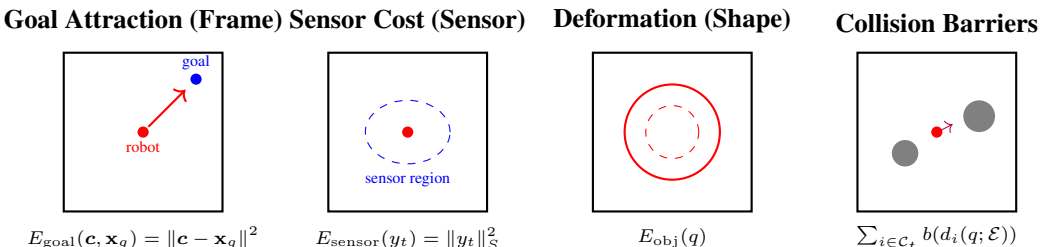


Figure 5: Policy-aligned energy decomposition in GRL–SNAM. The sensor policy exposes a sensor configuration cost E_{sensor} , the frame policy induces goal attraction E_{goal} , and the shape policy contributes deformation energy E_{obj} , while all modules share collision barrier terms $b(d_i)$ around active constraints \mathcal{C}_t . A meta-policy g_ξ assigns weights $(\beta, \lambda, \{\alpha_i\})$ to these components to form the surrogate potential $\mathcal{R}(q; \eta_\xi^t, \mathcal{E}) = E_{\text{sensor}} + \beta^t E_{\text{goal}} + \lambda^t E_{\text{obj}} + \sum_{i \in \mathcal{C}_t} \alpha_i^t b(d_i(q; \mathcal{E}))$ used in the Hamiltonian dynamics.

3.2 NAVIGATOR SCORE FIELDS AND CONTEXT-CONDITIONED POLICIES.

Rather than learning a single monolithic mapless navigation policy, we decompose each module of robots by a small collection of *module score fields* defined on phase space. Each module is a context-conditioned Hamiltonian system: its energy induces a vector field, and the time- Δt flow map of that vector field serves as the module’s policy operator.

Sub-Modular score fields and induced policies. Let $\mathcal{K} = \{y, f, o\}$ index the sensor, frame, and shape modules. For each $k \in \mathcal{K}$, let Q_k denote its configuration manifold and let $\mathcal{Z}_k := T^*Q_k$ be its phase space with state $z_k = (q_k, p_k)$, where $q_k \in Q_k$ and $p_k \in T_{q_k}^*Q_k$ is the conjugate costate. Let $\theta_k \in \Theta_k$ denote the module-specific parameters, and assume the parameter sets are disjoint: $\Theta_i \cap \Theta_j = \emptyset$ for all $i \neq j$. Let $\mathcal{E} \in \mathcal{E}$ denote a local environment context (e.g., a local observation patch together with a goal descriptor). We model the module energy by a differentiable Hamiltonian surrogate

$$h_k^{\theta_k} : \mathcal{Z}_k \times \mathcal{E} \times \mathbb{R}_{\geq 0} \rightarrow \mathbb{R}, \quad (z_k, \mathcal{E}, t) \mapsto h_k^{\theta_k}(z_k; \mathcal{E}, t),$$

where t denotes the (local) integration time within a short rollout horizon. Given a context-conditioned damping matrix $\Gamma_k^\xi(q_k; \mathcal{E}) \succeq 0$ and a nonconservative input $G_k^\xi(q_k; \mathcal{E}) u_k^\xi(z_k, t; \mathcal{E})$, we define the *modular score field* (deterministic drift) as the differential Hamiltonian

$$s_k^{\theta_k, \xi}(z_k, t; \mathcal{E}) := \begin{bmatrix} \nabla_{p_k} h_k^{\theta_k}(z_k; \mathcal{E}, t) \\ -\nabla_{q_k} h_k^{\theta_k}(z_k; \mathcal{E}, t) \end{bmatrix} + \begin{bmatrix} 0 \\ -\Gamma_k^\xi(q_k; \mathcal{E}) \nabla_{p_k} h_k^{\theta_k}(z_k; \mathcal{E}, t) + G_k^\xi(q_k; \mathcal{E}) u_k^\xi(z_k, t; \mathcal{E}) \end{bmatrix}. \quad (10)$$

The modular stagewise dynamics are the ODE $\dot{z}_k = s_k^{\theta_k, \xi}(z_k, t; \mathcal{E})$. Fix an integration rule with step size $\Delta t > 0$ and denote by $\Phi_k^{\Delta t}(\cdot; \mathcal{E}) : \mathcal{Z}_k \rightarrow \mathcal{Z}_k$ its time- Δt flow map. We define the (deterministic) *context-conditioned modular policy* as the rollout operator

$$\pi_k^{\theta_k, \xi}(\mathcal{E}) := \Phi_k^{\Delta t}(\cdot; \mathcal{E}), \quad z_{k, t+\Delta t} = \pi_k^{\theta_k, \xi}(\mathcal{E})(z_{k, t}). \quad (11)$$

If $\Gamma_k^\xi \equiv 0$ and $u_k^\xi \equiv 0$, then $s_k^{\theta_k, \xi}$ reduces to the Hamiltonian vector field and $\pi_k^{\theta_k, \xi}(\mathcal{E})$ is symplectic; otherwise it remains a (local) diffeomorphism under standard Lipschitz regularity but is generally non-symplectic.

The disjointness of parameter sets implies $\partial s_k^{\theta_k, \xi} / \partial \theta_j \equiv 0$ for all $j \neq k$, so the intra-modular energies can be trained in parallel while coordination is enforced through shared context-dependent constraints and shared dual weights.

Template Sub-modular Hamiltonians and shared dual weights. We couple modules through a shared mechanical energy family and context-conditioned potential reshaping. Let $\eta(\mathcal{E}) = \eta_\xi(\mathcal{E}) \in \mathbb{R}_+^{m(\mathcal{E}, t)}$ denote the nonnegative dual weights produced by the navigator’s context encoder, with components $\eta(\mathcal{E}) = (\beta(\mathcal{E}), \lambda(\mathcal{E}), \{\alpha_i(\mathcal{E}, t)\}_{i \in \mathcal{C}_t})$. The active constraint set $\mathcal{C}_t(\mathcal{E}, q) := \{i \mid d_i(q; \mathcal{E}) \geq 0\}$ is discovered online by sensing. For each $k \in \mathcal{K}$ we use a mechanical template

$$H_k(q_k, p_k; \mathcal{E}) = \frac{1}{2} p_k^\top M^{-1} p_k + \mathcal{R}_k(q_k; \eta(\mathcal{E}), \mathcal{E}), \quad h_k^{\theta_k}(z_k; \mathcal{E}, 0) = H_k(z_k; \mathcal{E}). \quad (12)$$

and instantiate the context-shaped potentials

$$\mathcal{R}_y(q_y; \eta, \mathcal{E}) = E_{\text{sensor}}(q_y; \mathcal{E}, \omega_y) + \sum_{i \in \mathcal{C}_t(\mathcal{E}, q_y)} \alpha_i(\mathcal{E}, t) b(d_i(q; \mathcal{E}); \omega_b), \quad (13)$$

$$\mathcal{R}_f(q_f; \eta, \mathcal{E}) = \beta(\mathcal{E}) E_{\text{goal}}(q_f; \mathcal{E}, \omega_g) + \sum_{i \in \mathcal{C}_t(\mathcal{E}, q_f)} \alpha_i(\mathcal{E}, t) b(d_i(q; \mathcal{E}); \omega_b), \quad (14)$$

$$\mathcal{R}_o(q_o; \eta, \mathcal{E}) = \lambda(\mathcal{E}) E_{\text{obj}}(q_o; \omega_d) + \sum_{i \in \mathcal{C}_t(\mathcal{E}, q_o)} \alpha_i(\mathcal{E}, t) b(d_i(q; \mathcal{E}); \omega_b). \quad (15)$$

Here $\omega = (\omega_y, \omega_g, \omega_d, \omega_b)$ collects intra-term parameters, while $\eta(\mathcal{E})$ controls inter-term tradeoffs via nonnegative weights.

Sub-modular responses and aggregation. Each module integrates its phase dynamics over a short horizon and returns a standardized response map R_k to the navigator. The navigator aggregates these responses to update $\eta_\xi(\mathcal{E})$ (and, when enabled, damping/correction parameters) and to generate stable trajectories across stages.

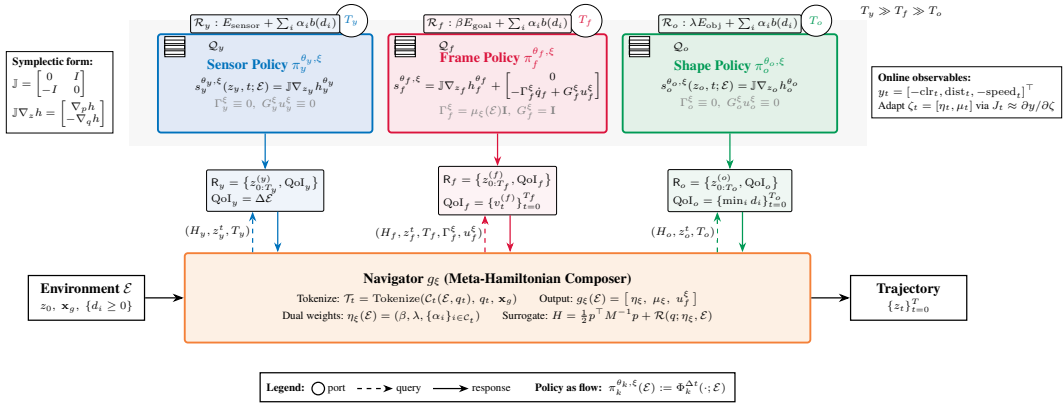


Figure 6: Modular score-field architecture for GRL-SNAM. The Navigator g_ξ tokenizes active constraints \mathcal{C}_t , state q_t , and goal \mathbf{x}_g , then outputs dual weights $\eta_\xi = (\beta, \lambda, \{\alpha_i\})$, friction μ_ξ , and port correction u_ξ^f . Each module $k \in \{y, f, o\}$ integrates its score field $s_k^{\theta_k, \xi} = \mathbb{J} \nabla_{z_k} h_k^{\theta_k}$ (plus non-conservative terms for the frame module) over horizon T_k and returns response R_k with phase-space rollouts and QoIs. The frame module uniquely receives dissipation Γ_f^ξ and port input u_f^ξ ; sensor and shape modules have purely symplectic dynamics.

3.3 GRL-SNAM OFFLINE TRAINING AND ONLINE ADAPTATION

The GRL-SNAM operates as a meta-learning system that coordinates multi-scale policies by learning how to update their Hamiltonian energy functions rather than directly manipulating phase space states.

Choice of Hamiltonian and Hamiltonian dynamics Throughout the paper we further simplify our navigator’s Hamiltonian surrogate by assuming fixed ω throughout all environment when we primarily focus on learning to optimize the environment-indexed linear cone generated by task energies. The potential energy is denoted as follows and is shown in Figure 5:

$$\begin{aligned} \mathcal{R}(q; \eta(\mathcal{E})) = & \underbrace{\|\mathbf{y}\|_S^2}_{\text{Sensor Cost } (E_{\text{sensor}})} + \underbrace{\beta \|\mathbf{c} - \mathbf{x}_g\|_2^2}_{\text{Goal Attraction } (E_{\text{goal}})} \\ & + \underbrace{\lambda E_{\text{obj}}(q(t))}_{\text{Deformation Energy } (E_{\text{obj}})} + \underbrace{\sum_{i \in \mathcal{C}_t(\mathcal{E}, q)} \alpha_i b(d_i, \hat{d})}_{\text{Collision Barriers } (\text{FPE})}. \end{aligned} \quad (16)$$

In addition, we assume friction and additional forces (e.g. derived from safety constraints) are happened in FPE submodule only, and we pick a particular parametrization as:

$$\begin{aligned} \Gamma_y^\xi &\equiv 0, \quad G_y^\xi \equiv 0, \quad u_y^\xi \equiv 0, \\ \Gamma_f^\xi &= \mu_\xi(\mathcal{E}) \mathbf{I}, \quad G_f^\xi = \mathbf{I}, \quad u_f^\xi \neq 0, \\ \Gamma_o^\xi &\equiv 0, \quad G_o^\xi \equiv 0, \quad u_o^\xi \equiv 0, \end{aligned} \quad (17)$$

Thus the meta policy g_ξ directly produces the cone coordinates of potentials and non-conservative forces correction in FPE module as a friction and a port correction term:

$$g_\xi(\mathcal{E}) = [\eta_\xi(\mathcal{E}), \mu_\xi(\mathcal{E}), u_f^\xi], \quad (18)$$

which defines the potential—and therefore the generalized force—for the stagewise motion-planning Hamiltonian rollouts. Learning g_ξ gives a *meta-policy* that maps environments to energy weights, i.e. a stagewise bilevel scheme where the inner layer optimizes motion under H_k and the outer layer trains ξ so that scenario-level QoIs/constraints are satisfied across environments.

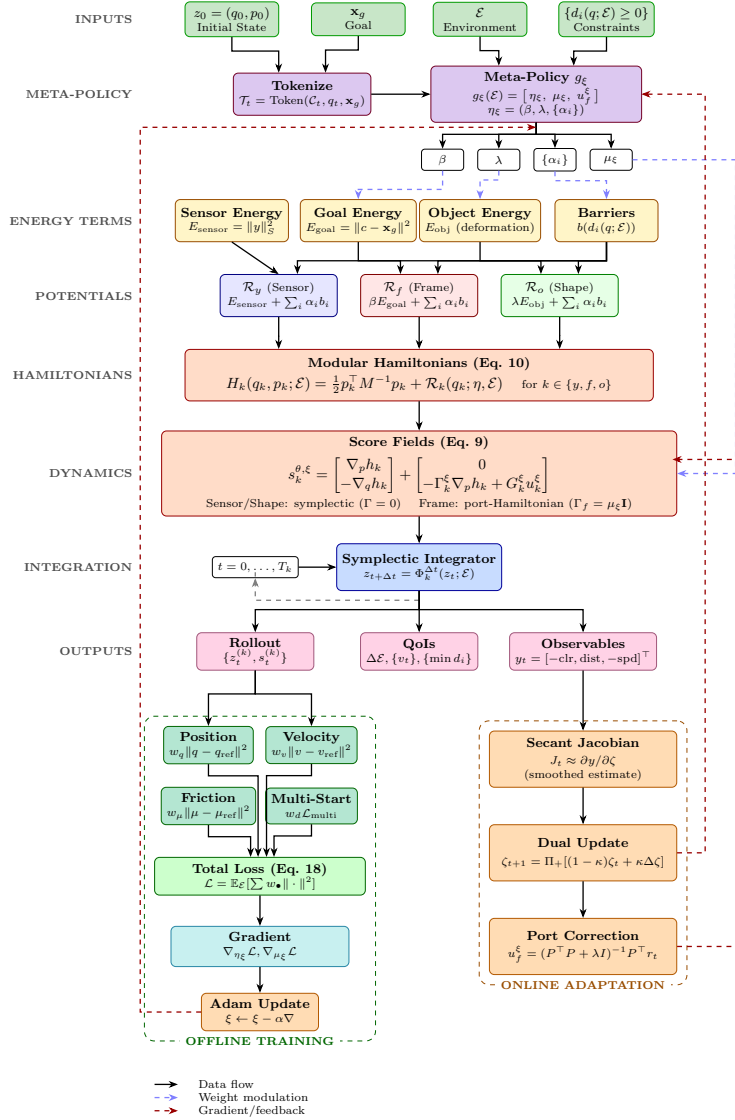


Figure 7: **GRL-SNAM computational flow: sub-modular Hamiltonian structure with offline training and online adaptation.** Given the current state $z_0 = (q_0, p_0)$, goal x_g , and locally sensed environment context \mathcal{E} (obstacle constraints $\{d_i(q; \mathcal{E}) \geq 0\}$), the navigator g_ξ tokenizes the active local information and outputs a small set of *meta-parameters*: the nonnegative energy weights $\eta_\xi = (\beta, \lambda, \{\alpha_i\})$, the frame dissipation μ_ξ , and an optional frame port input u_f^ξ . These parameters modulate a fixed library of interpretable energy terms (sensor cost, goal attraction, deformation, and barrier penalties) to form module-specific potentials $\mathcal{R}_y, \mathcal{R}_f, \mathcal{R}_o$, which define the corresponding modular Hamiltonians $H_k(q_k, p_k; \mathcal{E}) = \frac{1}{2} p_k^T M^{-1} p_k + \mathcal{R}_k(q_k; \eta_\xi, \mathcal{E})$ (c.f. Equation (12)). Each module induces a score (drift) field; sensor and shape follow conservative (symplectic) dynamics, while the frame module additionally includes dissipation and a nonconservative port term. A symplectic integrator rolls out the dynamics for a short horizon, producing trajectories and quantities of interest (environment updates, velocities, and clearances) as well as low-dimensional observables $y_t = [-\text{clr}_t, \text{dist}_t, -\text{spd}_t]^\top$. *Offline training* (left branch) learns the mapping from context to meta-parameters by minimizing a supervised loss on position/velocity/friction, augmented with a multi-start robustness term near obstacles. *Online adaptation* (right branch) updates only the current meta-parameters using a smoothed secant Jacobian estimate to track the desired observables, and uses the residual to compute a corrective port input when energy reweighting alone is insufficient. Arrows indicate (i) forward data flow, (ii) weight modulation from g_ξ into energies, and (iii) gradient/feedback pathways connecting rollouts to offline updates and online corrections.

Learning $\eta_\xi(\mathcal{E})$, $\mu_\xi(\mathcal{E})$ through observation of Hamiltonian dynamics. Each submodule exposes a response map that provides integrated dynamics rollout and additional quantity of interests (QoI) as the feedback:

$$\mathbf{R}_k : (H_k; \theta_k, \mathcal{E}, \xi) \mapsto \{z_t^{(k)}, \text{QoI}_k\}_{t=0}^{T_k}, \quad k \in \mathcal{K},$$

where T_k refers time scale for each submodule. To be more specific:

$$\text{QoI}_y = \Delta\mathcal{E}, \quad \text{QoI}_f = \{v_t^{(f)} := M_f^{-1} p_t^{(f)}\}_{t=0}^{T_f}, \quad \text{QoI}_o = \{\min_{i \in \mathcal{C}_t(\mathcal{E}, q)} d_i(q_t^{(o)}; \mathcal{E})\}_{t=0}^{T_o}. \quad (19)$$

Namely, feedback QoIs are: environmental update, velocity observation, and min distance clearance (and thus collision violation). Additional QoIs, that can be deduced from $z_t^{(k)}, s_t^{(k)}$, are not stated here explicitly. To train a policy that output $\eta_\xi(\mathcal{E})$ and $\mu_\xi(\mathcal{E})$ with different environments, we propose to minimize

$$\mathcal{L}(\eta_\xi, \mu_\xi) = \mathbb{E}_{\mathcal{E}} \left[w_q \|\mathbf{q} - \mathbf{q}_{ref}\|_2^2 + w_v \|\mathbf{v} - \mathbf{v}_{ref}\|_2^2 + w_\mu \|\mu - \mu_{ref}\|_2^2 + w_d \mathcal{L}_{\text{multi}} \right]. \quad (20)$$

where $\mathcal{L}_{\text{multi}}$ is a short multi-start robustness penalty that re-rolls from perturbed $q_t^{(k)}$ seeds near obstacles to discourage brittle $\eta_\xi(\mathcal{E})$ and $\mu_\xi(\mathcal{E})$ (details are addressed in Algorithm 2), and $w_\bullet \geq 0$ are user-input hyperparameters. The training via Equation (20) can be conducted offline, component-wise, or even fine-tuned online, but we state that it is important to fully utilize the instantaneous response from a real navigation scenario which provides the scheme of per-scenario online correction even when $\eta_\xi(\mathcal{E})$ and $\mu_\xi(\mathcal{E})$ are properly trained under large-scale simulated dataset with reference potentials.

Algorithm 2 Offline GRL-SNAM training of $\eta(\mathcal{E})$ and $\mu_\xi(\mathcal{E})$

Require: dataset of different environments $\{\mathcal{E}, \alpha_{ref}, \beta_{ref}, \lambda_{ref}, \mu_{ref}\} \in \mathcal{D}$, step range $T \in \{2, 3, 4, 5, 6\}$, short rollout trials M , time step Δt , weights w_\bullet

- 1: Initialize ξ
- 2: **for** epoch = 1, 2, … **do**
- 3: **for** batch $\mathcal{B} \subset \mathcal{D}$ **do**
- 4: Sample (q_0, p_0) per scene \mathcal{E} in \mathcal{B}
- 5: Build **tokens** from active constraints $\mathcal{C}_t(\mathcal{E}, q_0)$, goal x_g , and current (q_0, p_0)
- 6: $(\{\alpha_j\}, \beta) \leftarrow \eta_\xi(\mathbf{tokens})$, $\mu \leftarrow \mu_\xi(\mathbf{tokens})$
- 7: **for** $m = 1, 2, \dots, M$ **do**
- 8: Sample a near obstacle point \tilde{q}_0 , initialize \tilde{p}_0 towards nearest obstacle at \tilde{q}_0 .
- 9: Integrate Equation (10) for T steps from $(\tilde{q}_0, \tilde{p}_0)$.
- 10: Compute $clr \leftarrow \min_{i,t} d_i(\tilde{q}_t; \mathcal{E})$ ▷ e.g. Leapfrog
- 11: Compute $\mathcal{L}_{\text{multi}} \leftarrow \mathcal{L}_{\text{multi}} + \frac{1}{M} b \left(r_{min} - clr, \hat{d} \right)$.
- 12: ▷ r_{min} refers minimal radius of robot object.
- 13: **end for**
- 14: Integrate Equation (10) for T_k steps from (q_0, p_0)
- 15: Evaluate loss $\mathcal{L}(\eta_\xi, \mu_\xi)$ in Equation (20)
- 16: Update η_ξ, μ_ξ using $\nabla_{\eta_\xi} \mathcal{L}$ and $\nabla_{\mu_\xi} \mathcal{L}$ ▷ Uncertainty hyperparameter weighted
- 17: **end for**
- 18: **end for**
- 19: **end for**

Online Adaptation of $g_\xi(\mathcal{E})$ via QoIs We state how response map for each environment can yield a correction term under online navigation scenario. Given response \mathbf{R}_k at time t we construct an *observable* measurement vector and its reference goal:

$$y_t = \begin{bmatrix} -clr_t \\ \text{dist}_t \\ -\text{speed}_t \end{bmatrix} \in \mathbb{R}^3, \quad y_t^* = \begin{bmatrix} -m_{\text{safe}} \\ \text{dist}_t - \varepsilon_{\text{prog}} \\ -\max(\text{speed}_t, \mathbf{1}_{\{clr_t \geq m_{\text{safe}}\}} v_{\text{min}}) \end{bmatrix},$$

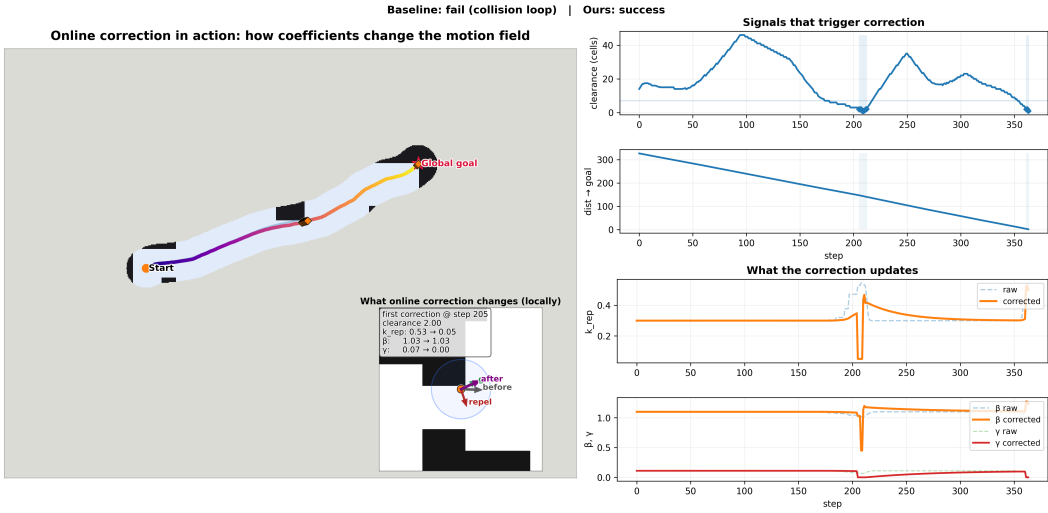


Figure 8: **Online correction mechanism (Sec. 3.3).** Left: a representative rollout where the frozen baseline enters a collision loop, while GRL-SNAM reaches the global goal by applying local corrections at detected failure points; the inset visualizes the first correction as a change in the local motion field (goal-seeking plus obstacle repulsion) around the active obstacles. Right: the observable vector $y_t = [-\text{clr}_t, \text{dist}_t, -\text{speed}_t]^\top$ used for triggering/adaptation, with shaded bands marking correction events. Bottom-right: the corresponding parameter updates i.e.; the dual weights $\tilde{\eta}_t = [\beta_t, \lambda_t, \alpha_{t, \mathcal{I}_t}]^\top$ (active-set barrier weights) and dissipation/port terms $(\mu_t, u_{f,t}^\xi)$ show how the navigator performs lightweight, stage-local updates to the Hamiltonian-shaped policy to restore safety (clearance) while maintaining goal progress.

where clr is the minimum clearance to inflated obstacles, dist is goal distance (to the global goal point), and $\text{speed} = \|v\|$. We update only the *active* barrier weights by selecting an index set \mathcal{I}_t that represents nearby obstacles. Define the parameter vector

$$\tilde{\eta}_t = \begin{bmatrix} \beta_t \\ \lambda_t \\ \alpha_{t, \mathcal{I}_t} \end{bmatrix} \in \mathbb{R}_+^{2+|\mathcal{I}_t|}, \quad \zeta_t = [\tilde{\eta}_t, \mu_t].$$

We denote an estimator of Jacobian $J_t = \frac{\partial y}{\partial \zeta_t}$ as

$$\tilde{J}_t = \frac{(y_t - y_{t-1})(\zeta_t - \zeta_{t-1})^\top}{\|\zeta_t - \zeta_{t-1}\|_2^2 + \varepsilon}, \quad J_t = \rho J_{t-1} + (1 - \rho) \tilde{J}_t,$$

with smoothing $\rho \in [0, 1]$ and $\varepsilon > 0$. Then, given the desired observable change $\Delta y_t^{\text{des}} := y_t^* - y_t$, one can update meta-policy parameter via a Tikhonov-regularized least square steps:

$$\Delta \zeta_t = \arg \min_{\Delta \zeta} \|J_t \Delta \zeta - \Delta y_t^{\text{des}}\|_2^2 + \lambda \|\Delta \zeta\|_2^2, \quad \Rightarrow \quad \Delta \zeta_t = (J_t^\top J_t + \lambda I)^{-1} J_t^\top \Delta y_t^{\text{des}}.$$

This yields updated β_{t+1} , γ_{t+1} , and $\alpha_{t+1,i}$ for $i \in \mathcal{I}_t$ (inactive weights keep their previous values).

$$\zeta_{t+1} = \Pi_{\mathbb{R}_+}((1 - \kappa) \zeta_t + \kappa \Delta \zeta_t), \quad \kappa_i \in [0, 1].$$

Since the update is a result of least square step, there exists residual:

$$r_t = \Delta y_t^{\text{des}} - J_t \Delta \zeta_t.$$

The online port correction term can amend the energy change by solving another least square problem given port-observable sensitivity $P_t \approx \partial y / \partial u_f$:

$$u_{f,t}^\xi = \arg \min_{u \in \mathcal{U}} \|P_t u - r_t\|_2^2 + \lambda_u \|u\|_2^2 = (P_t^\top P_t + \lambda_u I)^{-1} P_t^\top r_t,$$

followed by componentwise clipping to a feasible box \mathcal{U} . A simple choice is to use $P_t = \text{diag}(0, 0, \kappa_v)$ so that the port primarily regulates speed while the energy weights steer clearance and goal progress. We comment that richer P_t can be learned online by the same secant recipe as J_t .

Multi-Scale Temporal Coordination The policies operate at natural temporal hierarchies, creating stable multi-scale coordination, as shown in Figure 9. This temporal separation enables a **nested quasi-static approximation**: the fastest dynamics (reconfiguration) equilibrate within each frame update, and frame dynamics settle before the slower sensor policy evolves. This hierarchy prevents destabilizing interactions across timescales while preserving the necessary coupling for coherent, coordinated behavior.

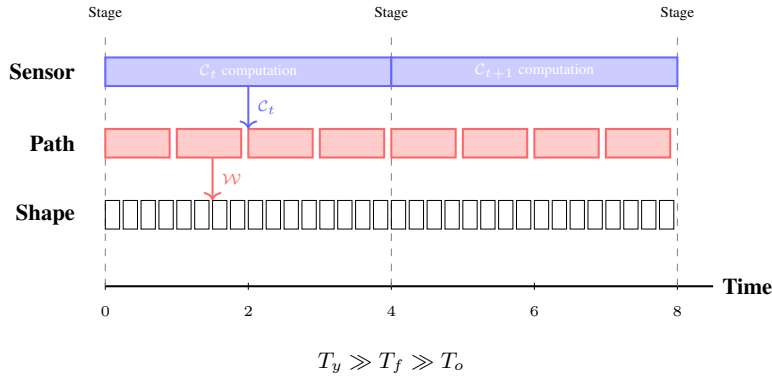


Figure 9: Temporal hierarchy. Sensor policy operates at low frequency (once per stage), establishing environmental constraints C_t . Path policy operates at medium frequency within each stage, computing waypoints \mathcal{W} . Shape policy operates at high frequency, continuously adapting at each integration step. This creates a natural hierarchy where slow sensor updates provide stable constraints for faster path and shape adaptations.

4 HYPERELASTIC RING ROBOT MODEL

Our framework in Sec. 3 is agnostic to the underlying robot body: the score-based policies $\{\pi_y, \pi_f, \pi_o\}$ only assume access to a local context \mathcal{C}_t , a reduced state z_t and a modular hamiltonian proposal. For experiments, we instantiate this framework on a planar *hyperelastic ring* that must squeeze through clutter and narrow passages. In this domain, the shape policy π_o acts on a low-dimensional shape state

$$z_o(t) = (s(t), p_s(t)),$$

where $s(t) > 0$ is a uniform scale, and one denote $\mathbf{o}(t) \in \mathbb{R}^2$ as the ring center coincide with robot frame center \mathbf{c} .

Design rationale. We choose a hyperelastic ring with a spline boundary for three reasons that match the Hamiltonian formulation in Sec. 3: (i) it is the simplest soft body that *provably requires* shape change to solve our benchmarks (a rigid disc of any fixed radius cannot pass through the same bottlenecks), so deformation and collision-clearance trade-offs cannot be “faked” by rigid planning alone; (ii) the reduced state s provides a low-dimensional, analytically tractable testbed for the energy decomposition in Equation (12), letting us study Hamiltonian energy shaping and meta-weights ($\beta, \lambda, \{\alpha_i\}$) without confounding internal DOF; and

Thus, the hyperring model is not a restriction of GRL-SNAM, but a controlled, low-DOF instantiation that stresses exactly the squeezing and clearance behaviors we target.

Geometric Representation of Hyperelastic Ring We represent the boundary of the hyperelastic ring object by a periodic cubic B-spline with n_{ctrl} control points

$$\mathbf{S}(u) = \sum_{i=1}^{n_{\text{ctrl}}} N_{i,3}(u) \mathbf{P}_i, \quad u \in [0, 1], \quad (21)$$

where $N_{i,3}$ are C^2 -continuous B-spline basis functions. This choice provides a smooth closed curve with well-defined normals and curvature, and allows fast evaluation through precomputed matrices.

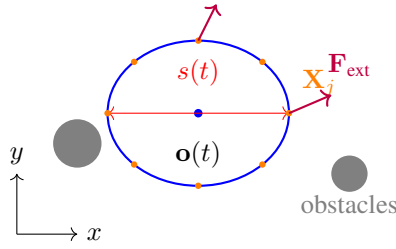


Figure 10: Hyperelastic ring instantiation of the generic shape policy π_o . The reduced configuration s is mapped to spline samples \mathbf{X}_j where policy-induced forces act.

A reference unit ring is initialized as

$$\mathbf{P}_{0,i} = r_{\text{base}} \begin{bmatrix} \cos(2\pi i/n_{\text{ctrl}}) \\ \sin(2\pi i/n_{\text{ctrl}}) \end{bmatrix}, \quad (22)$$

and transformed to world coordinates by a similarity transform $\mathbf{P}_i(t) = \mathbf{o}(t) + s(t) \mathbf{P}_{0,i}$. For numerical evaluation we precompute spline matrices $B, D \in \mathbb{R}^{K \times n_{\text{ctrl}}}$ and sample K points on the boundary

$$\mathbf{X}_j(t) = \sum_i B_{ji} \mathbf{P}_i(t), \quad \mathbf{X}'_j(t) = \sum_i D_{ji} \mathbf{P}_i(t), \quad (23)$$

with arc lengths $\ell_j = \|\mathbf{X}'_j\|$ and unit tangents $\hat{\mathbf{T}}_j = \mathbf{X}'_j / \ell_j$. We use uniform quadrature weights $\omega_j = 1/K$.

Shape Sub-Modular Hamiltonian. In this domain, the generic Hamiltonian from Equation (12) specializes to

$$\mathcal{H}_o(z_o; \mathcal{E}_\tau) = \frac{1}{2} M_s^{-1} p_s^2 + \mathcal{R}_o(q_o; \mathcal{E}_t), \quad (24)$$

where M_s refers a fixed “mass” term of scale and $p_s = M_s^{-1} \dot{s}$ refers conjugate momenta. We match the navigation specialization in Equation (15) by defining the barrier potentials $b(d_i(q, \mathcal{E}))$ and object intrinsic energy E_{obj} for deformation.

Barrier potentials. The sensor policy π_y exposes weighted point obstacles (\mathbf{c}_i, r_i, w_i) in \mathcal{C}_t from \mathcal{E} . Here \mathbf{c}_i denotes the center of objects and r_i denotes the distance. w_i denotes the scale of obstacles. For each sample point \mathbf{X}_j we compute distances $d_{ji} = \|\mathbf{X}_j - \mathbf{c}_i\| - r_i$, and accumulate an Incremental Potential Contact (IPC, Li et al. (2020b)) barrier function:

$$d_i(q, \mathcal{E}) := \sum_{j=1}^K \omega_j \ell_j w_k b_{\text{IPC}}(d_{jk}; \hat{d}), \quad (25)$$

with $b_{\text{IPC}}(\cdot)$ in the standard piecewise form

$$b_{\text{IPC}}(d; \hat{d}) = \begin{cases} -(d - \hat{d})^2 (\log d - \log \hat{d}) & 0 < d < \hat{d}, \\ 0 & d \geq \hat{d}, \\ V_{\text{penalty}} & d \leq 0. \end{cases} \quad (26)$$

The term \hat{d} refers the contact distance thresholding while V_{penalty} is a user-specified constant that penalize penetration. This is a concrete instantiation of the barrier term in Equation (5), with IPC chosen because its differential yields near obstacle contact forces and time integrations resembles physical-world behaviors of an elastic object. We provide Theorem A.4 to justify IPC potentials are also a valid barrier function that maintains the conclusions addressed in Theorem 3.2.

Object potential. Let A_{ref} denote the reference rest area of the ring. We denote the scaled area $A(s) = s^2 A_{\text{ref}}$. We compute the minimal clearance $d_{\min} := \min_{j,i} \{d_{ji}\}$, and use it to define a clearance-dependent scale target

$$s_{\text{target}} := s_0 + (1 - s_0) \tanh(\delta \max(d_{\min}, 0)), \quad (27)$$

which encourages compression in tight passages while keeping the ring expanded in free space: for large d_{\min} , s_{target} shall be close to 1, while for lower clearance the target shrinks smoothly. The bulk potential is thus defined as

$$E_{\text{obj}}(q) := \mathcal{U}_{\text{bulk}}(s; d_{\min}) = \frac{k_{\text{bulk}}}{2} (A(s) - A(s_{\text{target}}))^2. \quad (28)$$

This realizes E_{obj} with a *single* deformation DOF (scale s), striking a balance between expressivity (squeezing is possible) and the low-dimensional Hamiltonian search space assumed in Sec. 3.1. The three policies $\{\pi_y, \pi_f, \pi_o\}$ interact with the ring exactly at the level of boundary samples, in a way that mirrors the abstract modular decomposition of \mathcal{R} .

5 EXPERIMENTAL EVALUATION

We evaluate GRL-SNAM on two navigation benchmarks that share the same *stagewise, local-sensing* interface but differ in dynamics: (i) deformable hyperelastic ring navigation in cluttered workspaces, and (ii) point-agent dungeon navigation derived from Liang et al. (2023). In both tasks, GRL-SNAM receives the state q_t , a stage-exit goal g_t , and obstacles within a local window; task-specific dynamics and energy terms instantiate the reduced Hamiltonian \mathcal{H} .

5.1 TASKS AND ENVIRONMENTS

Stagewise local sensor and mapping effort quantification. At time t , the agent observes obstacles intersecting a local window $\mathcal{W}(q_t)$ of size $2\hat{d} \times 2\hat{d}$ centered at q_t , and a stage signal (macro-cell index) with its current exit goal g_t from a stage manager over a workspace tiling. We quantify sensing effort by the mapping ratio

$$\rho_{\text{map}} := \frac{\text{area}(\bigcup_t \mathcal{W}(q_t))}{L^2}. \quad (29)$$

5.1.1 NARROW-GAP PASSING NAVIGATION TASK WITH A HYPERELASTIC RING ROBOT

Environment. Each instance is a $[0, L] \times [0, L]$ workspace with procedurally sampled circular obstacles (positions/radii/density), spanning bottlenecks, zig-zag corridors, and cul-de-sacs. Start-goal pairs are sampled so that a deformable ring admits a collision-free solution, while a rigid disc of comparable size may not. We construct Train, In distribution Test(**Test-ID**, matched statistics), and Out-of-distribution Test (**Test-OOD**, shifted gap/density) splits.

Dynamics and interface. The robot is a reduced-order hyperelastic ring with Hamiltonian $\mathcal{H}(q, p)$. GRL-SNAM interacts only through $(q_t, g_t, \mathcal{W}(q_t))$ and the resulting generalized forces/coefficients; implementation details of the hyperelastic model are provided in Section 4.

Reduced Hamiltonian used in this task. We use a reduced Hamiltonian whose potential combines a goal term toward g_t and barrier terms from signed distances to locally observed obstacles, with dissipation/regularization. Context encoders predict coefficients (β, γ, α) that modulate these terms.

5.1.2 DUNGEON NAVIGATION VIA A POINT-NAV SYSTEM

Environment and dynamics. We use dungeon layouts from Liang et al. (2023). The agent is a point mass in continuous 2D with state q_t (position; optionally velocity) and action $\mathbf{a}_t = [v_x, v_y] \in [-3, 3]^2$. Collisions with walls are penalized/terminating; reaching the goal yields reward.

Observations (matched to the stagewise interface). A `StagewiseSensor` selects the active macro-cell and exposes its exit as the local goal g_t . An `ObstacleExtractor` fits circular obstacles to wall segments inside $\mathcal{W}(q_t)$, returning centers, radii, and a visibility mask. The observation concatenates stage-relative position, g_t , and the local obstacle set.

Use in evaluation. We instantiate GRL-SNAM with a simple quadratic goal energy and radial barrier energies from the extracted obstacles, and compare to PPO/TRPO/SAC under (i) full-episode long-horizon training and (ii) short-rollout stagewise training with the same observation/action interface as GRL-SNAM.

5.1.3 EXPERIMENTAL SETUPS

We justify our choice of predefined hyperparameters for each task in Table 1 and further explain them in B.13. Most parameters are learnable or sharable across tasks. Only when maps’ scale and robot configurations vary shall one choose additional hyperparameters. Experiments are performed on one NVIDIA A100 GPU with 40 GB VRAM, using Linux operating system, and all networks are trained via PyTorch (Paszke et al., 2019) library. For RL baselines, we adapt PPO, SAC and TRPO algorithms provided in Stable-Baselines3 (Raffin et al., 2021) for comparison.

5.2 BASELINE METHODS

We compare GRL-SNAM against a spectrum of planning and learning methods that differ in (i) map access (full vs. local), (ii) planning scope (global vs. local), and (iii) supervision signal (hand-crafted surrogates vs. learned policies). Below we summarize the baselines and their roles.

5.2.1 BASELINES FOR HYPERELASTIC RING NAVIGATION

For the deformable hyperring task we consider two non-learning families plus our GRL-SNAM controller, all instantiated on the same hyperelastic model.

Global planners (full-map references). Assuming full occupancy grids, these methods provide reference paths and define L_{ref} for SPL and detour:

- **Rigid A***: A* on an obstacle-inflated grid for a rigid disc of radius r_{rest} , yielding conservative collision-free paths that may be overly cautious for a deformable ring.
- **Deformable A***: Clearance-aware A* that augments edge costs with a deformation penalty as clearance approaches a minimum radius r_{min} , allowing squeezing through tight passages at an energetic cost.

Local reactive planners (stagewise, same information as GRL-SNAM). To provide fair local baselines, we instantiate classical controllers that share the *same* stage manager and local window as GRL-SNAM:

- **Potential Fields (PF, staged)**: Attractive potential toward the current stage exit plus repulsive potentials from locally sensed obstacles and stage boundaries.
- **Control Barrier Functions (CBF, staged)**: A nominal control toward the stage exit filtered through a CBF quadratic program using clearance-based barrier functions to enforce local safety.
- **Dynamic Window Approach (DWA, staged)**: Sampling of (v, ω) pairs within dynamics limits, short-horizon rolling, and scoring based on goal alignment, velocity, and clearance with penalties for leaving the active stage.

All three operate under identical sensing and stagewise constraints as GRL-SNAM, but rely on hand-crafted surrogates instead of learned Hamiltonians.

Ours: GRL-SNAM (hyperring instantiation). On the hyperelastic ring, GRL-SNAM uses the reduced Hamiltonian described in Section 3.3 and 4, combining goal, barrier, and dissipation terms

Table 1: Hyperparameter nomenclature and selection across experiments. **Default: fixed.** Parameters marked ^L are learned/predicted by the meta-policy (softplus-enforced nonnegativity where applicable); parameters marked ^{PC} are precomputed.

Block	Symbol	Description	Value / Range
<i>Learned coefficients (variable-dimension ζ_t)</i>			
Barrier	α_j^L	Per-obstacle barrier weight	$\alpha_j \geq 0$ (softplus)
Goal	β^L	Goal attraction strength	$\beta \geq 0$ (softplus)
Damping	γ^L	Linear damping scale	$\gamma \geq 0$ (softplus)
<i>Shared pipeline: loss & optimization</i>			
Opt.	η	Learning rate	1×10^{-4} – 3×10^{-4}
Loss	$w_{\text{traj}}, w_{\text{vel}}$	Position / velocity loss weights	1.0, 1.0
Loss	$w_{\text{fric}}, w_{\text{multi}}$	Damping / multi-start penalty	0.1, 0.5
Rollout	H	Surrogate rollout horizon	2–6 steps
Test-time	λ_{prox}	Proximal regularization	10^{-3}
<i>Shared pipeline: IPC barrier & staging</i>			
Barrier	\hat{d}	Barrier activation distance	0.28–1.0
Barrier	$b(d)$	$-(d - \hat{d})^2 \log(d/\hat{d})$	—
Staging	(W, H)	Stage window dimensions	(2.6, 2.0)
Staging	ρ_{overlap}	Stage overlap ratio	0.3
Geometry	r_{inflate}	Obstacle inflation (tube radius)	0.05–0.4
<i>Hyperelastic ring: dynamics</i>			
Trans.	M_c, γ_c	Robot pose mass / damping	1.5, 4.0
Scale	M_s, γ_s	Scale mass / damping	1.0, 2.0
Material	k_{bulk}	Bulk modulus (area stiffness)	1.5
<i>Hyperelastic ring: geometry</i>			
Shape	r_{robot}	Nominal ring radius	0.30–0.50
Spline	n_{ctrl}, K	B-spline control / sample points	20, 240
Time	Δt	Integration timestep	0.03
<i>Dungeon: FPE navigation</i>			
Speed	v_{max}	Maximum velocity	2.5–3.0
Goal	k_{goal}	Goal attraction gain	20.0–25.0
Barrier	k_{barrier}	Barrier repulsion gain	0.0
Time	Δt	Integration timestep	0.3
<i>Dungeon: environment</i>			
Map	$\text{SDF}(x, y)^{\text{PC}}$	Signed distance field (from grid)	—
Staging	s_{stage}	Stage window size	60 px
Waypoints	d_{wp}	Minimum waypoint wall clearance	1.5–4.0 px

with adaptive coefficients (β, γ, α) predicted by context encoders. It shares the same stage manager and local window as the reactive baselines but learns the local force field from short rollouts instead of fixing it a priori. All hyperring results (minimal sensing vs. navigation quality, planner comparisons, Hamiltonian field analysis, ablations, robustness) are reported against this set.

5.2.2 BASELINES FOR DUNGEON POINT-AGENT NAVIGATION

All dungeon methods share the same point-agent dynamics and action space, so differences reflect the planning/learning rule and map access (Fig. 11).

Classical baselines.

- **Grid A^{*} (full map):** 8-connected A^{*} on the true occupancy grid; used as the path-length reference L_{ref} .

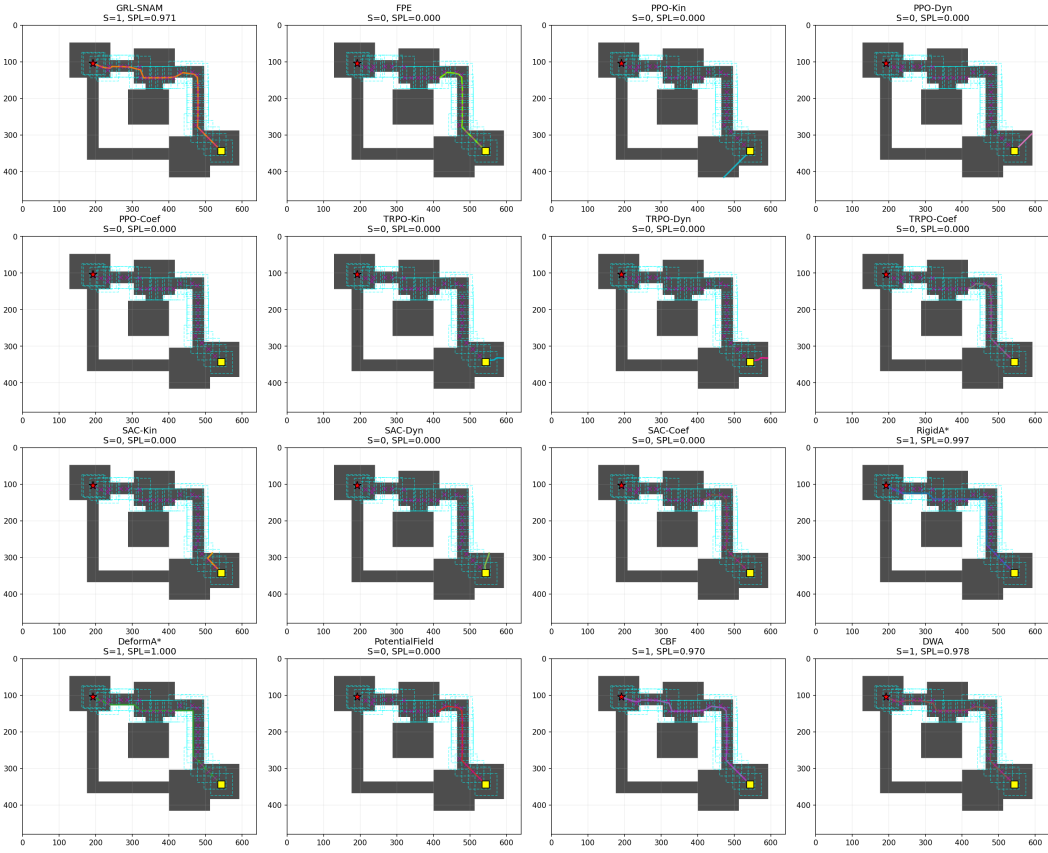


Figure 11: Representative dungeon rollouts under stagewise local sensing. Each panel shows the same layout with the goal (red \times), start (yellow square), executed trajectory (colored by time), and the union of visited sensing windows $\mathcal{W}(q_t)$ (cyan boxes). Panel titles report episode success S and SPL (with Grid A* as the reference path length L_{ref}). GRL-SNAM reaches the goal with near-planner efficiency, whereas stagewise deep-RL baselines (PPO/TRPO/SAC with Kin/Dyn/Coeff parameterizations) and the greedy potential-field baseline fail on this instance; classical planners and safety-filtered local methods (CBF/DWA) succeed but follow more conservative routes.

- **Greedy PF (local):** moves toward the goal with repulsion from walls in the local occupancy patch.
- **Local DWA (local):** samples velocity commands (v_x, v_y) , rolls out short trajectories against locally sensed walls, and scores by goal alignment, clearance, and length.

Deep RL baselines. We train PPO (Schulman et al., 2017), TRPO (Schulman et al., 2015), and SAC (Haarnoja et al., 2018) with the same encoder and observation encoding under two regimes:

- **Full-episode RL (long horizon):** standard end-to-end episodes with a global goal and a fixed step budget (e.g., 2000), without stage supervision.
- **Stagewise RL (short rollouts):** the same stagewise observation/action interface as GRL-SNAM: stage-relative state, stage-exit goal, and local extracted obstacles; episodes are extended to $K_{\text{ext}} = 8K$ to support exploration.

Within-framework variants (same data, different learning rule). Holding the stagewise interface and short-rollout dataset fixed, we replace Hamiltonian-structured supervision with:

- **Velocity regression:** supervised prediction of a_t from observations.

- **Coefficient RL:** policy-gradient learning over Hamiltonian coefficients (α, β, γ) instead of the DfPO-style objective.

5.3 METRICS AND EVALUATION PROTOCOL

Across both tasks we evaluate methods along four axes: (i) task success and path efficiency, (ii) safety and physical plausibility, (iii) mapping / sensing budget, and (iv) learning efficiency and robustness. Unless stated otherwise, we report averages over multiple random seeds and environment instances.

Navigation performance. We report: (i) **success rate** (fraction of episodes reaching the goal without hard collisions), (ii) **Success-weighted Path Length (SPL)**, measuring path efficiency relative to a reference planner (Rigid A* for hyperring, Grid A* for dungeon), and (iii) **detour ratio** L/L_{ref} over successful runs, indicating excess path length relative to the reference. We also track **smoothness** via average heading change per step to assess physical plausibility.

Safety and clearance. Safety is quantified by the **minimum** and **mean clearance** to the nearest obstacle along a trajectory (positive values indicate safety margins, negative values indicate penetrations), the number of **hard collisions** per episode, and, for methods with explicit barriers (CBF, GRL-SNAM, Deformable A*), the fraction of timesteps that violate a prescribed safety threshold (barrier violations).

Mapping and sensing budget. To measure how much of the environment each method must observe, we define the **mapping ratio** as the fraction of workspace area that ever falls inside a local sensing window during an episode. All stagewise methods (PF, CBF, DWA, GRL-SNAM, dungeon local baselines) use the same window size $2\hat{d} \times 2\hat{d}$; global planners (Rigid A*, Grid A*) have mapping ratio 100%.

Learning efficiency. For learning-based methods (GRL-SNAM, deep RL, within-framework variants) we track **sample efficiency** via success and SPL as functions of training interaction steps, summarize performance with area under the learning curve, and report the steps required to reach target thresholds (e.g., 80% success or $\text{SPL} \geq 0.7$). For GRL-SNAM, “steps” are short-rollout samples used in supervised Hamiltonian training; for PPO/TRPO/SAC they are environment transitions. We also report total environment steps, gradient updates, and update-to-sample ratios where relevant.

Evaluation protocols. For hyperelastic ring experiments, each environment is evaluated from multiple random start–goal pairs (typically 50), and we report aggregated statistics on Test-ID and Test-OOD splits. Unless noted, navigation-quality tables (e.g., Table 2) are computed on *successful runs only* to isolate path quality from outright failure. For dungeon experiments, full-episode baselines are trained and evaluated on long-horizon episodes with fixed step budgets, while short-rollout baselines and GRL-SNAM are trained on a stagewise dataset with horizon $H \in [2, 6]$ and evaluated on a held-out set of stagewise test samples with identical observation and action spaces. Robustness experiments vary sensing and dynamics fidelity over a grid of perturbation levels (e.g., position jitter, radius errors, missed/false obstacles, damping perturbations) and report success, SPL, clearance, and collisions; ablations vary only the training objective while keeping environments fixed, reporting the same core metrics plus qualitative behavior summaries.

5.4 RESULTS AT A GLANCE

Across the hyperelastic ring and dungeon point-agent tasks, results support four takeaways:

1. **Effective Path Planning under minimal sensing** On the hyperelastic ring, GRL-SNAM attains CBF-level efficiency while observing only sparse stagewise windows: Table 2 shows $\text{SPL} \approx 0.95$ and $\text{detour} \approx 1.09$ at a mapping ratio of $\sim 10\text{--}11\%$, comparable to PF’s sensing budget but with substantially higher path efficiency.
2. **Stronger navigation than conventional, reactive, and deep RL baselines.** On ring Test-ID/OOD, GRL-SNAM achieves near-perfect success with high SPL, smooth trajectories,

and positive clearance, while A^* planners, PF/CBF/DWA, and RL baselines trade off safety vs. efficiency or fail in clutter (Fig. 12, Fig. 13). In the dungeon benchmark, GRL-SNAM substantially outperforms PPO/TRPO/SAC trained end-to-end over millions of steps, and also outperforms their stagewise short-rollout versions under the same observation/action interface (Table 3, Table 4).

3. **The gain comes from the adaptive reward and geometric Hamiltonian learning.** Under matched stagewise sensing and short-rollout data, PPO/TRPO/SAC plateau below 30% success, whereas GRL-SNAM reaches $\sim 90\%$ success with $\sim 500k$ supervised updates on the same interface (Table 4), indicating the advantage is driven by Hamiltonian-structured supervision rather than algorithm choice.
4. **Interpretable fields, learned constraints, and robust adaptation.** GRL-SNAM learns a coherent force field that balances goal attraction and barrier repulsion via adaptive coefficients (β, γ, α) (Fig. 14, Fig. 15) and recovers barrier-like energy profiles from interaction (Fig. 16). Ablations isolate the role of dissipation and near-contact training (Table 5), and robustness tests show graceful degradation under sensing/dynamics noise (Table 6). Replay analysis indicates the system stores compact local transitions and constraint summaries rather than full maps (Fig. 17).

We next quantify sensing–performance trade-offs, then present the main ring and dungeon comparisons, followed by field analyses, ablations, and robustness.

5.5 NAVIGATION QUALITY VS. MAPPING EFFORT UNDER MINIMAL SENSING

We test whether GRL-SNAM can achieve near-planner navigation while sensing only a small fraction of the workspace. The dataset contains all the noise levels mentioned in Table 6. All *stagewise* methods share the same stage manager and local sensing window of size $2\hat{d} \times 2\hat{d}$; they differ only in how local observations are converted into forces/actions. We compare (i) classical local controllers (PF, CBF), (ii) GRL-SNAM, and (iii) deep RL trained under the *same* stagewise sensing and short-rollout distribution as GRL-SNAM.

RL under matched interfaces. For PPO, TRPO, and SAC we evaluate three control parameterizations: **Kin** (output velocities), **Dyn** (output forces integrated by a damped point-mass model), and **Coef** (output Hamiltonian coefficients (α, β, γ)). Thus, RL baselines share observations, local dynamics, and Hamiltonian building blocks with GRL-SNAM; only the learning rule and control parameterization change.

Metrics. On *successful runs* we report SPL, detour L/L_{ref} (Rigid A^* reference), minimum clearance (negative indicates penetration), and mapping ratio (fraction of workspace covered by any sensing window).

Near-planner quality at minimal mapping. Table 2 shows that GRL-SNAM matches CBF-level efficiency (SPL 0.95 vs. 0.96; detour 1.09 vs. 1.04) while requiring essentially the same mapping ratio as PF (10.7% vs. 10.3%). PF, despite identical sensing, yields substantially longer paths (detour 1.42) and lower SPL (0.77), indicating that the improvement comes from how sensed patches are converted into a local navigation field, not from sensing more of the map.

RL does not close the gap under matched sensing. Deep RL variants consume *more* mapping (typically 14–18%) yet remain far behind GRL-SNAM. We observe three recurring behaviors: (i) **Kin** policies often graze or collide (negative MinClear) and achieve low SPL; (ii) **Dyn** policies frequently stall or fail to complete (near-zero SPL, large detours); and (iii) **Coef** policies are strongest (TRPO/SAC-Coef), but still require higher mapping and operate at near-grazing clearances ($\approx 0.004\text{m}$) with only moderate SPL (0.57). Changing optimizer (PPO/TRPO/SAC) or parameterization (Kin/Dyn/Coef) shifts outcomes but does not reproduce the efficiency–safety trade-off achieved by GRL-SNAM.

Takeaway. Under identical stagewise sensing, GRL-SNAM is the only method that simultaneously attains high path efficiency (near CBF), low mapping (near PF), and strictly positive clearance,

Table 2: Navigation quality vs. mapping effort on the hyperelastic ring task (success-only runs). All stagewise methods use the same sensing window and stage manager. RL variants share the same stagewise sensing and short-rollout distribution as GRL-SNAM, differing only in control parameterization (Kin/Dyn/Coef) and learning rule.

Method	SPL \uparrow	Detour \downarrow	MinClear (m) \uparrow	Mapping (%) \downarrow
PF	0.77	1.42	0.18	10.3
CBF	0.96	1.04	0.32	11.2
GRL-SNAM	0.95	1.09	0.26	10.7
PPO-Kin	0.143	1.87	-0.358	15.4
PPO-Dyn	0.000	2.31	0.771	18.1
PPO-Coef	0.071	1.65	-0.092	14.7
TRPO-Kin	0.000	2.12	-0.327	16.5
TRPO-Dyn	0.000	1.98	0.019	15.9
TRPO-Coef	0.571	1.44	0.004	15.3
SAC-Kin	0.000	2.27	-0.229	16.8
SAC-Dyn	0.000	2.41	-0.229	16.9
SAC-Coef	0.571	1.53	0.004	14.6

suggesting the main advantage is the Hamiltonian-structured supervision that learns a constraint-aware local energy landscape rather than a direct reward-maximizing policy.

5.6 COMPREHENSIVE NAVIGATION COMPARISON

We compare GRL-SNAM to (i) full-map global planners (Rigid A*, Deformable A*), (ii) stagewise local controllers (PF, CBF, DWA) with the same sensing window and stage manager, and (iii) deep RL policies trained under the same stagewise, short-rollout interface as GRL-SNAM (Kin/Dyn/Coef). We evaluate on Test-ID and Test-OOD using success, SPL, detour L/L_{ref} , minimum clearance, and smoothness. Figure 13 reports aggregate metrics and Figure 12 shows representative rollouts.

Performance across ID and OOD. GRL-SNAM maintains near-perfect success on both Test-ID and Test-OOD and achieves the highest SPL with low variance. By contrast, full-map planners are either conservative (inflation-induced detours) or sensitive to hand-tuned deformation costs, and stagewise reactive methods (PF/CBF/DWA) degrade on Test-OOD due to local oscillations, stalls, or cul-de-sac behavior.

Aggregate trade-offs (readout of Fig. 13). Fig. 13 is organized as two dashboards: Test-ID (left) and Test-OOD (right). Within each dashboard, the *top row* reports task-level performance and efficiency: (*left*) success rate (fraction of episodes reaching the goal), (*middle*) the distribution of SPL (zeros indicate failures; values near one indicate near-shortest successful paths), and (*right*) average path length, which disambiguates whether high SPL comes from genuinely short paths versus a small number of efficient successes. The *bottom row* reports safety and cost: (*left*) the distribution of per-episode minimum clearance $\text{clr}_{\min} = \min_n \text{clr}_n$ (lower tails indicate grazing/collisions), (*middle*) the “grazing rate” $\mathbb{P}(\text{clr}_{\min} \leq d_{\text{thr}})$ for a fixed threshold d_{thr} (here 1.5), and (*right*) average computation time per episode.

Across both Test-ID and Test-OOD, GRL-SNAM couples *high success* with an SPL distribution concentrated near high values, while maintaining strictly positive clearance (small lower tail and low grazing rate). In contrast, kinematic/dynamic RL baselines show a larger mass at low SPL (more failures and inefficient successes) and heavier low-clearance tails, while conservative/global planners and potential-field variants tend to keep large clearance but pay for it with reduced efficiency (lower SPL / longer paths) and, in some settings, additional failures from overly conservative detours or local minima.

Qualitative behavior. Fig. 12 shows a representative *Test-OOD bottleneck* layout (start: \star , goal: \square ; circles: obstacles). Each panel title reports *Success* and *SPL*. **Row 1 (GRL-SNAM and PPO variants):** GRL-SNAM (top-left) executes a single, smooth *squeeze-and-recover* maneuver: it threads the narrow gap between the upper obstacle cluster and the large central obstacle, then re-centers and reaches the goal with minimal detour (Success = 1, SPL = 1). In contrast, PPO-Kin and PPO-Dyn (top row, middle) fail in this bottleneck: the kinematic variant stalls short of the goal, while the dynamic variant drifts into an unproductive detour and times out (Success = 0). PPO-Coef (top-right) illustrates that even when coefficients are learnable, the rollout can still fail on this OOD geometry (Success = 0), reflecting sensitivity to tight clearances.

Row 2 (TRPO variants and SAC-Kin): TRPO-Kin and TRPO-Dyn (second row, left/middle) again fail to traverse the bottleneck (Success = 0), typically stopping early or clipping the corridor geometry. TRPO-Coef (second row, third) succeeds (Success = 1) but the path *hugs obstacle boundaries* through the constriction, indicating smaller clearance margins than GRL-SNAM. SAC-Kin (second row, right) also fails on this instance (Success = 0).

Row 3 (SAC variants and global planners): SAC-Dyn (third row, left) fails (Success = 0) and exhibits a large, boxy detour pattern that does not resolve the bottleneck. SAC-Coef (third row, second) succeeds (Success = 1) but, similar to TRPO-Coef, succeeds by skimming close to obstacles in the narrow passage. The global planners RigidA* and DeformA* (third row, right two panels) both succeed (Success = 1) but produce *piecewise-linear and/or conservative* routes with multiple right-angle turns and larger stand-off distances, yielding longer paths that avoid exploiting the short near-boundary squeeze.

Row 4 (classical local controllers): Potential Field (bottom-left) fails (Success = 0), consistent with a local-minimum/trapping failure mode near the bottleneck. By contrast, CBF and DWA (bottom-middle/right) both succeed (Success = 1), but their rollouts show characteristic *reactive behavior*: visible curvature/adjustments around obstacles and a less direct route than GRL-SNAM, reflecting oscillations or conservative arcs induced by local constraint satisfaction.

Global planners succeed but generate jagged or overly conservative paths that does not exploit near boundary squeezing path which can be shorter.

5.7 LEARNING STRATEGIES IN DUNGEON NAVIGATION: DEEP RL VS. HAMILTONIAN SUPERVISION

The dungeon point-agent task isolates the *learning signal* under matched dynamics and observations: all methods share the same 2D continuous control, local occupancy encoding, and Transformer encoder; only the training objective differs. We report (i) end-to-end, full-episode RL on the long-horizon MDP, and (ii) stagewise short-rollout training with the same observation/action interface used by GRL-SNAM.

Full-episode deep RL (long-horizon). We train PPO, TRPO, and SAC to reach a global goal within a 2000-step budget using only local observations. Despite 5–8M environment transitions, success remains below 8% and collision rates are \sim 25%, highlighting the difficulty of long-horizon credit assignment under partial observability.

Table 3: Full-episode, end-to-end navigation baselines (PPO/TRPO/SAC) in the dungeon environment. Despite substantial training budgets (5–8M environment steps), all three RL methods fail to learn reliable goal-directed navigation under the dungeon’s partial/local observations: success remains extremely low (1.5–7.2%), collisions are frequent (23.5–28.3%), and the agent typically terminates far from the goal (mean residual distance 14–24 m). See Fig. 11 for qualitative evidence.

Algorithm	Success (%)	Mean goal dist. (m)	Collision (%)	Env. training steps
PPO	7.2	14.1	23.5	5M
TRPO	3.8	23.7	26.1	6.5M
SAC	1.5	20.2	28.3	8M

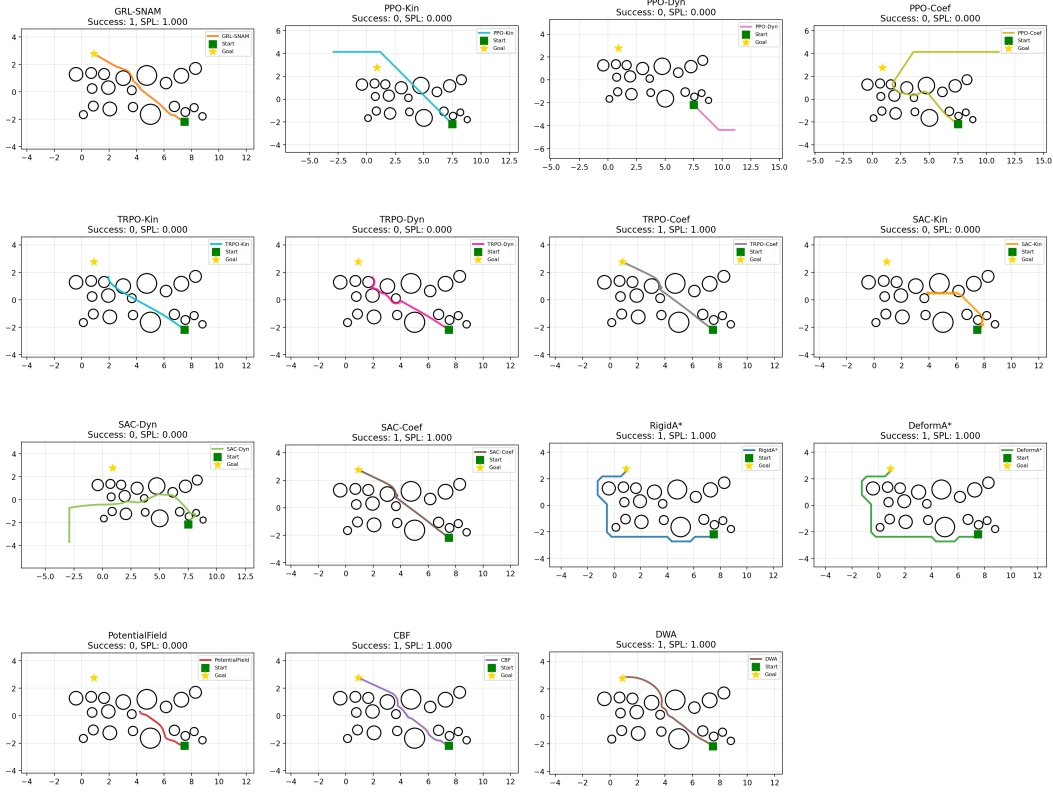


Figure 12: **Qualitative rollouts on a representative Test-OOD bottleneck layout.** Start is marked by \star , goal by \square , and circles denote obstacles; each panel title reports Success and SPL. **Row 1:** GRL-SNAM and PPO (Kin/Dyn/Coef). **Row 2:** TRPO (Kin/Dyn/Coef) and SAC-Kin. **Row 3:** SAC (Dyn/Coef) and global planners (RigidA*, DeformA*). **Row 4:** classical local methods (Potential Field, CBF, DWA). GRL-SNAM is the only method here that achieves a smooth, short *squeeze-and-recover* trajectory through the bottleneck without grazing, while learning-based baselines either fail (Kin/Dyn) or succeed by boundary-hugging (Coef). Global planners succeed but are jagged/overly conservative, and local controllers highlight reactive artifacts (trapping for PF; oscillatory/arc-like adjustments for CBF/DWA).

Stagewise short-rollout RL (matched interface). To remove interface confounds, we train the same RL algorithms on the *same* stagewise short-rollout distribution and structured observations as GRL-SNAM: stage-relative state, stage-exit goal, and locally extracted obstacles, with actions $\mathbf{a}_t = [v_x, v_y]$. RL improves over the full-episode setting, but still plateaus well below GRL-SNAM.

Table 4: Short-rollout, stagewise baselines vs. GRL-SNAM on the same dungeon-derived dataset and the same sensors. While PPO/TRPO/SAC improve over full-episode training, they remain limited in reliability (18.4–26.1% success) and exhibit noticeably larger tracking error and residual goal distance. In contrast, GRL-SNAM achieves 87.5% success with substantially lower state error and goal distance, indicating that the learned GRL-SNAM surrogate produces actions that are both locally safe and globally progress-seeking. This advantage is displayed with the qualitative comparison in Fig. 11.

Algorithm	Success (%)	Mean state error (m) \downarrow	Mean goal dist. (m) \downarrow	Env. training steps
PPO	26.1	1.8	1.2	≈ 3.2 M env. steps
TRPO	21.7	2.1	1.5	≈ 3.8 M env. steps
SAC	18.4	2.4	1.9	≈ 4.1 M env. steps
GRL-SNAM	87.5	0.3	0.1	500k gradient steps

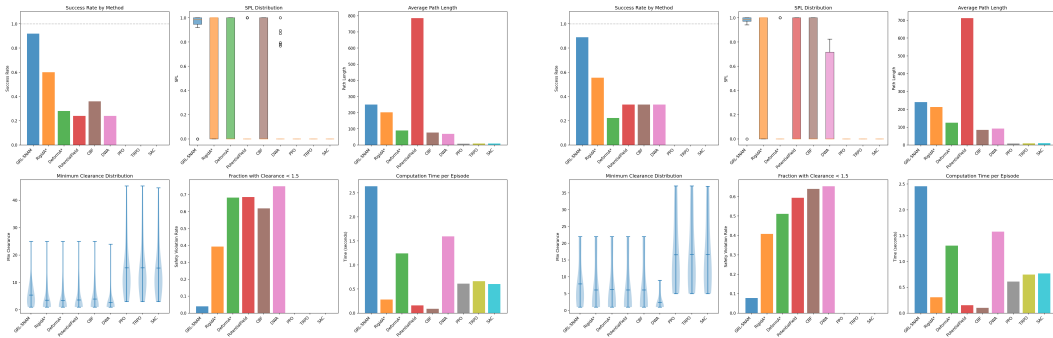


Figure 13: **Test-ID (left) and Test-OOD (right) dashboard (aggregate over all trials).** Each side contains six panels. *Top row (performance/efficiency):* (1) success rate; (2) SPL distribution (zeros correspond to failures; higher is better among successes); (3) average path length. *Bottom row (safety/cost):* (4) distribution of per-episode minimum clearance $\text{clr}_{\min} = \min_n \text{clr}_n$; (5) grazing rate $\mathbb{P}(\text{clr}_{\min} \leq d_{\text{thr}})$ with $d_{\text{thr}}=1.5$; (6) average computation time per episode. GRL-SNAM achieves a strong joint trade-off across splits: high success with high SPL and short paths, while preserving positive clearance (low grazing rate) at moderate compute.

Takeaway: objective dominates optimizer. With dynamics, sensing, and encoder fixed, swapping PPO/TRPO/SAC changes results modestly but does not close the gap. The consistent improvement comes from *Hamiltonian-structured supervision*: GRL-SNAM learns an energy model whose gradients encode goal attraction, barrier avoidance, and dissipation, rather than optimizing a sparse scalar reward. This yields substantially higher success and lower terminal error in the same observation/action regime, indicating that the advantage is primarily due to the learning formulation rather than the choice of RL optimizer.

5.8 HAMILTONIAN FIELD AND CONSTRAINT LEARNING

We analyze the learned force fields, barrier structure, and replay contents on the hyperelastic ring under stagewise sensing.

Force-field decomposition. Figure 14 visualizes the learned force field (negative differential of sub-modular potentials) as goal attraction F_g , obstacle barriers F_{bs} , and their composition

$$F = \beta F_g + \gamma F_{bs}. \quad (30)$$

F_g alone is task-directed but obstacle-agnostic, while F_{bs} encodes avoidance without a navigation objective. Their composition produces smooth, clearance-preserving arcs around clutter via adaptive reweighting through (β, γ) .

Online coefficient adaptation. Along a representative rollout (Fig. 15), clearance decreases near bottlenecks and recovers after passage (top). The magnitudes $|F_g|$ and $|F_{bs}|$ rebalance accordingly (middle), while coefficients (β, γ, α) vary smoothly over time (bottom), indicating adaptation occurs through the Hamiltonian parametrization rather than ad hoc action scaling.

Empirical barrier learning. Figure 16 compares the learned obstacle barrier energy to the simulator’s analytic reference using an angle-averaged radial profile. The learned barrier is near-zero at large clearance and rises sharply near contact, closely tracking the reference while slightly softening at intermediate distances and steepening near contact, consistent with additional deformation/friction costs captured in the rollout data.

Stagewise reuse and bootstrapped refinement. Stagewise parameterization induces a family of local policies (sensor/frame/shape controllers) that share parameters but adapt (β, γ, α) by stage. As new windows are visited, local rollouts refine the Hamiltonian for those regions; revisits exploit this refinement without recomputing global plans. Empirically, trajectories tighten toward least-cost paths over time while maintaining positive clearance.

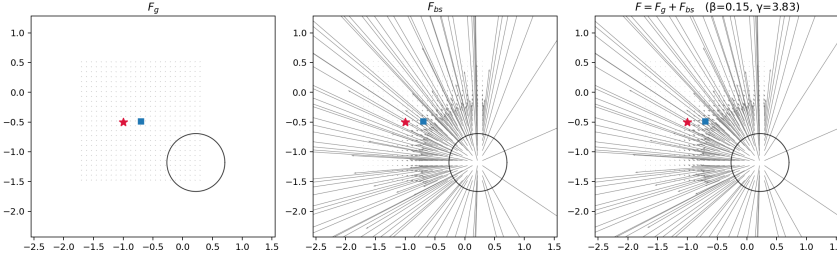


Figure 14: **Learned Hamiltonian field decomposition.** Shown are the constituent fields used by GRL-SNAM to generate local motion under partial, stagewise observations. **Left:** F_g points toward the current stage goal and captures progress, but ignores obstacles. **Middle:** F_{bs} is induced by locally sensed barriers and encodes avoidance/clearance, but lacks task direction. **Right:** the deployed field $F = \beta F_g + \gamma F_{bs}$ combines both effects; the learned, context-dependent coefficients (β, γ) modulate the relative strength of goal following vs. obstacle avoidance, producing a trajectory direction that threads the corridor while maintaining a safety margin near contact regions.

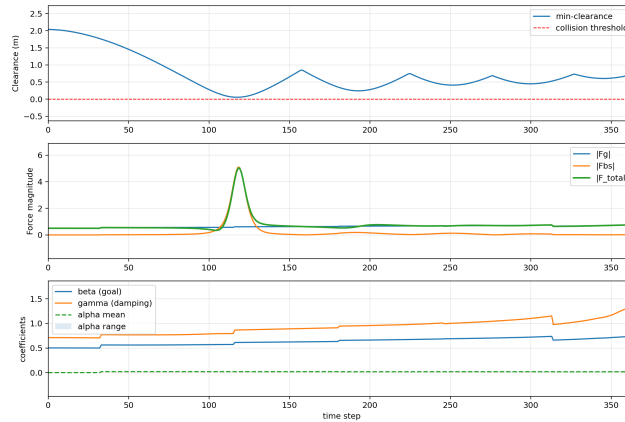


Figure 15: **Temporal analysis of Hamiltonian adaptation.** Top: minimum clearance. Middle: $|F_g|$ and $|F_{bs}|$. Bottom: coefficients (β, γ, α). Coefficients change smoothly as the robot enters/leaves clutter, rebalancing goal and barrier terms.

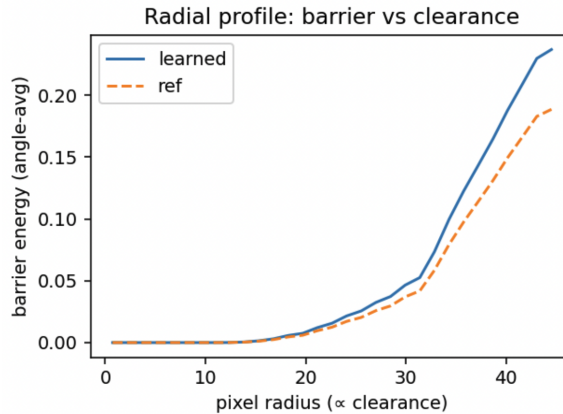


Figure 16: **Radial profile of barrier energy vs. clearance.** Angle-averaged barrier energy around obstacles for the learned barrier (solid) and analytic reference (dashed). The learned profile matches the reference trend and sharpens near contact. The difference between two curves indicates Our method can learn to adapt the energy landscape based on its current environment context.

Replay buffer thriftiness. Figure 17 shows buffer memory is dominated by local transitions (q_t, q_{t+1}) (about 80%), with compact constraint/contact summaries (about 15%); actions, gradients, barrier scales, and rewards occupy only a few percent. The buffer therefore stores only what is needed for Hamiltonian updates—local dynamics and local constraints—without caching full maps or dense cost volumes.

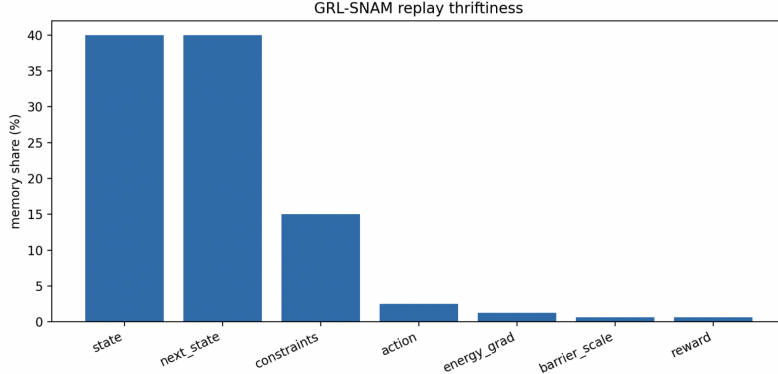


Figure 17: **Replay thriftiness in GRL-SNAM.** Memory share of buffer fields: $\sim 80\%$ local transitions (q_t, q_{t+1}), $\sim 15\%$ compact constraint/contact sets, and only a few percent for actions, gradients, barrier scales, or rewards. GRL-SNAM is memory efficient as it only maintains the local state exhaustively while using a low dimensional network structure which effectively encodes the energy landscape.

Closed-loop Hamiltonian refinement. Stagewise interaction supplies short rollouts that populate the buffer (Fig. 17); buffer updates adjust coefficients and barrier parameters, reshaping the local landscape (Figs. 14–16); the updated landscape then induces the next round of dynamics. This yields a closed-loop procedure that repeatedly refines \mathcal{H}_θ from local experience.

5.9 ABLATIONS AND ROBUSTNESS

We finally probe how specific design choices in GRL-SNAM affect performance, and how well the learned Hamiltonian controller tolerates sensing and dynamics perturbations.

Effect of loss components. Recall that our navigation surrogate is trained with a weighted multi-term loss

$$\mathcal{L} = w_{\text{traj}} \mathcal{L}_{\text{traj}} + w_{\text{vel}} \mathcal{L}_{\text{vel}} + w_{\text{friction}} \mathcal{L}_{\text{friction}} + w_{\text{multi}} \mathcal{L}_{\text{multi}}, \quad (31)$$

where $\mathcal{L}_{\text{traj}}$ and \mathcal{L}_{vel} supervise trajectory and velocity matching, $\mathcal{L}_{\text{friction}} = \|\gamma - \gamma_o\|_2^2$ aligns the learned damping with the stagewise reference, and $\mathcal{L}_{\text{multi}}$ trains near-contact robustness via perturbed short rollouts. We ablate the last two terms while keeping environments and architectures fixed.

Table 5: **Ablation of loss terms** on the hyperelastic ring benchmark (Test-ID/OOD). Arrows denote desired direction. Icons summarize consistent qualitative trends across several seeds.

Variant	Collisions \downarrow	MinClr \uparrow	Barrier Viol. \downarrow	Progress/SPL \uparrow	Smoothness \downarrow	Observed behavior
$w_{\text{fric}} = 0, w_{\text{multi}} = 0$	High (✗)	< 0	High	Poor	Poor	Penetrates obstacles
$w_{\text{fric}} = 0, w_{\text{multi}} = 0.5$	Low (✓)	High	Low	Low	OK	Very slow, conservative
$w_{\text{fric}} = 0.1, w_{\text{multi}} = 0$	None (✓)	High	Low	High	Best	Smooth, stable, fast
$w_{\text{fric}} = 0.1, w_{\text{multi}} = 0.5$	None (✓)	Slightly lower	Low	High	Good	Stable; tighter margins

Table 5 shows that: (i) without $\mathcal{L}_{\text{friction}}$ or $\mathcal{L}_{\text{multi}}$, the learned field is under-damped and oscillatory, leading to barrier violations and penetrations; (ii) $\mathcal{L}_{\text{multi}}$ alone enforces safety but at the cost of extremely slow motion, as the learner over-weights near-contact failures and suppresses progress; (iii) $\mathcal{L}_{\text{friction}}$ alone is sufficient to eliminate penetrations and produce smooth, fast trajectories; and (iv) combining both terms yields the best overall trade-off, with slightly tighter clearances but robust, stable motion in clutter. These trends are consistent with the Hamiltonian interpretation: $\mathcal{L}_{\text{friction}}$ learns

an appropriate dissipation term, preventing “ringing” of the barrier energy, while $\mathcal{L}_{\text{multi}}$ selectively shapes the field near constraints.

Robustness to sensing and dynamics perturbations. We next evaluate GRL-SNAM under controlled perturbations to sensing and dynamics. We vary position jitter and radius estimation error in the local obstacle extractor, randomly drop or hallucinate obstacles, and perturb the damping coefficient γ and applied velocities. Each start–goal pair is rolled out across a grid of perturbation levels, yielding a total of $N = n_{\text{env}} \times n_{\text{trials}} \times n_{\text{perturbations}}$ runs.

Table 6: Robustness of GRL-SNAM to sensing noise and dynamics perturbations. Perturbation settings are reported as (sensing noise, damping scale). Even when noise level in sensor and motion is very high (Severe Noise), our method is still robust and achieve 87% overall success rate, which is better comparing against RL methods.

Perturbation Level	Success (%)	SPL \uparrow	Min. Clearance (m) \uparrow	Collisions \downarrow
Nominal (0.0, 1.0)	98.7	0.82	0.36	0.3
Mild Noise (0.05, 0.9)	91.3	0.79	0.33	0.7
Severe Noise (0.10, 0.7)	87.1	0.72	0.29	1.1

As shown in Table 6, GRL-SNAM maintains high success rates ($\geq 87\%$) and positive clearance even under severe noise and dynamics mismatch. SPL and clearance degrade gracefully as perturbations increase, while collision counts remain low. Rather than failing catastrophically when constraints or dynamics are mis-specified, the learned Hamiltonian field re-weights goal and barrier terms in response to distorted local observations (cf. Figure 15), preserving a meaningful safety–progress trade-off.

Takeaways. The performance of (i) the friction and multi-start losses play distinct, interpretable roles in learning dissipation and near-contact robustness in the Hamiltonian surrogate; (ii) performance is not brittle to moderate changes in sensing or dynamics, because GRL-SNAM adapts by reshaping the energy landscape rather than overfitting to a single nominal model; and (iii) these properties are emergent from the same empirical Hamiltonian-modification pipeline analyzed in Section 5.8, reinforcing our claim that GRL-SNAM provides a stable, constraint-aware alternative to standard reward-based policies for stagewise navigation.

6 CONCLUSION

We introduce GRL-SNAM, a geometric reinforcement learning framework that leverages Hamiltonian structure to couple sensing, planning, and deformation into a unified energy-based policy. Our formulation enables stable, feedforward navigation updates and achieves near-optimal path quality with minimal mapping effort in challenging deformable-robot tasks. The results highlight that incorporating geometric priors into RL can yield both efficiency and robustness, even under noisy sensing and out-of-distribution layouts. Future work will extend the approach to richer sensing modalities and more complex environments, with the goal of validating its scalability to real robotic systems.

ACKNOWLEDGEMENT

This research was supported in part from the Peter O’Donnell Foundation, the Jim Holland- Backcountry Foundation and in part from a grant from the Army Research Office accomplished under Cooperative Agreement Number W911NF-19-2-0333.

REFERENCES

David H Ackley, Geoffrey E Hinton, and Terrence J Sejnowski. A learning algorithm for boltzmann machines. *Cognitive science*, 9(1):147–169, 1985.

J. I. Alora, Moses C. Beard, Thomas Libby, Philipp Rothemund, et al. Discovering dominant dynamics for nonlinear continuum robot control. *npj Robotics*, 3(1):5, 2025.

Anthony Brohan, Noah Brown, Justice Carbajal, Yevgen Chebotar, Joseph Dabis, Chelsea Finn, Keerthana Gopalakrishnan, Karol Hausman, Alex Herzog, Jasmine Hsu, Julian Ibarz, Brian Ichter, Alex Irpan, Tomas Jackson, Sally Jesmonth, Nikhil J Joshi, Ryan Julian, Dmitry Kalashnikov, Yuheng Kuang, Isabel Leal, Kuang-Huei Lee, Sergey Levine, Yao Lu, Utsav Malla, Deeksha Manjunath, Igor Mordatch, Ofir Nachum, Carolina Parada, Jodilyn Peralta, Emily Perez, Karl Pertsch, Jornell Quiambao, Kanishka Rao, Michael Ryoo, Grecia Salazar, Pannag Sanketi, Kevin Sayed, Jaspia Singh, Sumedh Sontakke, Austin Stone, Clayton Tan, Huong Tran, Vincent Vanhoucke, Steve Vega, Quan Vuong, Fei Xia, Ted Xiao, Peng Xu, Sichun Xu, Tianhe Yu, and Brianna Zitkovich. Rt-1: Robotics transformer for real-world control at scale, 2023. URL <https://arxiv.org/abs/2212.06817>.

Brandon Caasenbrood, Alexander Pogromsky, and Henk Nijmeijer. Control-oriented models for hyperelastic soft robots through differential geometry of curves. *Soft Robotics*, 9(2):346–361, 2022.

Devendra Singh Chaplot, Ruslan Salakhutdinov, Abhinav Gupta, and Saurabh Gupta. Neural topological slam for visual navigation. In *Proceedings of the IEEE/CVF Conference on Computer Vision and Pattern Recognition*, pp. 12875–12884, 2020.

Mohammad Dehghani Tezerjani et al. A survey on reinforcement learning applications in slam. *arXiv preprint arXiv:2408.14518*, 2024.

Shaan A Desai, Marios Mattheakis, David A Roberts, and Pavlos Protopapas. Port-hamiltonian neural networks for learning explicit time-dependent dynamical systems. *Physical Review E*, 104(3):034312, 2021.

Zhan Feng et al. Safer gap: A gap-based local planner for safe navigation with nonholonomic mobile robots. *arXiv preprint arXiv:2303.08243*, 2023.

M.M.A. Ferreira and R.B. Vinter. When is the maximum principle for state constrained problems nondegenerate? *Journal of Mathematical Analysis and Applications*, 187(2):438–467, 1994. ISSN 0022-247X. doi: <https://doi.org/10.1006/jmaa.1994.1366>. URL <https://www.sciencedirect.com/science/article/pii/S0022247X84713667>.

Dieter Fox, Wolfram Burgard, and Sebastian Thrun. The dynamic window approach to collision avoidance. *IEEE robotics & automation magazine*, 4(1):23–33, 2002.

Scott Fujimoto, Herke Hoof, and David Meger. Addressing function approximation error in actor-critic methods. In *International conference on machine learning*, pp. 1587–1596, 2018.

Saurabh Gupta, Varun Tolani, James Davidson, Sergey Levine, Rahul Sukthankar, and Jitendra Malik. Cognitive mapping and planning for visual navigation, 2019. URL <https://arxiv.org/abs/1702.03920>.

Tuomas Haarnoja, Aurick Zhou, Pieter Abbeel, and Sergey Levine. Soft actor-critic: Off-policy maximum entropy deep reinforcement learning with a stochastic actor. In *International conference on machine learning*, pp. 1861–1870, 2018.

Richard F Hartl, Suresh P Sethi, and Raymond G Vickson. A survey of the maximum principles for optimal control problems with state constraints. *SIAM review*, 37(2):181–218, 1995.

Tai Hoang, Huy Le, Philipp Becker, Vien Anh Ngo, and Gerhard Neumann. Geometry-aware rl for manipulation of varying shapes and deformable objects. *arXiv preprint arXiv:2502.07005*, 2025.

John J Hopfield. Neural networks and physical systems with emergent collective computational abilities. *Proceedings of the national academy of sciences*, 79(8):2554–2558, 1982.

Junwoo Jang and Maani Ghaffari. Social zone as a barrier function for socially-compliant robot navigation, 2024. URL <https://arxiv.org/abs/2405.15101>.

Yanwei Jia and Xun Yu Zhou. q-learning in continuous time. *Journal of Machine Learning Research*, 24(161):1–61, 2023. URL <http://jmlr.org/papers/v24/22-0755.html>.

Eshagh Kargar and Ville Kyrki. Macrpo: Multi-agent cooperative recurrent policy optimization, 2021. URL <https://arxiv.org/abs/2109.00882>.

Nikhil Keetha, Jay Karhade, Krishna Murthy Jatavallabhula, Gengshan Yang, Sebastian Scherer, et al. Splatam: Splat, track & map 3d gaussians for dense rgb-d slam. In *Proceedings of the IEEE/CVF Conference on Computer Vision and Pattern Recognition*, 2024.

Junho Kim, Eun Sun Lee, Mingi Lee, Donsu Zhang, and Young Min Kim. Sgolam: Simultaneous goal localization and mapping for multi-object goal navigation, 2021. URL <https://arxiv.org/abs/2110.07171>.

Holger Klein, Noémie Jaquier, Andre Meixner, and Tamim Asfour. On the design of region-avoiding metrics for collision-safe motion generation on riemannian manifolds, 2023. URL <https://arxiv.org/abs/2307.15440>.

Matthew Lai, Keegan Go, Zhibin Li, Torsten Kröger, Stefan Schaal, Kelsey Allen, and Jonathan Scholz. Roboballet: Planning for multirobot reaching with graph neural networks and reinforcement learning. *Science Robotics*, 10(106):eads1204, 2025.

Yann LeCun, Sumit Chopra, Raia Hadsell, M Ranzato, Fujie Huang, et al. A tutorial on energy-based learning. *Predicting structured data*, 1(0), 2006.

Kyowoon Lee, Seongun Kim, and Jaesik Choi. Adaptive and explainable deployment of navigation skills via hierarchical deep reinforcement learning. In *International Conference on Robotics and Automation*, 2023.

Chengshu Li et al. Hrl4in: Hierarchical reinforcement learning for interactive navigation with mobile manipulators. In *Conference on Robot Learning*, 2020a.

Junjie Li et al. Learn with imagination: Safe set guided state-wise constrained policy optimization. *arXiv preprint arXiv:2308.13140*, 2023.

Minchen Li, Zachary Ferguson, Teseo Schneider, Timothy R Langlois, Denis Zorin, Daniele Panozzo, Chenfanfu Jiang, and Danny M Kaufman. Incremental potential contact: intersection- and inversion-free, large-deformation dynamics. *ACM Trans. Graph.*, 39(4):49, 2020b.

Jingsong Liang, Zhichen Wang, Yuhong Cao, Jimmy Chiun, Mengqi Zhang, and Guillaume Adrien Sartoretti. Context-aware deep reinforcement learning for autonomous robotic navigation in unknown area. In *Conference on Robot Learning*, pp. 1425–1436. PMLR, 2023.

Elisabetta Liu and Cosimo Della Santina. Physics-informed neural networks to model and control robots: a theoretical and experimental investigation. *Advanced Intelligent Systems*, 2024.

Paul Malisani. Interior point methods in optimal control problems of affine systems: Convergence results and solving algorithms. *SIAM Journal on Control and Optimization*, 61(6):3390–3414, 2023.

David Martínez-Rubio and Sebastian Pokutta. Accelerated riemannian optimization: Handling constraints with a prox to bound geometric penalties. In *The Thirty Sixth Annual Conference on Learning Theory*, pp. 359–393. PMLR, 2023.

Luke McLennan, Yi Wang, Ryan Farrell, Minh Nguyen, and Chandrajit Bajaj. Learning generalized hamiltonian dynamics with stability from noisy trajectory data, 2025. URL <https://arxiv.org/abs/2509.07280>.

Nicholas Mohammad and Nicola Bezzo. Soft actor-critic-based control barrier adaptation for robust autonomous navigation in unknown environments, 2025. URL <https://arxiv.org/abs/2503.08479>.

Barry W Mulvey and Thirishantha Nanayakkara. Haven: haptic and visual environment navigation by a shape-changing mobile robot with multimodal perception. *Scientific Reports*, 14(1):27018, 2024.

Minh Nguyen and Chandrajit Bajaj. A differential and pointwise control approach to reinforcement learning. 2025a. URL <https://arxiv.org/abs/2404.15617>.

Minh Phuong Nguyen and Chandrajit L. Bajaj. Stochastic differential policy optimization: A rough path approach to reinforcement learning. In *Workshop on the Theory of AI for Scientific Computing*, 2025b. URL <https://openreview.net/forum?id=W2TVe58Rp2>.

Jorge Nocedal and Stephen J. Wright. *Numerical Optimization*. Springer Series in Operations Research and Financial Engineering. Springer, New York, NY, 2 edition, 2006. ISBN 978-0-387-40065-5. doi: 10.1007/978-0-387-40065-5.

Adam Paszke, Sam Gross, Francisco Massa, Adam Lerer, James Bradbury, Gregory Chanan, Trevor Killeen, Zeming Lin, Natalia Gimelshein, Luca Antiga, et al. Pytorch: An imperative style, high-performance deep learning library. *Advances in neural information processing systems*, 32, 2019.

J Pearson and R Sridhar. A discrete optimal control problem. *IEEE Transactions on automatic control*, 11(2):171–174, 1966.

F. Qi, C. Zhou, H. Qing, H. Sun, and J. Yin. Aerial track-guided autonomous soft ring robot. *Advanced Science*, 2024.

Antonin Raffin, Ashley Hill, Adam Gleave, Anssi Kanervisto, Maximilian Ernestus, and Noah Dormann. Stable-baselines3: Reliable reinforcement learning implementations. *Journal of Machine Learning Research*, 22(268):1–8, 2021. URL <http://jmlr.org/papers/v22/20-1364.html>.

Mohammad Roshanfar, Javad Dargahi, and Amir Hooshiar. Hyperelastic modeling and validation of hybrid-actuated soft robot with pressure-stiffening. *Micromachines*, 14(5):1001, 2023.

Farell Ryan, Eric Bickel J., and Bajaj Chandrajit. Bayesian port-hamiltonian surrogate for three-phase reservoir flow simulation. volume Middle East Oil, Gas and Geosciences Show (MEOS GEO) of *SPE Middle East Oil and Gas Show and Conference*, pp. D021S043R002, 09 2025. doi: 10.2118/227802-MS. URL <https://doi.org/10.2118/227802-MS>.

Adarsh Jagan Sathyamoorthy, Kasun Weerakoon, Tianrui Guan, Jing Liang, and Dinesh Manocha. Terrapn: Unstructured terrain navigation using online self-supervised learning. In *2022 IEEE/RSJ International Conference on Intelligent Robots and Systems (IROS)*, pp. 7197–7204. IEEE, 2022.

John Schulman, Sergey Levine, Pieter Abbeel, Michael Jordan, and Philipp Moritz. Trust region policy optimization. In *International conference on machine learning*, pp. 1889–1897. PMLR, 2015.

John Schulman, Filip Wolski, Prafulla Dhariwal, Alec Radford, and Oleg Klimov. Proximal policy optimization algorithms. 2017.

Haruki Settai, Naoya Takeishi, and Takehisa Yairi. A temporal difference method for stochastic continuous dynamics. *arXiv preprint arXiv:2505.15544*, 2025.

Haoxiang Shi, Xiang Deng, Zaijing Li, Gongwei Chen, Yaowei Wang, and Liqiang Nie. Dagger diffusion navigation: Dagger boosted diffusion policy for vision-language navigation. *arXiv preprint arXiv:2508.09444*, 2025.

Edgar Sucar, Shikun Liu, Joseph Ortiz, and Andrew J Davison. imap: Implicit mapping and positioning in real-time. In *Proceedings of the IEEE/CVF International Conference on Computer Vision*, pp. 6229–6238, 2021.

Richard S Sutton, Doina Precup, and Satinder Singh. Between mdps and semi-mdps: Learning, planning, and representing knowledge at multiple temporal scales. Technical report, Technical Report 98-74, University of Massachusetts, Amherst, 1998.

Hamid Taheri et al. Deep reinforcement learning with enhanced ppo for safe mobile robot navigation. *arXiv preprint arXiv:2405.16266*, 2024.

Lei Tai, Giuseppe Paolo, and Ming Liu. Virtual-to-real deep reinforcement learning: Continuous control of mobile robots for mapless navigation. In *2017 IEEE/RSJ international conference on intelligent robots and systems (IROS)*, pp. 31–36. IEEE, 2017.

Lei Tai, Wolfram Burgard, Jingwei Zhang, Oleksii Zhelo, and Ming Liu. Curiosity-driven exploration for mapless navigation with deep reinforcement learning. May 2018a. IEEE International Conference on Robotics and Automation (ICRA 2018).

Lei Tai, Jingwei Zhang, Ming Liu, and Wolfram Burgard. Socially compliant navigation through raw depth inputs with generative adversarial imitation learning, 2018b. URL <https://arxiv.org/abs/1710.02543>.

Alexander Sasha Vezhnevets, Simon Osindero, Tom Schaul, Nicolas Heess, Max Jaderberg, David Silver, and Koray Kavukcuoglu. Feudal networks for hierarchical reinforcement learning. In *International conference on machine learning*, pp. 3540–3549. PMLR, 2017.

Niclas Vödisch, Daniele Cattaneo, Wolfram Burgard, and Abhinav Valada. *Continual SLAM: Beyond Lifelong Simultaneous Localization and Mapping Through Continual Learning*, pp. 19–35. Springer Nature Switzerland, 2023. ISBN 9783031255557. doi: 10.1007/978-3-031-25555-7_3. URL http://dx.doi.org/10.1007/978-3-031-25555-7_3.

Tianhao Wang et al. Pinn-ray: A physics-informed neural network to model soft robotic fin ray fingers. *arXiv preprint arXiv:2407.08222*, 2024.

Weizheng Wang et al. Multi-agent llm actor-critic framework for social robot navigation. *arXiv preprint arXiv:2503.09758*, 2025.

Chi Yan, Delin Qu, Dan Wang, Dan Xu, Zhigang Wang, et al. Gs-slam: Dense visual slam with 3d gaussian splatting. In *Proceedings of the IEEE/CVF Conference on Computer Vision and Pattern Recognition*, 2024.

Songyuan Zhang, Zhangjie Cao, Dorsa Sadigh, and Yanan Sui. Confidence-aware imitation learning from demonstrations with varying optimality, 2022. URL <https://arxiv.org/abs/2110.14754>.

Chao Zheng et al. Semantic slam system for mobile robots based on large visual model in complex environments. *Scientific Reports*, 15(1):1–15, 2025.

Jun Zhu, Zihao Du, Haotian Xu, Fengbo Lan, Zilong Zheng, Bo Ma, Shengjie Wang, and Tao Zhang. Navi2gaze: Leveraging foundation models for navigation and target gazing, 2024. URL <https://arxiv.org/abs/2407.09053>.

Zihan Zhu, Songyou Peng, Viktor Laehner, Weiyang Xu, Michael Niemeyer, et al. Nice-slam: Neural implicit scalable encoding for slam. In *Proceedings of the IEEE/CVF Conference on Computer Vision and Pattern Recognition*, pp. 12786–12796, 2022.

A IDENTIFIABILITY OF GRL-SNAM

A.1 FROM OPTIMAL CONTROL TO REDUCED HAMILTONIAN DYNAMICS

Lemma A.1 (Forward: autonomous pure state constraints induce a (reduced) Hamiltonian flow). *Fix a scenario \mathcal{E} and consider the autonomous, control-affine system on an open set $\mathcal{Q} \subset \mathbb{R}^n$,*

$$\dot{q}(t) = f(q(t)) + A(q(t))u(t), \quad q(0) = q_0, \quad q(T) = q_T, \quad (32)$$

with pure state inequality constraints

$$d_i(q(t)) \geq 0, \quad i = 1, \dots, m, \quad t \in [0, T], \quad (33)$$

and objective

$$\min_{u(\cdot) \in \mathcal{U}} J(q, u) := \int_0^T L(q(t), u(t)) dt, \quad (34)$$

where the admissible control set \mathcal{U} consists of measurable $u(\cdot)$ with $u(t) \in U \subset \mathbb{R}^d$ a.e.

Assume:

1. f and A are locally Lipschitz on \mathcal{Q} .
2. U is nonempty, compact, and convex; $L(\cdot, \cdot)$ is continuous and C^1 in (q, u) .
3. (Existence) There exists an optimal pair $(q^*(\cdot), u^*(\cdot))$ satisfying Equation (32) and Equation (33).
4. (Regularity / qualification) Each $d_i \in C^2(\mathcal{Q})$ and along boundary arcs the active constraint gradients satisfy a standard constraint qualification (e.g. linear independence of $\{\nabla d_i(q^*(t))\}_{i \in \mathcal{A}(t)}$ and a feasible-direction condition), so that the state-constrained maximum principle applies.

Define the control Hamiltonian as Fenchel Coupling

$$\mathcal{H}_c(q, p, u) := \langle f(q) + A(q)u, p \rangle - L(q, u). \quad (35)$$

Then there exist: (i) a costate $p : [0, T] \rightarrow \mathbb{R}^n$ of bounded variation (\mathbf{BV} , right-continuous with left limits), and (ii) nonnegative finite Radon measures $\{\mu_i\}_{i=1}^m$ on $[0, T]$, such that the following hold:

(i) **Maximum condition (a.e.).** For almost every $t \in [0, T]$,

$$u^*(t) \in \arg \max_{u \in U} \mathcal{H}_c(q^*(t), p(t), u). \quad (36)$$

(ii) **State equation.** For a.e. t ,

$$\dot{q}^*(t) = \nabla_p \mathcal{H}_c(q^*(t), p(t), u^*(t)) = f(q^*(t)) + A(q^*(t))u^*(t). \quad (37)$$

(iii) **Adjoint equation in measure form.** As an equality of \mathbb{R}^n -valued measures on $[0, T]$,

$$dp(t) = -\nabla_q \mathcal{H}_c(q^*(t), p(t), u^*(t)) dt - \sum_{i=1}^m \nabla d_i(q^*(t)) \mu_i(dt). \quad (38)$$

Equivalently, for all $0 \leq t_0 < t_1 \leq T$,

$$p(t_1^+) - p(t_0^-) = - \int_{t_0}^{t_1} \nabla_q \mathcal{H}_c(q^*(t), p(t), u^*(t)) dt - \sum_{i=1}^m \int_{(t_0, t_1]} \nabla d_i(q^*(t)) \mu_i(dt). \quad (39)$$

(iv) **Complementarity / support.** Each μ_i is supported on the active set:

$$\text{supp}(\mu_i) \subset \{t \in [0, T] : d_i(q^*(t)) = 0\}, \quad \text{i.f.f.} \quad \int_{[0, T]} d_i(q^*(t)) \mu_i(dt) = 0. \quad (40)$$

(iv) **Reduced Hamiltonian.** Assume in addition that the running cost decomposes as

$$L(q, u) = \varphi(u) + V(q), \quad \text{with } \varphi \text{ proper, closed, strictly convex, and } C^1, \text{ and } V \in C^1(\mathcal{Q}). \quad (41)$$

Then the maximizer $u^*(q, p)$ in Equation (36) is unique (up to the compact control constraint U), and the reduced PMP Hamiltonian depends only on (q, p) :

$$H_{\text{PMP}}(q, p) := \sup_{u \in U} \mathcal{H}_c(q, p, u) = \sup_{u \in U} \{p^\top A(q)u - \varphi(u)\} + p^\top f(q) - V(q). \quad (42)$$

Hence Equation (37) and Equation (38) can be restated without explicit dependency on u^* .

Proof. We present the derivation in steps and refer readers Theorem 4.2 in Hartl et al. (1995) for further discussions. The proof contains major steps including reducing the general state-constrained PMP statement to the present autonomous, pure-state-constraint setting and then eliminating u via conjugacy.

Step 1 (Apply the state-constrained maximum principle). Under assumptions (1)–(4), the state-constrained maximum principle provides a costate of bounded variation and a bounded-variation multiplier associated with the state constraints, together with an integral adjoint relation. Specializing to *pure* state constraints (no mixed constraints) yields an identity of the form Equation (39) except that the state-constraint multiplier appears as a BV function $\zeta_i(\cdot)$. Writing its Stieltjes increment as $d\zeta_i(t)$ and using the BV decomposition, define the nonnegative measure $\mu_i := -d\zeta_i$; then $\mu_i \geq 0$ and Equation (39) follows.

Step 2 (Maximum condition from needle variations). Fix a Lebesgue point t for (q^*, u^*) and consider a needle variation $u_\varepsilon(\cdot)$ that equals $u^*(\cdot)$ except on a small interval $(t, t + \varepsilon)$ where it is set to a constant $\bar{u} \in U$. Using (A1)–(A2), the first variation of J exists and is linear in $\bar{u} - u^*(t)$, while feasibility of Equation (33) is handled by the measure multipliers μ_i . The necessary condition that the first variation is nonnegative for all $\bar{u} \in U$ implies Equation (36) for almost every t .

Step 3 (Adjoint equation from state variations + integration by parts). Let δq be an admissible first-order state variation induced by admissible control variations. Write the first variation of the Lagrangian functional associated with Equation (32) using a multiplier $p(\cdot)$, and integrate by parts on each interval of continuity of p . The terms involving the state constraints appear through Stieltjes integrals against $d\zeta_i$, i.e., through $\int \nabla c_i(q^*(t)) d\zeta_i(t)$; converting to $\mu_i = -d\zeta_i$ yields Equation (38).

Step 4 (Complementarity/support). Because each $\zeta_i(\cdot)$ is constant on interior intervals where $c_i(q^*(t)) > 0$, its Stieltjes increment vanishes there; hence $\mu_i = -d\zeta_i$ only charges times when the constraint is active. This is exactly Equation (40).

Step 5 (Reduced Hamiltonian by Legendre–Fenchel conjugacy). Define the *reduced Hamiltonian* (pointwise supremum over u)

$$H_{\text{PMP}}(q, p) := \sup_{u \in U} \{p^\top A(q)u - \varphi(u)\} + p^\top f(q) - V(q). \quad (43)$$

By strict convexity of φ , the maximizer $u^*(q, p)$ is unique and satisfies the first-order condition $\nabla \varphi(u^*) = A(q)^\top p$ (when $U = \mathbb{R}^d$; for compact U use the argmax form). Hence $u^*(q, p) = \nabla \varphi^*(A(q)^\top p)$, and Danskin's theorem yields

$$\begin{aligned} \nabla_p H_{\text{PMP}}(q, p) &= f(q) + A(q)u^*(q, p), \\ \nabla_q H_{\text{PMP}}(q, p) &= (\nabla_q f(q))^\top p + (\nabla_q A(q)u^*(q, p))^\top p - \nabla V(q). \end{aligned}$$

Substituting $u^*(t) = u^*(q^*(t), p(t))$ into Equation (37)–Equation (38) gives the *reduced* constrained Hamiltonian flow

$$\begin{aligned} \dot{q}^*(t) &= \nabla_p H_{\text{PMP}}(q^*(t), p(t)), \\ dp(t) &= -\nabla_q H_{\text{PMP}}(q^*(t), p(t)) dt - \sum_{i=1}^m \nabla d_i(q^*(t)) \mu_i(dt), \end{aligned} \quad (44)$$

which is precisely the claimed Hamiltonian outcome of the state-constrained optimal control problem. \square

Corollary A.2 (Reduced Hamiltonian via a quadratic control penalty). *Consider the control-affine dynamics $\dot{q} = f(q; \mathcal{E}) + A(q; \mathcal{E})u$ and assume the cost-to-go functional splits as $L(q, u; \mathcal{E}) = \varphi(u) + V(q; \mathcal{E})$ with a quadratic effort penalty $\varphi(u) = \frac{1}{2}u^\top \Phi u$ for some $\Phi \succ 0$. Assume $f(\cdot; \mathcal{E}) \equiv 0$ and $A(q; \mathcal{E}) \equiv A$. Then the reduced Hamiltonian (i.e. $\sup_u \{p^\top (f + Au) - L\}$) equals*

$$H(q, p; \mathcal{E}) = \frac{1}{2} p^\top (A(q; \mathcal{E})\Phi^{-1} A(q; \mathcal{E})^\top) p - V(q; \mathcal{E}).$$

In particular, if we define the (inverse) mass by

$$M(q; \mathcal{E})^{-1} := A(q; \mathcal{E})\Phi^{-1} A(q; \mathcal{E})^\top \in \mathbb{S}_{++}^2,$$

then $H(\cdot, \cdot; \mathcal{E}) \in \mathcal{H}$, where

$$\mathcal{H}_{PMP} := \left\{ H(q, p; \mathcal{E}) = \frac{1}{2} p^\top M^{-1} p - V(q; \mathcal{E}) \mid M \in \mathbb{S}_{++}^2 \right\}.$$

Proof. By definition of the PMP reduced Hamiltonian,

$$H_{PMP}(q, p; \mathcal{E}) = \sup_u \left\{ p^\top (f(q; \mathcal{E}) + A(q; \mathcal{E})u) - \varphi(u) - V(q; \mathcal{E}) \right\}.$$

Setting $f \equiv 0$ reduces the supremum to $\sup_u \{(A^\top p)^\top u - \frac{1}{2}u^\top \Phi u\} - V$. The maximizer satisfies $\Phi u^* = A^\top p$, hence $u^* = \Phi^{-1} A^\top p$ and the supremum value is $\frac{1}{2}p^\top A\Phi^{-1} A^\top p - V$. Since $\Phi \succ 0$ and $A(\cdot; \mathcal{E})$ has full rank, the induced matrix $A\Phi^{-1} A^\top$ is positive definite, so $M^{-1} \in \mathbb{S}_{++}^2$ and $H \in \mathcal{H}$. \square

Barrier relaxation of state-constraint OCPs In the implementation one replaces hard constraints $d_i(q) \geq 0$ by a smooth barrier/penalty term $B_\mu(q) := \mu \sum_i b(d_i(q))$ and optimizes an *unconstrained* problem with augmented running cost $\bar{L}_\mu(q, u, t) = L(q, u, t) + B_\mu(q)$. This does not require introducing BV multipliers in the PMP dynamics; instead it modifies the potential (equivalently, modifies $\nabla_q H_{PMP}$) by adding $\nabla_q B_\mu$. From the inverse-design viewpoint, learning barrier weights corresponds to selecting a particular absolutely continuous approximation of the constraint measure $d\zeta$ (as a standard exact-penalty / interior-point interpretation). For our GRL-SNAM navigator, we provide additional statements (c.f. Theorem A.3 and Theorem A.4) to address the approximability of our choice of Hamiltonians.

Proposition A.3 (Barrier relaxation $\mu \downarrow 0$ yields a state-constrained limit). *Fix \mathcal{E} and consider the deterministic state-constrained OCP*

$$\begin{aligned} \min_{u(\cdot)} J(u) &:= \int_0^T L(q(t), u(t)) dt \\ \text{s.t. } \dot{q} &= f(q) + A(q)u, \quad q(0) = q_0, \quad q(T) = q_T, \quad d_i(q(t)) \geq 0 \quad \forall t, \quad i = 1, \dots, m. \end{aligned} \tag{45}$$

Assume:

(H1) $U \subset \mathbb{R}^d$ is compact and convex, $u(\cdot) \in L^\infty([0, T]; U)$.

(H2) f, A are globally Lipschitz on \mathbb{R}^n ; $L(\cdot, \cdot)$ is continuous and convex in u , and there exist $c_0, c_1 > 0$ such that $L(q, u) \geq -c_0 + c_1 \|u\|^2$.

(H3) Each $d_i \in C^2(\mathbb{R}^n)$ and the feasible set of Equation (45) is nonempty. Moreover, (Slater) there exists a strictly feasible pair (\bar{q}, \bar{u}) satisfying $d_i(\bar{q}(t)) \geq \delta$ for all $t \in [0, T]$ and all i , for some $\delta > 0$.

(H4) (Existence of an optimal solution) Equation (45) admits at least one optimal pair (q^*, u^*) .

For $\mu > 0$, define the log-barrier relaxed (unconstrained) problems

$$\begin{aligned} \min_{u(\cdot)} J_\mu(u) &:= \int_0^T \left(L(q(t), u(t)) + \mu \sum_{i=1}^m \alpha_i b(d_i(q(t))) \right) dt \\ \text{s.t. } \dot{q} &= f(q) + A(q)u, \quad q(0) = q_0, \quad q(T) = q_T, \end{aligned} \tag{46}$$

where $\alpha_i > 0$ are fixed weights and $b(s) = -\log s$ (so Equation (46) is defined only on trajectories with $d_i(q(t)) > 0$ for all t). Let (q^μ, u^μ) be a minimizer of Equation (46).

Then:

(a) (Strict feasibility) For every $\mu > 0$, $d_i(q^\mu(t)) > 0$ for all $t \in [0, T]$ and all i .

(b) (Subsequence convergence) For any sequence $\mu_k \downarrow 0$, there exists a subsequence (not relabeled) and a feasible pair (q^0, u^0) for Equation (45) such that

$$q^{\mu_k} \rightarrow q^0 \text{ uniformly on } [0, T], \quad u^{\mu_k} \rightharpoonup^* u^0 \text{ in } L^\infty([0, T]; \mathbb{R}^d).$$

(c) (Optimality of cluster points) Any cluster point (q^0, u^0) obtained in (b) is optimal for Equation (45), and the optimal values satisfy $\lim_{\mu \downarrow 0} \inf J_\mu = \inf J$.

Moreover, assume in addition:

(H5) (Uniform multiplier tightness) The measures $\mu_i^\mu(dt) := \lambda_i^\mu(t) dt$ defined by

$$\lambda_i^\mu(t) := \mu \alpha_i \frac{1}{d_i(q^\mu(t))} \geq 0 \iff \mu \alpha_i \nabla b(d_i(q^\mu(t))) = -\lambda_i^\mu(t) \nabla d_i(q^\mu(t)) \quad (47)$$

have uniformly bounded total mass: $\sup_{\mu > 0} \mu_i^\mu([0, T]) < \infty$ for each i .

Then, along the subsequence in (b), $\mu_i^{\mu_k} \xrightarrow{*} \mu_i$ as finite Radon measures, and the limiting pair (q^0, u^0) admits a costate p and measures $\{\mu_i\}$ satisfying the state-constrained PMP in measure form. In particular, complementarity holds:

$$\int_{[0, T]} d_i(q^0(t)) \mu_i(dt) = 0, \quad \text{supp}(\mu_i) \subset \{t : d_i(q^0(t)) = 0\}. \quad (48)$$

Proof. **Step 1 (Existence and strict feasibility for the barrier problems).** Fix $\mu > 0$. By (H3) there exists at least one strictly feasible trajectory, hence J_μ is finite on a nonempty set. Since $b(s) = -\log s$ diverges to $+\infty$ as $s \downarrow 0$ and is undefined for $s \leq 0$, any admissible minimizer must satisfy $d_i(q^\mu(t)) > 0$ for all t and i , proving (a). Existence of a minimizer for Equation (46) follows from standard deterministic OCP existence arguments: (H1) provides weak-* compactness of controls in L^∞ ; (H2) gives existence/uniqueness and continuous dependence of q on u (via global Lipschitz dynamics), and lower semicontinuity of the integral cost under weak-* convergence (using convexity in u). Thus a minimizing sequence has a convergent subsequence whose limit attains the infimum.

Step 2 (Compactness of $\{(q^\mu, u^\mu)\}$ as $\mu \downarrow 0$). Let \bar{u} be the strictly feasible Slater control from (H3), and \bar{q} its trajectory. For any minimizer (q^μ, u^μ) ,

$$J_\mu(u^\mu) \leq J_\mu(\bar{u}) = \int_0^T L(\bar{q}(t), \bar{u}(t)) dt + \mu \sum_i \alpha_i \int_0^T b(d_i(\bar{q}(t))) dt \leq C_0 + \mu C_1,$$

where $C_0, C_1 < \infty$ are constants (since $d_i(\bar{q}(t)) \geq \delta > 0$ implies $b(d_i(\bar{q}(t)))$ is bounded). By (H2), $L(q, u) \geq -c_0 + c_1 \|u\|^2$ yields a uniform L^2 bound on u^μ (hence also boundedness in L^∞ because $u^\mu(t) \in U$). Therefore $\{u^\mu\}$ is bounded in L^∞ , so by Banach–Alaoglu there exists a subsequence $\mu_k \downarrow 0$ with $u^{\mu_k} \rightharpoonup^* u^0$ in L^∞ . By Lipschitz dynamics and bounded controls, the corresponding states q^{μ_k} are equi-Lipschitz and uniformly bounded, so by Arzelà–Ascoli, $q^{\mu_k} \rightarrow q^0$ uniformly for some absolutely continuous q^0 . Passing to the limit in the ODE (continuous dependence of solutions on controls) gives that q^0 is the trajectory induced by u^0 . Since each $d_i(q^{\mu_k}(t)) > 0$ and d_i is continuous, the uniform limit implies $d_i(q^0(t)) \geq 0$ for all t , so (q^0, u^0) is feasible for Equation (45). This proves (b).

Step 3 (Value convergence and optimality of cluster points). We prove $\lim_{\mu \downarrow 0} \inf J_\mu = \inf J$ and that any cluster point is optimal.

(i) *Lim-inf inequality.* For the minimizing sequence u^{μ_k} ,

$$\inf J_{\mu_k} = J_{\mu_k}(u^{\mu_k}) \geq \int_0^T L(q^{\mu_k}(t), u^{\mu_k}(t)) dt = J(u^{\mu_k}),$$

since the barrier term is nonnegative. By convexity of L in u and uniform convergence $q^{\mu_k} \rightarrow q^0$, the integral functional $u \mapsto \int_0^T L(q[u](t), u(t)) dt$ is weak-* lower semicontinuous, hence

$$\liminf_{k \rightarrow \infty} \inf J_{\mu_k} \geq \liminf_{k \rightarrow \infty} J(u^{\mu_k}) \geq J(u^0) \geq \inf J.$$

(ii) *Lim-sup inequality.* Fix any feasible control u for Equation (45) with trajectory q (so $d_i(q(t)) \geq 0$). Let (\bar{q}, \bar{u}) be the Slater strictly feasible pair with margin $\delta > 0$. Define a perturbed control

$$u^{(\epsilon)} := (1 - \epsilon)u + \epsilon\bar{u}, \quad \epsilon \in (0, 1).$$

Then $u^{(\epsilon)} \in U$ a.e. by convexity of U . Let $q^{(\epsilon)}$ be the induced trajectory. By continuous dependence of the ODE solution on controls, $q^{(\epsilon)} \rightarrow q$ uniformly as $\epsilon \downarrow 0$. Moreover, since (\bar{q}, \bar{u}) is strictly feasible and d_i is continuous, there exists $\epsilon_0 > 0$ such that for all $\epsilon \in (0, \epsilon_0)$, $q^{(\epsilon)}$ is *strictly feasible*, i.e. $\min_{t \in [0, T]} d_i(q^{(\epsilon)}(t)) > 0$ for all i (intuitively: the perturbation moves the trajectory into the interior; formally, use uniform convergence plus $d_i(\bar{q}(t)) \geq \delta$ and continuity of d_i). Hence $J_\mu(u^{(\epsilon)})$ is well-defined for all $\mu > 0$.

Now choose a sequence $\epsilon = \epsilon(\mu) \downarrow 0$ such that

$$\epsilon(\mu) \downarrow 0 \quad \text{and} \quad \mu \log(1/\epsilon(\mu)) \rightarrow 0 \quad (\mu \downarrow 0),$$

e.g. $\epsilon(\mu) = \exp(-\sqrt{1/\mu})$. Then $q^{(\epsilon(\mu))} \rightarrow q$ uniformly and $J(u^{(\epsilon(\mu))}) \rightarrow J(u)$ by continuity of L and dominated convergence theorem. For the barrier term, strict feasibility implies $d_i(q^{(\epsilon(\mu))}(t)) \geq c\epsilon(\mu)$ for some $c > 0$ on $[0, T]$ (possibly after shrinking ϵ_0); thus

$$0 \leq \mu \alpha_i \int_0^T b(d_i(q^{(\epsilon(\mu))}(t))) dt \leq \mu \alpha_i T (\log(1/c) + \log(1/\epsilon(\mu))) \xrightarrow[\mu \downarrow 0]{} 0.$$

Therefore $\limsup_{\mu \downarrow 0} \inf J_\mu \leq \lim_{\mu \downarrow 0} J_\mu(u^{(\epsilon(\mu))}) = J(u)$. Taking infimum over feasible u yields $\limsup_{\mu \downarrow 0} \inf J_\mu \leq \inf J$.

Combining (i) and (ii) gives $\lim_{\mu \downarrow 0} \inf J_\mu = \inf J$. Finally, from the liminf chain $\inf J \leq J(u^0) \leq \liminf \inf J_{\mu_k} = \inf J$, we conclude $J(u^0) = \inf J$, so (q^0, u^0) is optimal for Equation (45). This proves (c).

Step 4 (Adjoint equation in measure form and complementarity). For each μ , the barrier problem Equation (46) is unconstrained (aside from boundary conditions), hence admits the classical PMP. The barrier contribution to the adjoint equation is

$$-\nabla_q \left(\mu \sum_i \alpha_i b(d_i(q^\mu(t))) \right) = -\sum_i \lambda_i^\mu(t) \nabla d_i(q^\mu(t)), \quad \lambda_i^\mu(t) = \mu \alpha_i \frac{1}{d_i(q^\mu(t))} \geq 0,$$

which is Equation (47). Assumption (H5) implies the measures $\mu_i^\mu(dt) := \lambda_i^\mu(t) dt$ have uniformly bounded total mass, hence are weakly-* precompact in the space of finite Radon measures. Therefore, along a subsequence, $\mu_i^{\mu_k} \rightharpoonup^* \mu_i$. Passing to the limit in the adjoint equation yields the measure-form adjoint relation of the state-constrained PMP, with multipliers $\{\mu_i\}$.

To prove complementarity Equation (48), note that for each μ ,

$$\int_0^T d_i(q^\mu(t)) \mu_i^\mu(dt) = \int_0^T d_i(q^\mu(t)) \lambda_i^\mu(t) dt = \int_0^T \mu \alpha_i dt = \mu \alpha_i T \xrightarrow[\mu \downarrow 0]{} 0.$$

Since $q^{\mu_k} \rightarrow q^0$ uniformly and d_i is continuous, $d_i(q^{\mu_k}) \rightarrow d_i(q^0)$ uniformly. By weak-* convergence of measures, $\int d_i(q^{\mu_k}) d\mu_i^{\mu_k} \rightarrow \int d_i(q^0) d\mu_i$. Thus $\int d_i(q^0) d\mu_i = 0$ and, since both terms are nonnegative, μ_i is supported on $\{t : d_i(q^0(t)) = 0\}$. \square

We extend the Theorem A.3 in IPC barrier potential as well. The statement is addressed in Theorem A.4.

Corollary A.4 (IPC barrier inherits the log-barrier limit (primal) and contact-measure form (dual)). *Consider the state-constrained OCP Equation (45) and assume the hypotheses of Proposition A.3 stated for the log-barrier $b(s) = -\log s$. Fix activation distances $\hat{d}_i > 0$ and define the IPC barrier (clamped to zero outside the activation region) by*

$$b_{\text{IPC}}(d; \hat{d}) := \begin{cases} (\hat{d} - d)^2 \phi\left(\frac{d}{\hat{d}}\right), & 0 < d < \hat{d}, \\ 0, & d \geq \hat{d}, \end{cases} \quad b(x) = -\log x. \quad (49)$$

For $\mu > 0$, consider the barrier-relaxed problems with running cost augmented by $\mu \sum_i \alpha_i b_{\text{IPC}}(d_i(q); \hat{d}_i)$ (where $\alpha_i > 0$ are fixed weights and $d_i(q) > 0$ is required whenever b_{IPC} is active). Let (q^μ, u^μ) be minimizers.

(i) **Primal limit.** As $\mu \downarrow 0$, any sequence $\mu_k \downarrow 0$ admits a subsequence such that $q^{\mu_k} \rightarrow q^*$ (uniformly) and $u^{\mu_k} \xrightarrow{*} u^*$, where (q^*, u^*) is an optimal solution of the original hard-constrained OCP Equation (45). Moreover, $\lim_{\mu \downarrow 0} \inf J_\mu = \inf J$.

(ii) **Multiplier/measure form (under the same tightness condition).** Define the IPC multiplier densities on the active set $\{t : 0 < d_i(q^\mu(t)) < \hat{d}_i\}$ by

$$\lambda_i^\mu(t) := \mu \alpha_i \left[-\partial_d b_{\text{IPC}}(d_i(q^\mu(t)); \hat{d}_i) \right] \geq 0, \quad \mu_i^\mu(dt) := \lambda_i^\mu(t) dt. \quad (50)$$

If $\sup_{\mu > 0} \mu_i^\mu([0, T]) < \infty$ (uniform tightness), then along a subsequence $\mu_i^\mu \rightharpoonup^* \mu_i$ weakly-* as finite Radon measures, and the limiting necessary conditions take the state-constrained PMP form with contact measures $\{\mu_i\}$. In addition, the complementarity residual vanishes:

$$\int_0^T d_i(q^\mu(t)) \mu_i^\mu(dt) \xrightarrow[\mu \downarrow 0]{} 0, \quad \text{hence} \quad \text{supp}(\mu_i) \subset \{t : d_i(q^*(t)) = 0\}. \quad (51)$$

Proof. **Step 1 (IPC barrier is sandwiched by log barriers on a near-contact region).** Fix i and write $x := d/\hat{d}_i \in (0, 1)$ on the active set. Since $0 < d < \hat{d}_i$ implies $0 < (\hat{d}_i - d)^2 \leq \hat{d}_i^2$, we have the pointwise upper bound

$$0 \leq b_{\text{IPC}}(d; \hat{d}_i) = (\hat{d}_i - d)^2 b(x) \leq \hat{d}_i^2 b(x). \quad (52)$$

On the *near-contact* region $0 < d \leq \hat{d}_i/2$ we also have $(\hat{d}_i - d)^2 \geq (\hat{d}_i/2)^2$, hence

$$b_{\text{IPC}}(d; \hat{d}_i) \geq (\hat{d}_i/2)^2 b(x), \quad 0 < d \leq \hat{d}_i/2. \quad (53)$$

Thus, on any trajectory segment where contacts are potentially active, IPC is equivalent (up to constants) to a log barrier.

Step 2 (Primal convergence via Proposition A.3). Consider the IPC-relaxed objective

$$J_\mu^{\text{IPC}}(u) = \int_0^T \left(L(q, u) + \mu \sum_i \alpha_i b_{\text{IPC}}(d_i(q); \hat{d}_i) \right) dt.$$

By Equation (52), for any admissible (q, u) ,

$$J_\mu^{\text{IPC}}(u) \leq \int_0^T \left(L(q, u) + \mu \sum_i \alpha_i \hat{d}_i^2 \phi\left(\frac{d_i(q)}{\hat{d}_i}\right) \right) dt =: J_\mu^{\log, U}(u),$$

i.e., IPC is no more penalizing than a scaled log barrier. Conversely, by Equation (53), on times when $d_i(q) \leq \hat{d}_i/2$ the IPC term dominates a (smaller) scaled log barrier. This is sufficient for the standard barrier homotopy argument used in Proposition A.3: (i) strict feasibility holds for each μ since $b_{\text{IPC}}(d) \rightarrow \infty$ as $d \downarrow 0$; (ii) the recovery sequence can be constructed exactly as in Proposition A.3 by choosing $\epsilon(\mu) \downarrow 0$ such that $\mu \hat{d}_i^2 b(c\epsilon(\mu)) \rightarrow 0$ (e.g. $\epsilon(\mu) = \exp(-1/\sqrt{\mu})$), and then applying Equation (52) to bound the IPC penalty by the scaled log penalty. Hence $\lim_{\mu \downarrow 0} \inf J_\mu^{\text{IPC}} = \inf J$ and any cluster point of minimizers solves the hard-constrained OCP. This proves (i).

Step 3 (Adjoint equation in measure form and complementarity). For each $\mu > 0$ the IPC-relaxed problem is unconstrained (on the domain $d_i(q) > 0$), so its PMP adjoint equation includes the smooth force $-\mu \alpha_i \partial_d b_{\text{IPC}}(d_i(q^\mu); \hat{d}_i) \nabla d_i(q^\mu)$. Defining λ_i^μ by Equation (50) yields the absolutely continuous measures $\mu_i^\mu(dt) = \lambda_i^\mu(t) dt$. Under the same tightness condition as in Proposition A.3, weak-* sequential compactness of $\mathcal{M}_+([0, T])$ implies $\mu_i^\mu \rightharpoonup^* \mu_i$ along a subsequence, and passing to the limit in the adjoint equation gives the state-constrained measure form.

To show Equation (51), note that on the active set $0 < d < \hat{d}_i$ we can write $b_{\text{IPC}}(d; \hat{d}_i) = \hat{d}_i^2(1 - x)^2 b(x)$ with $x = d/\hat{d}_i$. A direct differentiation gives $-d \partial_d b_{\text{IPC}}(d; \hat{d}_i) = \hat{d}_i^2 x(1 - x)(2(1 - x)b(x) + 1)$, and using the elementary bound $xb(x) = x(-\log x) \leq 1/e$ for $x \in (0, 1]$ yields

$$0 \leq -d \partial_d b_{\text{IPC}}(d; \hat{d}_i) \leq \hat{d}_i^2 \left(1 + \frac{2}{e} \right).$$

Therefore,

$$\begin{aligned} \int_0^T d_i(q^\mu(t)) \mu_i^\mu(dt) &= \mu \alpha_i \int_0^T \left(-d_i(q^\mu(t)) \partial_d b_{\text{IPC}}(d_i(q^\mu(t)); \hat{d}_i) \right) dt \\ &\leq \mu \alpha_i T \hat{d}_i^2 \left(1 + \frac{2}{e} \right) \xrightarrow{\mu \downarrow 0} 0, \end{aligned} \quad (54)$$

proving the vanishing complementarity residual and hence the support statement in Equation (51). \square

A.2 INVERSE HAMILTONIAN DESIGN BY POTENTIAL RESHAPING

We provide additional propositions and theorems to motivate our choice of Hamiltonian function and Hamiltonian dynamics. The optimally controlled dynamics admits a PMP Hamiltonian which solves a Two Point Boundary Value Problem (**TPBVP**). Therefore, it is worthwhile to state reversibility of the Hamiltonian flow and how it relates our choice of Hamiltonian function search space.

Proposition A.5 (Symplectic flow and the shooting map). *Fix \mathcal{E} and let $H(\cdot; \mathcal{E}) \in C^2(T^*Q)$. Let $\Phi_H^t(\cdot; \mathcal{E}) : T^*Q \rightarrow T^*Q$ be the Hamiltonian flow of $\dot{x} = X_H(x)$. For any $(q_0, p_0) \in T^*Q$ and any t in the existence interval, the endpoint map*

$$(q(t), p(t)) = \Phi_H^t(q_0, p_0; \mathcal{E})$$

is well-defined, and $\Phi_H^t(\cdot; \mathcal{E})$ is a diffeomorphism with inverse $\Phi_H^{-t}(\cdot; \mathcal{E})$. In particular, the map

$$\mathcal{S}_{\mathcal{E}}(p_0) := \pi_Q(\Phi_H^T(q_0, p_0; \mathcal{E})) \in Q$$

(where $\pi_Q(q, p) = q$) is C^1 and encodes the shooting formulation of the two-point boundary value problem.

Proposition A.6 (Local feed-forward representation of the TPBVP via an invertible shooting map). *Consider the fixed-endpoint TPBVP*

$$\dot{q} = \nabla_p H(q, p; \mathcal{E}), \quad \dot{p} = -\nabla_q H(q, p; \mathcal{E}), \quad q(0) = q_0, \quad q(T) = q_T. \quad (55)$$

Assume there exists a solution $(q^(\cdot), p^*(\cdot))$ and define $p_0^* := p^*(0)$. Suppose the shooting map $\mathcal{S}_{\mathcal{E}}$ from Lemma A.5 satisfies the rank condition*

$$D\mathcal{S}_{\mathcal{E}}(p_0^*) \in \mathbb{R}^{n \times n} \text{ is nonsingular} \quad (n = \dim Q). \quad (56)$$

Then, by the implicit function theorem, there exist neighborhoods \mathcal{U} of q_T and \mathcal{V} of p_0^ and a C^1 map*

$$\sigma_{\mathcal{E}} : \mathcal{U} \rightarrow \mathcal{V} \quad \text{s.t.} \quad \mathcal{S}_{\mathcal{E}}(\sigma_{\mathcal{E}}(q_T)) = q_T, \quad \sigma_{\mathcal{E}}(q_T) = p_0^*.$$

Consequently, the TPBVP Equation (55) is locally equivalent to the following feed-forward IVP:

$$(q(t), p(t)) = \Phi_H^t(q_0, \sigma_{\mathcal{E}}(q_T); \mathcal{E}), \quad t \in [0, T].$$

That is, solving the TPBVP reduces (locally) to applying the feed-forward map $p_0 = \sigma_{\mathcal{E}}(q_T)$ and integrating forward.

What does the rank condition mean Condition equation 56 is precisely the *nondegeneracy* that makes the endpoint map locally invertible. It can be interpreted as local surjectivity of the map $p_0 \mapsto q(T)$ around p_0^* ; equivalently, small changes in the initial costate can steer the final position in all directions. Without equation 56, the TPBVP may admit multiple solutions or no locally unique solution, and no smooth feed-forward map $q_T \mapsto p_0$ can be asserted.

Proposition A.7 (Forward-only reduction via a costate feedback (Hamilton–Jacobi condition)). *Assume there exists a C^1 function $W : [0, T] \times Q \rightarrow \mathbb{R}$ such that the feedback costate*

$$p = \kappa(t, q) := \nabla_q W(t, q)$$

satisfies, along the induced trajectory, the identity

$$\partial_t W(t, q) + H(q, \nabla_q W(t, q); \mathcal{E}) = 0, \quad W(T, q) = g(q) \quad (57)$$

for some terminal cost g (or more generally a terminal condition encoding the endpoint constraint). Then the optimal phase trajectory satisfying the PMP conditions can be generated by the forward-only closed-loop ODE

$$\dot{q}(t) = \nabla_p H(q(t), \nabla_q W(t, q(t)); \mathcal{E}), \quad q(0) = q_0,$$

with the costate recovered pointwise by $p(t) = \nabla_q W(t, q(t))$.

Interpretation for Geometric reinforcement learning Proposition A.6 shows a minimal requirement for a feed-forward representation of a TPBVP: a (local) inverse of the shooting map exists under a rank condition. Proposition A.7 is stronger: it reduces the forward–backward system to a forward IVP once a costate feedback $p = \kappa(t, q)$ exists, which is equivalent to the existence of a generating function W solving a Hamilton–Jacobi equation. In practice, a learned meta-map $\mathcal{E} \mapsto H(\cdot; \mathcal{E})$ together with either (i) a learned initializer $\sigma_{\mathcal{E}}$ or (ii) a learned costate feedback $\kappa_{\xi}(t, q; \mathcal{E})$ provides a feed-forward surrogate of the TPBVP.

Lemma A.8 (Time-reversal symmetry for mechanical Hamiltonians). *Let $H(q, p) = K(p) + V(q)$ on T^*Q , where $K \in C^2$ satisfies $K(-p) = K(p)$. Let Φ_H^t be the Hamiltonian flow and define the involution $\iota_R(q, p) := (q, -p)$. Then, for all t for which both sides are defined,*

$$\iota_R \circ \Phi_H^t = \Phi_H^{-t} \circ \iota_R.$$

Equivalently, if $x(t) = (q(t), p(t))$ solves Hamilton’s equations forward in time, then $\tilde{x}(t) := \iota_R(x(-t)) = (q(-t), -p(-t))$ is also a forward-time solution.

Proof. Hamilton’s equations are $\dot{q} = \nabla_p K(p)$ and $\dot{p} = -\nabla_q V(q)$. Let $\tilde{q}(t) := q(-t)$ and $\tilde{p}(t) := -p(-t)$. Then $\dot{\tilde{q}}(t) = -\dot{q}(-t) = -\nabla_p K(p(-t)) = \nabla_p K(-p(-t)) = \nabla_p K(\tilde{p}(t))$, where we used $\nabla_p K(-p) = -\nabla_p K(p)$. Also $\dot{\tilde{p}}(t) = -(-\dot{p}(-t)) = \dot{p}(-t) = -\nabla_q V(q(-t)) = -\nabla_q V(\tilde{q}(t))$. Thus (\tilde{q}, \tilde{p}) satisfies Hamilton’s equations, which is equivalent to the flow identity. \square

Feed-forward Hamiltonian and non-symplectic Hamiltonian dynamics Lemma A.8 applies only to *conservative* Hamiltonian dynamics (purely symplectic flows) which can reverse the p-dynamics given the terminal state of $p(T)$. Our deployed rollouts may include friction, barrier shaping, or other nonconservative corrections, in which case the induced time- Δt map is generally *not* symplectic and the time-reversal identity may not hold. In this work we use the conservative time-reversibility property only as *motivation* for adopting a forward, energy-shaped surrogate that is well-posed as an IVP and admits Lyapunov-type descent guarantees. Our policy learner (Equation (10)) learns a generalized Hamiltonian dynamics where dissipation and open-loop source term are considered as well. Formal approximability between such surrogates and the original PMP and TPBVP are considered as further research interests. Below we state our preliminary theorems.

Theorem A.9 (Local existence of a costate initializer map). *Assume: (i) for a given (q_0, q_T, \mathcal{E}) there exists a solution (q^*, p^*) of Equation (55) with $q^*(0) = q_0$ and $q^*(T) = q_T$; (ii) the Jacobian $\nabla_{p_0} S(p_0^*; q_0, q_T, \mathcal{E})$ is nonsingular. Then there exists a neighborhood \mathcal{U} of (q_0, q_T, \mathcal{E}) and a unique C^1 map*

$$\Pi^* : (q_0, q_T, \mathcal{E}) \mapsto p_0^* = \Pi^*(q_0, q_T, \mathcal{E})$$

such that $S(\Pi^(q_0, q_T, \mathcal{E}); q_0, q_T, \mathcal{E}) = 0$ for all $(q_0, q_T, \mathcal{E}) \in \mathcal{U}$.*

Proof. $S(\cdot; q_0, q_T, \mathcal{E})$ is C^1 in p_0 under the C^1 regularity of H and smooth dependence of ODE solutions on initial conditions. Apply the implicit function theorem to $S(p_0; q_0, q_T, \mathcal{E}) = 0$ at $(p_0^*; q_0, q_T, \mathcal{E})$. \square

Corollary A.10 (Forward-only reconstruction of the optimal trajectory). *Under the assumptions of Theorem A.9, if a feed-forward model $\widehat{\Pi}_{\xi}(q_0, q_T, \mathcal{E})$ approximates Π^* on \mathcal{U} , then the forward integration of Equation (55) initialized at $(q_0, \widehat{\Pi}_{\xi}(q_0, q_T, \mathcal{E}))$ produces a trajectory whose terminal error satisfies*

$$\|q(T; q_0, \widehat{\Pi}_{\xi}, \mathcal{E}) - q_T\| \leq L_S \|\widehat{\Pi}_{\xi}(q_0, q_T, \mathcal{E}) - \Pi^*(q_0, q_T, \mathcal{E})\|$$

for a local Lipschitz constant L_S , and the induced control $u^(q(t), p(t), t; \mathcal{E})$ is near-optimal whenever the resulting TPBVP residual is small (by standard stability of convex optimal control problems).*

A.3 IDENTIFIABILITY AND CONVERGENCE OF HAMILTONIAN UPDATES

Discrete-time deterministic setting. Fix an environment \mathcal{E} and a time step $\Delta t > 0$. Let $(q_t, p_t)_{t=0}^T$ denote a (measured or high-fidelity) trajectory generated by an (unknown) optimal control law. Assume the dynamics class and the control penalty are fixed/known, and we learn only the *potential weights* in a reduced Hamiltonian of the form

$$H_{\eta}(q, p, t; \mathcal{E}) := \frac{1}{2} p^T M^{-1} p + \mathcal{R}(q, t; \eta_{\xi}(\mathcal{E})) \tag{58}$$

where $R(q, t; \eta_\xi(\mathcal{E})) := \eta^T \phi(q, t; \mathcal{E})$ refer fixed-form potential functionals (determined from context of \mathcal{E} , and one example is Equation (13)) and $\eta := \eta_\xi(\mathcal{E}) \in \mathbb{R}^m$ are the weights (optionally constrained $\eta \geq 0$ via a parametrization). We fix a gauge by assuming ϕ contains *no pure constant feature* (or, equivalently, we impose a normalization constraint such as $\int \mathcal{R}(q) dq = 0$); this removes the additive-constant ambiguity.

Observation model: identifying η from discrete costate increments. Assume the symplectic Euler form

$$\begin{aligned} p_{t+1} &= p_t - \Delta t \nabla_q H_\eta(q_t, p_t, t; \mathcal{E}) + \varepsilon_t, \\ q_{t+1} &= q_t + \Delta t M^{-1} p_{t+1}, \quad t = 0, \dots, T-1, \end{aligned} \quad (59)$$

where ε_t collects discretization/modeling error ($\varepsilon_t = 0$ in the noiseless case). Since only \mathcal{R}_η depends on η and $\nabla_q \mathcal{R}_\eta = \sum_{j=1}^m \eta_j \nabla_q \phi_j$, define the regression target

$$y_t := \frac{p_t - p_{t+1}}{\Delta t} = \sum_{j=1}^m \eta_j g_{t,j} + \tilde{\varepsilon}_t, \quad g_{t,j} := \nabla_q \phi_j(q_t, t; \mathcal{E}), \quad (60)$$

with $\tilde{\varepsilon}_t := -\varepsilon_t / \Delta t$. Stacking $y_t \in \mathbb{R}^{d_q}$ gives a linear least-squares problem in η .

Assumption A.1 (Persistent excitation on visited paths). *Let $G \in \mathbb{R}^{m \times m}$ be the (trajectory) Gram matrix*

$$G := \sum_{t=0}^{T-1} \mathbf{G}_t, \quad \mathbf{G}_t := \left[\langle g_{t,i}, g_{t,j} \rangle \right]_{i,j=1}^m,$$

where $\langle \cdot, \cdot \rangle$ is the Euclidean inner product in \mathbb{R}^{d_q} . Assume $G \succeq \gamma I$ for some $\gamma > 0$.

Theorem A.11 (Identifiability of potential weights from deterministic discrete paths). *Consider the noiseless case $\varepsilon_t \equiv 0$ in Equation (59). Under Assumption A.1, the weights η in Equation (58) are uniquely determined by the observed path $\{(q_t, p_t)\}_{t=0}^T$ through Equation (60); i.e., if η and η' yield the same $\{y_t\}_{t=0}^{T-1}$, then $\eta = \eta'$.*

Proof. If η and η' yield the same y_t , then $\sum_{j=1}^m (\eta_j - \eta'_j) g_{t,j} = 0$ for all t . Let $\delta := \eta - \eta'$. Taking inner products with $g_{t,i}$ and summing over t gives $(G\delta)_i = \sum_t \sum_j \delta_j \langle g_{t,i}, g_{t,j} \rangle = 0$ for all i , hence $G\delta = 0$. Assumption A.1 implies $\delta = 0$, so $\eta = \eta'$. \square

Learning objective and Hamiltonian update convergence in learning time. Given a dataset of trajectories (possibly multiple rollouts and/or multiple environments), define the empirical loss

$$\mathcal{J}(\eta) := \frac{1}{2} \sum_{t=0}^{T-1} \|y_t - \sum_{j=1}^m \eta_j g_{t,j}\|_2^2 + \frac{\lambda}{2} \|\eta\|_2^2, \quad \lambda \geq 0, \quad (61)$$

where y_t and $g_{t,j}$ are defined by Equation (60). This is a convex quadratic in η .

Theorem A.12 (Strong convexity, convergence of η_k , and vanishing Hamiltonian updates). *Assume either (i) $\lambda > 0$, or (ii) $\lambda = 0$ and Assumption A.1 holds. Then \mathcal{J} is μ -strongly convex for some $\mu > 0$ and has a unique minimizer η^* . Consider gradient descent in learning time k :*

$$\eta_{k+1} = \eta_k - \alpha \nabla \mathcal{J}(\eta_k), \quad 0 < \alpha < \frac{2}{L},$$

where L is the Lipschitz constant of $\nabla \mathcal{J}$. Then $\eta_k \rightarrow \eta^*$ linearly and the induced Hamiltonian updates vanish on any bounded set: for any compact $\mathcal{K} \subset Q \times \mathbb{R}^{d_q}$,

$$\sup_{(q,p) \in \mathcal{K}} |H_{\eta_{k+1}}(q, p, t; \mathcal{E}) - H_{\eta_k}(q, p, t; \mathcal{E})| \xrightarrow[k \rightarrow \infty]{} 0. \quad (62)$$

Moreover, along any observed trajectory points $\{q_t\}$,

$$\max_{t \in \{0, \dots, T\}} |H_{\eta_{k+1}}(q_t, p_t, t; \mathcal{E}) - H_{\eta_k}(q_t, p_t, t; \mathcal{E})| \leq \|\eta_{k+1} - \eta_k\|_2 \cdot \max_t \|\phi(q_t, t; \mathcal{E})\|_2 \xrightarrow[k \rightarrow \infty]{} 0. \quad (63)$$

Proof. Under the stated conditions, the Hessian of \mathcal{J} is $G + \lambda I \succeq \mu I$ for some $\mu > 0$, so \mathcal{J} is strongly convex with unique minimizer η^* . Standard gradient-descent theory (c.f. Nocedal & Wright (2006)) yields linear convergence $\|\eta_k - \eta^*\| \leq \rho^k \|\eta_0 - \eta^*\|$ for some $\rho \in (0, 1)$. Since H_η depends on η only through $\mathcal{R}(q, t; \mathcal{E}) = \eta^\top \phi(q, t; \mathcal{E})$, we have the Lipschitz relation $|H_{\eta'} - H_\eta| = |(\eta' - \eta)^\top \phi| \leq \|\eta' - \eta\| \cdot \|\phi\|$. Combining with $\|\eta_{k+1} - \eta_k\| \rightarrow 0$ yields Equation (62)–Equation (63). \square

Remark (Interpreting dH/dk (learning-time derivative)). *A convenient discrete proxy is*

$$\frac{d}{dk} H_{\eta_k}(q, p) \approx H_{\eta_{k+1}}(q, p) - H_{\eta_k}(q, p) = \phi(q, t; \mathcal{E})^\top (\eta_{k+1} - \eta_k) = -\alpha \phi(q, t; \mathcal{E})^\top \nabla \mathcal{J}(\eta_k).$$

Thus, once the learning dynamics drive $\|\nabla \mathcal{J}(\eta_k)\| \rightarrow 0$, the Hamiltonian update magnitude vanishes uniformly on compact sets where ϕ is bounded.

Remark (Multiple environments and environment-conditioned weights). *If η is environment-dependent (e.g. $\eta = \eta(\mathcal{E})$), the identifiability and strong convexity conditions apply per environment with the corresponding Gram matrix $G(\mathcal{E})$ built from paths sampled in that environment. If $\eta_\xi(\mathcal{E})$ is produced by a neural network, the optimization is nonconvex in ξ ; however, the same Gram condition provides a local identifiability statement for the induced weights and implies vanishing Hamiltonian updates whenever the learning iterates converge to a stationary point.*

A.4 COUPLED STAGEWISE GOAL SELECTION AND ENERGY RESHAPING

Coupled stagewise problem: goal selection and Hamiltonian reshaping. In a stagewise motion planner, each local OCP (stage τ) requires a terminal goal $q_{\text{target}}(\mathcal{E}_\tau)$, while the next stage's initial condition is inherited from the current stage's terminal state. Hence, if the terminal goal is produced by a policy, the overall procedure becomes *coupled*: the goal policy determines $q_{\text{target}}(\mathcal{E}_\tau)$, but its consequence is only revealed after integrating the stage OCP.

To formalize this coupling, let $x_\tau = (q_\tau, p_\tau)$ denote the augmented state, and assume the stagewise dynamics are induced by a barrier-shaped reduced Hamiltonian family H_{η_τ} with weights $\eta_\tau = \eta_\xi(\mathcal{E}_\tau)$ and fixed horizon T_τ . Let $\Phi_{\eta_\tau}^{T_\tau}$ be the flow map at stage τ . Let a goal policy π_γ output the next stage terminal goal as

$$q_{\text{target}}(\mathcal{E}_\tau) = \pi_\gamma(\mathcal{E}_\tau, x_\tau, \mathcal{M}_\tau), \quad (64)$$

where \mathcal{M}_τ is any memory/context (e.g. visited-map encoding, stage index, or recurrent hidden state). Given $(x_\tau, q_{\text{target}}(\mathcal{E}_\tau))$, the inverse-design reshaping step selects a weight vector η_τ (or equivalently ξ) so that the Hamiltonian rollout hits $q_{\text{target}}(\mathcal{E}_\tau)$. Denote this selection operator by S :

$$\eta_\tau = \mathsf{S}(x_\tau, q_{\text{target}}(\mathcal{E}_\tau), \mathcal{E}_\tau), \quad \text{and} \quad x_{\tau+1} = \Phi_{\eta_\tau}^{T_\tau}(x_\tau; \mathcal{E}_\tau). \quad (65)$$

Composition yields a fixed-point (dueling) system. Substituting Equation (64) into Equation (65) yields the closed-loop stage map

$$x_{\tau+1} = \underbrace{\Phi_{\mathsf{S}(x_\tau, \pi_\gamma(\mathcal{E}_\tau, x_\tau, \mathcal{M}_\tau), \mathcal{E}_\tau), \mathcal{E}_\tau}^{T_\tau}(x_\tau; \mathcal{E}_\tau)}_{=: \mathcal{T}_\gamma(x_\tau, \mathcal{M}_\tau, \mathcal{E}_\tau)}. \quad (66)$$

Thus the goal policy and the Hamiltonian-shaping inverse design are not independent modules; they form a coupled system whose behavior is determined by the composite operator \mathcal{T}_γ . The “dueling” phenomenon is precisely that $q_{\text{target}}(\mathcal{E}_\tau)$ is chosen before the OCP is solved, but its quality can only be evaluated after the stage transition is realized. We state the following proposition as how to view sensor policy’s role in the training pipeline but comment out that this joint learning problem remains an open question.

Proposition A.13 (Coupled stagewise inverse design as a fixed-point / bilevel problem). *Assume: (i) the reshaping selection S is well-defined locally (e.g. by Theorem A.6 with a rank condition ensuring local solvability of $q(T) = q_{\text{target}}(\mathcal{E}_\tau)$ under fixed inherited x_τ), and (ii) the flow $\Phi_\eta^{T_\tau}$ depends smoothly on η and x_τ on the region of interest. Then learning a goal policy π_γ jointly with energy weights (or their generator) is equivalently posed as either:*

(a) A fixed-point learning problem: *find γ (and the reshaping module parameters) such that the induced closed-loop stage map Equation (66) has desirable invariants (e.g. reaches a terminal set,*

avoids cycles, satisfies progress constraints), i.e. $x_{\tau+1} = \mathcal{T}_\gamma(x_\tau, \mathcal{M}_\tau, \mathcal{E}_\tau)$ achieves a prescribed global objective.

(b) A bilevel optimization problem: the goal policy is an outer decision variable that selects $q_{\text{target}}(\mathcal{E}_\tau)$, while the inner level solves a stagewise inverse-design problem (reshaping) to realize that goal:

$$\begin{aligned} & \min_{\gamma} \mathbb{E} \left[\sum_{\tau=0}^{S-1} \mathcal{J}_{\text{global}}(x_\tau, q_{\text{target}}(\mathcal{E}_\tau), \mathcal{E}_\tau) \right] \\ \text{s.t. } & q_{\text{target}}(\mathcal{E}_\tau) = \pi_\gamma(\cdot), \\ & \eta_\tau \in \arg \min_{\eta} \|\pi_q \Phi_{\eta}^{T_\tau}(x_\tau) - q_{\text{target}}(\mathcal{E}_\tau)\|^2 + \text{Reg}(\eta), \\ & x_{\tau+1} = \Phi_{\eta_\tau}^{T_\tau}(x_\tau). \end{aligned} \quad (67)$$

In either view, evaluating the quality of $q_{\text{target}}(\mathcal{E}_\tau)$ necessarily requires integrating (or rolling out) the stage dynamics, so sequential solution is intrinsic to the problem structure.

Practical resolution: amortize the inner solve and train end-to-end In implementation, the inner “reshaping” solve (selecting η_τ to hit $q_{\text{target}}(\mathcal{E}_\tau)$) is typically amortized by a feed-forward policy $\eta_\xi(\mathcal{E}_\tau, \cdot)$ and trained through differentiable rollouts. This converts the bilevel structure into a single differentiable computation graph:

$$x_{\tau+1} = \Phi_{\eta_\xi(\mathcal{E}_\tau, x_\tau, \mathcal{M}_\tau)}^{T_\tau}(x_\tau), \quad q_{\text{target}}(\mathcal{E}_\tau) = \pi_\gamma(\mathcal{E}_\tau, x_\tau, \mathcal{M}_\tau),$$

with gradients backpropagated through the unrolled stage map.

When sequential coupling is unavoidable Even if π_γ is deterministic, the mapping from $(\mathcal{E}_\tau, x_\tau)$ to the realized next state $x_{\tau+1}$ depends on the stagewise OCP solution operator. Therefore the next-stage goal cannot be certified without either (i) executing the inner rollout/solve, or (ii) learning a sufficiently accurate surrogate for that solve. This is a structural property of stagewise planning and not an artifact of a particular algorithm.

B ALGORITHM IMPLEMENTATION DETAILS

This appendix gives the discrete-time implementation of the port–Hamiltonian navigation policy in Equation (4) together with the module interface in Equation (12) and the dissipative/port form in Equation (10). We provide Algorithm 3 (online GRL–SNAM) with explicit equation references (no section cross-references).

Throughout, we use: environment state \mathcal{E}_n , active constraints \mathcal{C}_n , module Hamiltonians H_k and responses R_k , navigator/meta-policy g_ξ , surrogate potential $\mathcal{R}(q; \eta, \mathcal{E})$, and port–Hamiltonian correction parameters (μ, u_f) . The phase-space state is $z_n = (q_n, p_n)$.

Discrete-time convention. We use a fixed integration step $\tau > 0$ and discrete index $n \in \mathbb{N}$ with physical time $t_n := n\tau$. All horizons (T_y, T_f, T_o) are integers measured in integration steps.

Configuration decomposition. When we need the robot center/position \mathbf{c}_n from the configuration q_n , we write

$$q_n = (\mathbf{c}_n, \text{other coordinates}), \quad \mathbf{c}_n := \text{pos}(q_n). \quad (68)$$

Active-set definition. Given signed distance functions $\{d_i(\cdot; \mathcal{E}_n)\}$ and activation threshold \hat{d} , the active set used throughout is

$$\mathcal{C}_n := \{i \mid d_i(q_n; \mathcal{E}_n) \leq \hat{d}\}. \quad (69)$$

Surrogate energy and Hamiltonian. For $\eta = (\beta, \lambda, \{\alpha_i\}_{i \in \mathcal{C}_n})$, we assemble

$$\mathcal{R}(q_n; \eta, \mathcal{E}_n) = E_{\text{sensor}}(q_n; \mathcal{E}_n, \omega_y) + \beta E_{\text{goal}}(q_n; \mathcal{E}_n, \omega_g) \quad (70)$$

$$+ \lambda E_{\text{obj}}(q_n; \omega_d) + \sum_{i \in \mathcal{C}_n} \alpha_i b(d_i(q_n; \mathcal{E}_n); \hat{d}, \omega_b), \quad (71)$$

$$H(q_n, p_n; \eta, \mathcal{E}_n) = \frac{1}{2} p_n^\top M^{-1} p_n + \mathcal{R}(q_n; \eta, \mathcal{E}_n). \quad (72)$$

Block-selectors for dissipation/ports (frame-only). To apply damping/ports only on the frame momentum coordinates, we implement

$$\Gamma(\mu) = \text{blkdiag}(0, \Gamma_f(\mu), 0), \quad G = \text{blkdiag}(0, G_f, 0), \quad \Gamma_f(\mu) = \mu I, \quad G_f = I, \quad (73)$$

and use $\Gamma(\mu), G$ in the discrete update below.

Gradients and one-step update (symplectic Euler). We compute

$$v_n := \nabla_p H(q_n, p_n) = M^{-1} p_n, \quad g_n := \nabla_q H(q_n, p_n) = \nabla_q \mathcal{R}(q_n; \eta, \mathcal{E}_n), \quad (74)$$

and take the symplectic Euler discretization of Equation (4):

$$p_{n+1} = p_n - \tau g_n - \tau \Gamma(\mu) v_n + \tau G u_f, \quad (75)$$

$$q_{n+1} = q_n + \tau M(q_n)^{-1} p_{n+1}. \quad (76)$$

Observables and target. We use

$$\text{clr}_n = \min \left\{ \min_i d_i(q_{n+1}; \mathcal{E}_n), \min_{\ell, i} d_i(q_\ell^{(o)}; \mathcal{E}_n) \right\}, \quad (77)$$

$$\text{dist}_n = \|c_{n+1} - \mathbf{x}_g\|, \quad \text{speed}_n = \|M(q_{n+1})^{-1} p_{n+1}\|, \quad (78)$$

and the observable vector

$$y_n = \begin{bmatrix} -\text{clr}_n \\ \text{dist}_n \\ -\text{speed}_n \end{bmatrix}. \quad (79)$$

We denote the (task-level) target as

$$y_n^* = \begin{bmatrix} -\text{clr}^* \\ \text{dist}^* \\ -\text{speed}^* \end{bmatrix}, \quad (80)$$

where $(\text{clr}^*, \text{dist}^*, \text{speed}^*)$ are fixed design setpoints.

Active parameter vector and Jacobian updates. Let $\mathcal{I}_n \subseteq \mathcal{C}_n$ be the subset of nearby obstacle indices used for the local weight update, and define

$$\tilde{\eta}_n = [\beta_n, \lambda_n, \{\alpha_{n,i}\}_{i \in \mathcal{I}_n}]^\top, \quad \zeta_n = [\tilde{\eta}_n, \mu_n]^\top. \quad (81)$$

We maintain EMA-smoothed secant Jacobians

$$\tilde{J}_n = \frac{(y_n - y_{n-1})(\zeta_n - \zeta_{n-1})^\top}{\|\zeta_n - \zeta_{n-1}\|_2^2 + \varepsilon}, \quad J_n = \rho J_{n-1} + (1 - \rho) \tilde{J}_n, \quad (82)$$

$$\tilde{P}_n = \frac{(y_n - y_{n-1})(u_{f,n} - u_{f,n-1})^\top}{\|u_{f,n} - u_{f,n-1}\|_2^2 + \varepsilon}, \quad P_n = \rho P_{n-1} + (1 - \rho) \tilde{P}_n. \quad (83)$$

Tikhonov LS update, projection, residual, and port correction. With desired increment $\Delta y_n^{\text{des}} := y_n^* - y_n$, we solve

$$\Delta \zeta_n = (J_n^\top J_n + \lambda_\zeta I)^{-1} J_n^\top \Delta y_n^{\text{des}}, \quad \zeta_n^{\text{upd}} = \Pi_{\mathbb{R}_+}(\zeta_n + \kappa \odot \Delta \zeta_n), \quad (84)$$

$$r_n = \Delta y_n^{\text{des}} - J_n \Delta \zeta_n, \quad (85)$$

$$u_{f,n}^{\text{upd}} = (P_n^\top P_n + \lambda_u I)^{-1} P_n^\top r_n, \quad u_{f,n}^{\text{upd}} \leftarrow \text{clip}(u_{f,n}^{\text{upd}}, \mathcal{U}). \quad (86)$$

Algorithm 3 Online GRL–SNAM: Navigator-driven Hamiltonian composition with QoI feedback

1: **Input:** goal \mathbf{x}_g , initial $z_0 = (q_0, p_0)$ (typically $p_0=0$), step τ , horizons (T_y, T_f, T_o) , max steps N_{\max}
2: **Init:** $n \leftarrow 0$, environment \mathcal{E}_0 , active set $\mathcal{C}_0 \leftarrow \emptyset$
3: **Init:** meta state $(\eta_0, \mu_0, u_{f,0})$ from g_ξ , Jacobians J_0, P_0 (Equations (82) and (83))
4: **while** $\neg \text{REACHEDGOAL}(c_n, \mathbf{x}_g)$ and $n < N_{\max}$ **do** $\triangleright c_n = \text{pos}(q_n)$ from Equation (68)
5: **(A) Sensor refresh and active-set discovery (low rate):**
6: **if** $n \equiv 0 \pmod{T_y}$ **then**
7: Query π_y with $\mathcal{Q}_y^n = (\mathcal{E}_n, \mathcal{C}_n, z_{y,0}=z_n, H_y(\cdot; \eta_n), T_y; \theta_y)$
8: Receive $\mathcal{R}_y^n = \{z_{0:T_y}^{(y)}, s_{0:T_y}^{(y)}, \Delta\mathcal{E}_n\}$
9: Update $\mathcal{E}_n \leftarrow \mathcal{E}_n \cup \Delta\mathcal{E}_n$
10: Update $\mathcal{C}_n \leftarrow \{i \mid d_i(q_n; \mathcal{E}_n) \leq \hat{d}\}$ \triangleright Equation (69)
11: **end if**
12: **(B) Frame and shape rollouts (medium/high rate):**
13: **if** $n \equiv 0 \pmod{T_f}$ **then**
14: Query π_f with $\mathcal{Q}_f^n = (\mathcal{E}_n, \mathcal{C}_n, z_{f,0}=z_n, H_f(\cdot; \eta_n, \mu_n, u_{f,n}), T_f; \theta_f)$
15: Receive $\mathcal{R}_f^n = \{z_{0:T_f}^{(f)}, s_{0:T_f}^{(f)}, \{v_\ell^{(f)}\}_{\ell=0}^{T_f}\}$
16: **end if**
17: Query π_o with $\mathcal{Q}_o^n = (\mathcal{E}_n, \mathcal{C}_n, z_{o,0}=z_n, H_o(\cdot; \eta_n), T_o; \theta_o)$
18: Receive $\mathcal{R}_o^n = \{z_{0:T_o}^{(o)}, s_{0:T_o}^{(o)}, \{\min_i d_i(q_\ell^{(o)}; \mathcal{E}_n)\}_{\ell=0}^{T_o}\}$
19: **(C) Meta-policy proposal (environment & response → weights):**
20: Build tokens \mathcal{T}_n from $(\mathcal{E}_n, \mathcal{C}_n, z_n, \mathbf{x}_g, \mathcal{R}_f^n, \mathcal{R}_o^n)$
21: $[\eta_n^{\text{prop}}, \mu_n^{\text{prop}}, u_{f,n}^{\text{prop}}] \leftarrow g_\xi(\mathcal{T}_n; \xi)$
22: with $\eta_n^{\text{prop}} = (\beta_n, \lambda_n, \{\alpha_{n,i}\}_{i \in \mathcal{C}_n}) \in \mathbb{R}_+^{2+|\mathcal{C}_n|}$
23: **(D) Compose surrogate Hamiltonian:**
24: Assemble $\mathcal{R}(q_n; \eta_n^{\text{prop}}, \mathcal{E}_n)$ via Equation (70)
25: Assemble $H(q_n, p_n; \eta_n^{\text{prop}}, \mathcal{E}_n)$ via Equation (72)
26: **(E) One-step port–Hamiltonian integration:**
27: Compute (v_n, g_n) via Equation (74)
28: Apply frame-only dissipation/port via Equation (73) and step Equations (75) and (76)
29: Set $z_{n+1} = (q_{n+1}, p_{n+1})$
30: **(F) Observable extraction:** \triangleright Equations (77) and (79)
31: Compute $(\text{clr}_n, \text{dist}_n, \text{speed}_n)$ via Equation (77)
32: Set y_n via Equation (79) and target y_n^* via Equation (80)
33: **(G) Online adaptation of active weights and friction:**
34: Select nearby obstacle indices $\mathcal{I}_n \subseteq \mathcal{C}_n$
35: Form ζ_n via Equation (81); update J_n via Equation (82)
36: Solve $\Delta\zeta_n$ and project to ζ_n^{upd} via Equation (84)
37: **(H) Port correction from residual:**
38: Compute residual r_n via Equation (85)
39: Update P_n via Equation (83) and solve $u_{f,n}^{\text{upd}}$ via Equation (86)
40: **(I) Commit parameters for next step:**
41: Unpack $\zeta_n^{\text{upd}} \mapsto (\beta_n^{\text{upd}}, \lambda_n^{\text{upd}}, \{\alpha_{n,i}^{\text{upd}}\}_{i \in \mathcal{I}_n}, \mu_n^{\text{upd}})$
42: Set $\eta_{n+1} \leftarrow (\beta_n^{\text{upd}}, \lambda_n^{\text{upd}}, \{\alpha_{n+1,i}^{\text{upd}}\}_{i \in \mathcal{C}_n})$ with $\alpha_{n+1,i} = \alpha_{n,i}^{\text{upd}}$ for $i \in \mathcal{I}_n$ and unchanged otherwise
43: Set $\mu_{n+1} \leftarrow \mu_n^{\text{upd}}$, $u_{f,n+1} \leftarrow u_{f,n}^{\text{upd}}$
44: $n \leftarrow n + 1$
45: **end while**
46: **Return:** trajectory $\{z_n\}_{n=0}^N$ and parameter history $\{(\eta_n, \mu_n, u_{f,n})\}_{n=0}^N$

B.1 INITIALIZATION

State initialization. Initialize phase-space coordinates $z_0 = (q_0, p_0)$ and set $p_0 = 0$ unless otherwise stated. When needed, extract $c_0 = \text{pos}(q_0)$ using Equation (68).

Step size and horizons. Choose $\tau \in [10^{-2}, 5 \times 10^{-2}]$ and integer horizons (T_y, T_f, T_o) in steps. Typical settings are $T_y=10, T_f=5, T_o=1$ (sensor refresh slowest, shape fastest), matching the temporal hierarchy in Fig. 9.

Maximum horizon. Let N_{\max} be the maximum number of discrete steps (e.g., 5,000–10,000), giving $t_{\max} = N_{\max}\tau$.

B.2 PARAMETER STRUCTURE AND INITIALIZATION

Meta-policy output and parameterization. The navigator outputs

$$g_{\xi}(\mathcal{T}_n; \xi) = [\eta_n^{\text{prop}}, \mu_n^{\text{prop}}, u_{f,n}^{\text{prop}}], \quad \eta_n^{\text{prop}} = (\beta_n, \lambda_n, \{\alpha_{n,i}\}_{i \in \mathcal{C}_n}) \in \mathbb{R}_+^{2+|\mathcal{C}_n|}.$$

The intra-term parameters $\omega = (\omega_y, \omega_M, \omega_g, \omega_d, \omega_b)$ are fixed across environments; only (η, μ, u_f) vary online.

Frame-only dissipation/ports. We enforce frame-only damping/ports using the block selectors in Equation (73), and the discrete update in Equations (75) and (76).

Jacobian initialization. Initialize J_0 and P_0 to small-norm matrices (e.g., 10^{-2} times identity where compatible), or zeros. They are refined online via the EMA secant updates in Equations (82) and (83).

B.3 TERMINATION CONDITIONS

We terminate if any of the following holds:

Success (goal reached). $\|c_n - \mathbf{x}_g\| < \epsilon_{\text{goal}}$, with $c_n = \text{pos}(q_n)$ from Equation (68).

Timeout. $n \geq N_{\max}$.

Collision (optional hard-stop). $\min_i d_i(q_n; \mathcal{E}_n) < 0$ (penetration).

Stuck (optional). $\|c_n - c_{n-W}\| < \epsilon_{\text{stuck}}$ for a fixed window W (e.g., $W=50$ steps).

B.4 HIERARCHICAL QUERY FLOW

GRL–SNAM uses the query–response interface consistent with Equation (12):

Module query interface. Each module is queried with $\mathcal{Q}_k^n = (\mathcal{E}_n, \mathcal{C}_n, z_{k,0}=z_n, H_k(\cdot), T_k; \theta_k)$ and returns

$$\mathbf{R}_k^n = \{z_{0:T_k}^{(k)}, s_{0:T_k}^{(k)}, \text{QoI}_k\}.$$

Concrete QoIs used in Algorithm 3 are: $\text{QoI}_y = \Delta\mathcal{E}_n$, $\text{QoI}_f = \{v_{\ell}^{(f)}\}_{\ell=0}^{T_f}$, and $\text{QoI}_o = \{\min_i d_i(q_{\ell}^{(o)}; \mathcal{E}_n)\}_{\ell=0}^{T_o}$.

Rate hierarchy. Sensor is queried every T_y steps (active-set update via Equation (69)), frame every T_f steps (stage guidance), and shape every T_o steps (often $T_o=1$).

B.5 SENSOR RESPONSE

Response structure. $\mathbf{R}_y^n = \{z_{0:T_y}^{(y)}, s_{0:T_y}^{(y)}, \Delta\mathcal{E}_n\}$, where $\Delta\mathcal{E}_n$ contains newly detected obstacles or refinements of obstacle parameters.

Active-set update. After $\mathcal{E}_n \leftarrow \mathcal{E}_n \cup \Delta\mathcal{E}_n$, we compute \mathcal{C}_n using Equation (69).

Local Hamiltonian. As in Equation (12), the sensor module uses

$$H_y(q_y, p_y; \mathcal{E}_n, \eta_n) = \frac{1}{2} p_y^\top M_y^{-1} p_y + \mathcal{R}_y(q_y; \mathcal{E}_n, \eta_n), \quad \mathcal{R}_y = E_{\text{sensor}} + \sum_{i \in \mathcal{C}_n} \alpha_{n,i} b(d_i; \hat{d}).$$

B.6 FRAME RESPONSE

Response structure. $\mathcal{R}_f^n = \{z_{0:T_f}^{(f)}, s_{0:T_f}^{(f)}, \{v_\ell^{(f)}\}_{\ell=0}^{T_f}\}$, where $v_\ell^{(f)} = M_f^{-1} p_\ell^{(f)}$.

Local Hamiltonian with dissipation/port. The frame module follows Equation (10) with

$$H_f(q_f, p_f; \mathcal{E}_n, \eta_n) = \frac{1}{2} p_f^\top M_f^{-1} p_f + \mathcal{R}_f(q_f; \mathcal{E}_n, \eta_n), \quad \mathcal{R}_f = \beta_n E_{\text{goal}} + \sum_{i \in \mathcal{C}_n} \alpha_{n,i} b(d_i; \hat{d}),$$

and (Γ_f, G_f) instantiated by Equation (73).

B.7 SHAPE RESPONSE

Response structure. $\mathcal{R}_o^n = \{z_{0:T_o}^{(o)}, s_{0:T_o}^{(o)}, \{\min_i d_i(q_\ell^{(o)}; \mathcal{E}_n)\}_{\ell=0}^{T_o}\}$.

Local Hamiltonian.

$$H_o(q_o, p_o; \mathcal{E}_n, \eta_n) = \frac{1}{2} p_o^\top M_o^{-1} p_o + \mathcal{R}_o(q_o; \mathcal{E}_n, \eta_n), \quad \mathcal{R}_o = \lambda_n E_{\text{obj}} + \sum_{i \in \mathcal{C}_n} \alpha_{n,i} b(d_i; \hat{d}),$$

with no dissipation/ports on the shape subsystem (i.e., $\Gamma_o = 0$, $u_o = 0$).

B.8 HAMILTONIAN ASSEMBLY AND DISCRETE INTEGRATION

Energy terms. We use the surrogate energy and Hamiltonian in Equations (70) and (72).

One-step update. We implement the symplectic Euler step in Equations (75) and (76), using gradients from Equation (74) and frame-only selectors from Equation (73).

B.9 OBSERVABLE EXTRACTION

We compute observables using Equations (77) and (79) and compare against the target in Equation (80).

B.10 PARAMETER ADAPTATION VIA OBSERVABLE FEEDBACK

We form the active parameter vector via Equation (81), update J_n via Equation (82), and solve the projected Tikhonov update via Equation (84). Inactive barrier weights $\alpha_{n,j}$ for $j \notin \mathcal{I}_n$ remain unchanged.

B.11 PORT CORRECTION FROM RESIDUAL

We compute the residual via Equation (85), update P_n via Equation (83), and solve the port LS with clipping via Equation (86). A robust fallback is to set $P_n = \text{diag}(0, 0, \kappa_v)$ (ports primarily regulate speed).

B.12 OUTPUT FORMAT

Trajectory and parameters. Return $\{z_n\}_{n=0}^N$ and the history $\{(\eta_n, \mu_n, u_{f,n})\}_{n=0}^N$ where N is the final step. This enables post-hoc inspection of how $(\beta, \lambda, \alpha_i)$ and μ evolve with the active set in Equation (69), and when nonconservative port forcing is invoked via Equation (86).

B.13 ADDITIONAL HYPERPARAMETERS IN TABLE 1

As a complement to Algorithm 3, we specify additional fixed parameters and training hyperparameters below.

Surrogate training (offline). The surrogate coefficient network g_ξ is trained on short rollouts of horizon $H \in \{2, \dots, 6\}$ steps with loss

$$\mathcal{L} = w_{\text{traj}} \|o_H - o_H^*\|^2 + w_{\text{vel}} \|v_H - v_H^*\|^2 + w_{\text{fric}} \|\gamma - \gamma_o\|^2 + w_{\text{multi}} \mathcal{L}_{\text{ms}},$$

where $(w_{\text{traj}}, w_{\text{vel}}, w_{\text{fric}}, w_{\text{multi}}) = (1.0, 1.0, 0.1, 0.5)$ and \mathcal{L}_{ms} is a multi-start robustness penalty sampling perturbed initial conditions near obstacles. We use learning rate $\eta \in [10^{-4}, 3 \times 10^{-4}]$ with Adam and gradient clipping at norm 5.0.

IPC barrier. The log-barrier $b(d; \hat{d}) = -(d - \hat{d})^2 \log(d/\hat{d})$ activates at distance $\hat{d} \in [0.28, 1.0]$. Barrier values and gradients are clamped to $[0, 200]$ and $[-200, 200]$ respectively for numerical stability.

Stage planning. Stages have dimensions $(W_{\text{stage}}, H_{\text{stage}}) = (2.6, 2.0)$ with overlap ratio $\rho_{\text{overlap}} = 0.3$. Obstacles are inflated by $r_{\text{inflate}} \in [0.05, 0.4]$ to define the collision-free tube for widest-path exit selection. The margin factor for radius-aware integration is 0.5.

Hyperelastic ring experiment. *Dynamics:* The ring uses mass matrix $M = \text{blkdiag}(M_o I_2, I, M_s)$ with $(M_o, I, M_s) = (1.5, 0.6, 1.0)$ and nominal damping $(\gamma_o, \gamma_\theta, \gamma_s) = (4.0, 1.6, 2.0)$. Area resistance uses bulk modulus $k_{\text{bulk}} = 1.5$. *Geometry:* The periodic cubic B-spline boundary has $n_{\text{ctrl}} = 20$ control points and $K = 240$ curve samples, with nominal robot radius $r_{\text{robot}} \in [0.30, 0.50]$. *Integration:* Symplectic Euler with timestep $\tau = 0.03$ s.

Dungeon navigation experiment. *Dataset generation:* Maximum velocity $v_{\text{max}} \in [2.5, 3.0]$ px/s, goal attraction gain $k_{\text{goal}} \in [20, 25]$, barrier repulsion gain $k_{\text{barrier}} \in [0, 1]$ (often 0 when SDF provides implicit avoidance), and barrier activation $\hat{d} = 1.0$ px. *Integration:* Explicit Euler with timestep $\tau = 0.3$ s and 4 substeps for collision resolution. *Environment:* Obstacle distances are queried from a precomputed signed distance field $\text{SDF}(x, y)$ via Euclidean distance transform. Stages are square windows of side $s_{\text{stage}} = 60$ px, with waypoints inflated to maintain wall clearance $d_{\text{wp}} \geq 1.5\text{--}4.0$ px.

Test-time adaptation. When enabled, online finetuning uses proximal regularization $\lambda_{\text{prox}} = 10^{-3}$ anchored to the pretrained checkpoint, updating only the final projection heads. The secant-based controller selects $k_\alpha \in \{1, 2\}$ nearest obstacles for local α -adjustment with per-head learning rates $(\kappa_\beta, \kappa_\gamma, \kappa_\alpha) = (0.25, 0.05, 0.4)$.